Analysis of flow through cylindrical packed beds with small cylinder diameter to particle diameter ratios.

WJS Van der Merwe

Dissertation submitted in fulfilment of the requirements for the degree *Master in Nuclear Engineering* at the Potchefstroom Campus of the North-West University

Supervisor: Prof CG du Toit

Co-Supervisor: Dr J-H Kruger

May 2014

Abstract

The wall effect is known to present difficulties when attempting to predict the pressure drop over randomly packed beds. The Nuclear Safety Standard Commission, "Kerntechnischer Ausschuss" (KTA), made considerable efforts to develop an equation which predicts the pressure drop over cylindrical randomly packed beds consisting of mono-sized spheres. The KTA was able to estimate a limiting line, which defines the region for which the wall effect is negligible, however the theoretical basis for this line is unclear. The goal of this investigation was to determine the validity of the KTA limiting line, using an explicit approach.

Packed beds were generated using Discrete Element Modelling (DEM), and the flow through the beds simulated using Computational Fluid Dynamics (CFD). STAR-CCM+® was used for both DEM and CFD operations, and the methods developed for this explicit approach were validated with empirical data. The KTA correlation predictions for friction factors were compared with the CFD results, as well as the predictions from a few other correlations.

The KTA correlation predictions for friction factors did not correspond well with the CFD results at low aspect ratios and low modified Reynolds numbers, due to the influence of the wall effect. The KTA limiting line was found to be valid, but not exact. A new limiting line for the KTA correlation was suggested, however the new limiting line improved little on the existing line and was the result of some major assumptions. In order to improve the determination of the position of the KTA limiting line further, criteria need to be established which determine how small the error in predicted friction factor must be before the KTA correlation can be accepted as accurate.

Keywords: Randomly packed beds; Spherical particles; Low aspect ratios; Pressure drop; Porosity; Wall effect; DEM; CFD; STAR-CCM+®.

Declaration

I, Wian Johannes Stephanus van der Merwe (Identity Number: 890626 5083 089), hereby declare the work contained in this dissertation to be my own. All information which has been gained from various journal articles, text books or other sources has been referenced accordingly.

Mr. W.J.S. van der Merwe Date

Acknowledgements

First and foremost I humbly thank my heavenly Father for His unending love, support and strength. Without Him this project would not have been possible.

I would like to express my gratitude to all those who have supported me during this study. My sincere thanks goes to my study leaders, Prof. C.G. (Jat) du Toit and Dr. J-H. Kruger, whose advice and guidance lead me during every step of this study. Prof. Jat, whose maddening attention to detail drove me to finally learn the difference between "compared to" and "compared with", taught me the value of research and also encouraged me to pursue a Ph.D. internationally. For that, I am extremely grateful. It has been a pleasure and a privilege to work under these insightful and knowledgeable leaders.

I also thank my friend and colleague, Mr. Lambert H. Fick, who helped me through the difficulties of this study and motivated me to always keep a positive outlook. I will be ever grateful for his friendship and support.

Finally I would like to thank my parents and my brother for their love, encouragement, patience and advice during these past two years. Though they might not have fully understood what this study entailed, they were always on hand to help me through the rough times. This study would not have been possible without them, and my gratitude for their unending support cannot be expressed in words.

This work is based upon research supported by the South African Research Chairs Initiative of the Department of Science and Technology and National Research Foundation. Any opinions, findings and conclusions or recommendations expressed in this material are those of the author(s) and therefore the NRF and DST do not accept any liability with regard thereto.

Contents

List of Figures

List of Tables

Nomenclature

General

a, a'	Constants in eqns. (2.11) to (2.13).
A	Area.
b, b'	Constants in eqns. (2.11) to (2.13).
B	Mesh base size.
C	Contact area between two particles.
C_{fs}	Coefficient of static friction.
d	Diameter of spherical particle.
D	Cylinder diameter.
D_C	Diameter of contact area between two particles.
D_H	Hydraulic diameter.
Δp	Pressure drop.
e, e', e''	Constants in eqns. (2.15) and (2.16).
E, E'	Functions in eqns. (2.15) and (2.16).
f	Fillet radius at contact points.
J	Damping coefficient.
k	Turbulent kinetic energy.
K	Spring stiffness.
ℓ	Turbulent length scale.
L	Axial length of bed.
L_{DEM}	Axial length of cylinder in DEM simulations.
L_I	Axial length of inlet region.
L_O	Axial length of outlet region.
m	Mass.
n	Constant in eqns. (2.11) and (2.13).
n'	Function in eq. (2.20).
N	Number of particles.
p	Pressure.
r	Radial coordinate.
R	Cylinder radius.
Re	Reynolds number.
S	Source term.
t	Time.
T	Temperature.

u	Component of $\mathbf{u}$ in the x-direction.
U	Superficial velocity.
U_i	Interstitial velocity.
v	Component of $\mathbf{u}$ in the y-direction.
V	Volume.
∂V	Control volume boundary.
w	Component of $\mathbf{u}$ in the z-direction.
x	Coordinate in the x-direction.
y	Coordinate in the y-direction.
z	Coordinate in the z-direction (axial coordinate).
z'	Number of planes tangential to the z axis.

Greek letters

α	Aspect Ratio (D/d).
γ	Turbulent velocity scale.
Γ	Diffusion coefficient.
δ	Kronecker delta.
Δ	Change.
ε	Porosity.
ϵ	Dissipation rate of turbulent kinetic energy.
ζ	Cell quality metric.
θ	Skewness angle.
ϑ	Number of faces.
κ	Conduction heat transfer coefficient.
λ	Control volume label.
μ	Dynamic viscosity.
μ^{τ}	Turbulent viscosity.
ν	Specific internal energy.
ρ	Density.
Υ	Dissipation function.
ϕ	General property.
ϕ'	General fluctuating component of ϕ.
φ	Face index.
Φ	Time average of the property ϕ.
Ψ	Friction factor.
ω	Dissipation rate per unit of turbulent kinetic energy.

Other symbols

Over-bar	Time averaged.
∇	Del operator.

Subscripts

a	Ambient.
avg	Average.
b	Bulk.
B	Body.
c	Cross-section.
ct	Contact.
CFD	Computational Fluid Dynamics.
cyl	Cylindrical plane.
d	Drag.
$Ergun$	Eq. (2.13).
ES	Eqns. (2.15) and (2.16).
g	Gravity.
i	Sphere index.
j	Sphere index.
k	Cross section index.
KTA	Eq. (2.14).
L	Laminar.
m	Modified.
max	Maximum.
min	Minimum.
o	Overlap.
p	Particle.
pg	Pressure gradient.
s	Solid.
sct	Sum of contact.
S	Surface.
t	Total.
T	Turbulent.
ud	User defined.
v	Void.
vm	Virtual mass.
$Wentz$	Eq. (2.18).

Superscripts

L	Total axial length of bed.
$L-2d$	Approximation of the axial length neglecting the length effect: Fig. 5.3.
n	Normal.
t	Tangential.

Vectors

$\mathbf{a}$	Area vector.
$\mathbf{A}$	Outward pointing face area vector.
$\mathrm{d}\mathbf{s}$	Vector connecting two cell centroids.
$\mathrm{d}\mathbf{S}$	Outward pointing surface vector.
$\mathbf{F}$	Force.
$\mathbf{S}$	Strain rate tensor.
$\mathbf{T}$	Reynolds stress tensor.
$\mathbf{u}$	Vector velocity field.
$\mathbf{u}'$	Fluctuating component of $\mathbf{u}$.
$\mathbf{U}$	Mean component of $\mathbf{u}$.

Abbreviations

2D	Two-Dimensional.
3D	Three-Dimensional.
CCA	Continuity Convergence Accelerator.
CFD	Computational Fluid Dynamics.
CT	Computed Tomography.
DEM	Discrete Element Method/Modelling.
DNS	Direct Numerical Simulation.
ES	Eisfeld & Schnitzlein.
KTA	Nuclear Safety Standards Commission ("Kerntechnisher Ausschuss").
LES	Large Eddy Simulation.
MIS	Mesh Independence Study.
NRMSD	Normalised Root Mean Square Deviation.
NWU	North-West University.
PMMA	Poly(methyl methacrylate).
RANS	Reynolds-Averaged Navier-Stokes.
RSM	Reynolds Stress Model.
SEM	Synthetic Eddy Method.

Chapter 1

Introduction

1.1 Background

A packed bed can be described as any fixed container which is packed with particles, where the particles can vary in shape and size. The basic principle of all packed beds is that a working fluid is passed over the bed, between the particles, causing numerous flow-, thermal- and chemical effects. The flow through such a packed bed is applied in many processes in the engineering industry, with examples such as: filtration, ion exchange, drying, heterogeneous catalysis, thermal heat exchangers and nuclear packed bed reactors (Dolejs and Machac, 1995; Mueller, 2010). When considering the design of a fluid-system which incorporates a packed bed, the pressure drop (Δp) over the bed is one of the most important variables which has to be predicted accurately (Winterberg and Tsotsas, 2000), as it is related to the flow distribution, pumping power and operating costs (Hassan and Kang, 2012). For this basic design reason, the flow through packed beds has been the topic of interest for many authors. Ergun (1952) was one of the first authors to summarise the factors which influence the pressure drop over packed beds as: (1) the rate of fluid flow, (2) viscosity and density of the fluid, (3) closeness and orientation of the packing, and (4) size, shape and surface roughness of the particles. Hence, the pressure drop is very sensitive to the geometrical properties of the bed. Considering cylindrical beds consisting of mono-sized spherical particles, the most important geometric properties are: (1) the aspect ratio, $\alpha = D/d$, with D the cylinder diameter and d the particle diameter, and (2) the bed porosity, which is related to the permeability of the bed.

In infinite randomly packed beds, with large aspect ratios, the porosity can be considered uniform. Hence, an assumption often made by designers is that the flow distribution is uniform over the diameter of the bed (Eppinger et al., 2011). However, particles in finite randomly packed beds form ordered packings on the bed boundaries, which result in large variations in porosity in the near-boundary regions. This phenomenon is commonly known as the wall effect, and becomes increasingly prominent at small aspect ratios (Mueller, 2010). Since the wall effect is related to the bed permeability, the flow distribution cannot be assumed to be uniform over the diameter of finite beds. Thus, the wall effect presents numerous difficulties when attempting to predict the pressure drop, as it is Reynolds number dependent (Cheng, 2011). In creeping flow regimes, a decrease in the aspect ratio leads to an increase in the pressure drop, due to additional friction. Whilst in turbulent flow regimes, a decrease in the aspect ratio leads to a decrease in pressure drop, due to higher porosity (Di Felice and Gibilaro, 2004; Reddy and Joshi, 2008).

A number of methods exist to describe the pressure drop over randomly packed beds. The most common method uses a hydraulic diameter concept to calculate the bed friction factor, Ψ, which is analogous to the flow through pipes. Authors who first used this method successfully, to develop semi-empirical correlations that predict the pressure drop over infinite beds, were Carman (1937) and Ergun (1952). These correlations, however, do not take the wall effect into account and present inaccurate predictions at low aspect ratios. Many authors have attempted to improve these correlations to include the wall effect, by fitting semi-empirical correlations to their own experimental data. As a result, a large number of correlations exist, which are commonly categorised as Carman- or Ergun-type equations respectively. Only a few of these correlations are relevant to the current investigation.

The Eisfeld and Schnitzlein correlation is an Ergun-type equation which was derived from more than 2300 experimental data points (Eisfeld and Schnitzlein, 2001). This correlation is relevant to the current investigation as it takes the wall effect into account, and predicts accurate values for the friction factor at low aspect ratios. The Nuclear Safety Standards Commission, "Kerntechnischer Ausschuss" (KTA), also made considerable efforts to develop a Carman-type equation which predicts the pressure drop over packed beds with mono-sized spherical particles (KTA, 1988). The derivation of the correlation was based on the investigation of various correlations from literature. Instead of taking the wall effect into account, KTA (1988) took experimental investigations from various authors and chose points for α and the modified Reynolds number, Re_m, where the influence of the containing walls was negligible. By plotting these values for α against Re_m they were able to estimate a limiting line, which defines the region for which the wall effect is negligible. Fig. 1.1 shows that the KTA correlation is not valid for small aspect ratios, however the theoretical basis for this line is unclear.

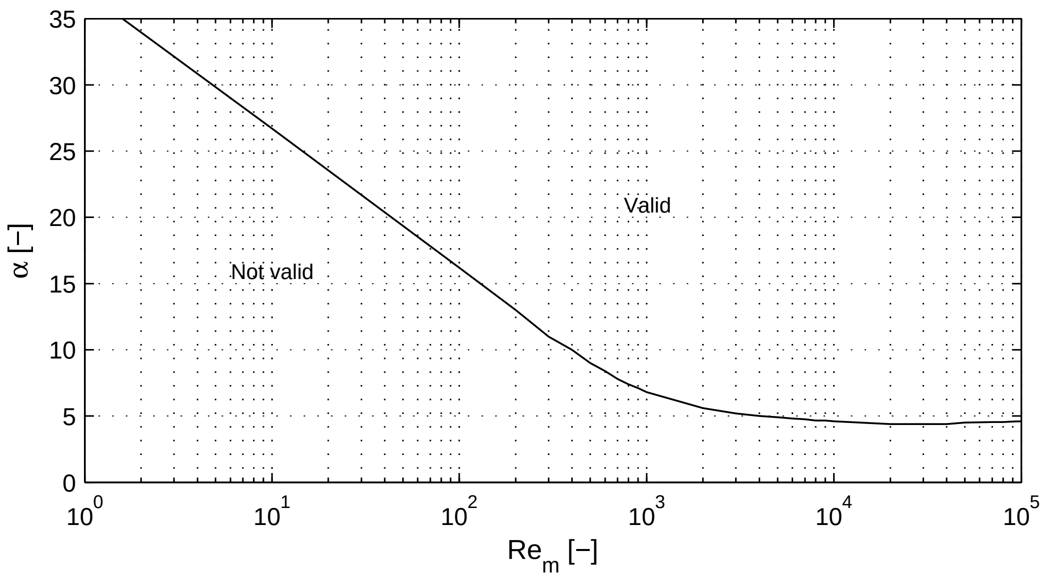

Figure 1.1: Lower limit of the KTA correlation: the KTA limiting line.

1.2 Problem statement

The KTA correlation is a semi-empirical, Carman-type equation which predicts the pressure drop over randomly packed beds, and is well known within the nuclear community. It does not take the wall effect into account, and is not valid for small aspect ratios as shown in Fig. 1.1. However, the KTA (1988) does not present a convincing theoretical basis for this lower limit of the KTA correlation, and thus the validity of the estimated KTA limiting line is uncertain.

1.3 Objectives

The main objective of this investigation was to determine the validity of the KTA limiting line shown in Fig. 1.1, which is the lower limit of the KTA (1981) correlation. Also, if possible, to improve on the definition of the limiting line.

1.4 Methodology

The complexities in the structure of packed beds have thus far prevented the detailed understanding of the flow between bed particles. With recent increases in computational power, Computational Fluid Dynamics (CFD) has become a viable method to analyse the complex flows in packed beds (Reddy and Joshi, 2010). Such CFD analyses require Three-Dimensional (3D) models, and Discrete Element Method (DEM) has shown promise to generate realistic randomly packed beds (Eppinger et al., 2011). Theron (2011) investigated a method to model the flow through packed beds using an explicit approach. Using DEM, he generated beds with aspect ratios of $1.39 \leq \alpha \leq 4.93$, and simulated the flow through each bed. His results for porosity and pressure drop compared well with that found in literature. Theron (2011) showed that the commercial CFD package STAR-CCM+® (CD-Adapco, 2012) provides a stable platform for both DEM and CFD operations, considering the analysis of packed beds.

This investigation was an extension of the work done by Theron (2011). Packed beds were generated using DEM, and the flow through the beds simulated using CFD. STAR-CCM+® was used for both DEM and CFD operations, and the methods developed for this explicit approach were validated with empirical data. The KTA correlation predictions for friction factors were then compared to the CFD results, as well as the Eisfeld & Schnitzlein correlation predictions.

1.5 Overview of document

This document contains detail of the steps taken to reach the objectives described in Section 1.3. Chapter 1 gives a summery of the most relevant literature reviewed, which leads to the problem statement and objectives of this investigation. Chapter 2 presents the literature survey done on the aspects of packed beds that were relevant to this investigation. Geometric properties of packed beds are described, as well as the influence of these properties on the characteristics of the flow through packed beds. Correlations derived to predict the pressure drop through packed beds, and previous investigations that used DEM or CFD to analyse packed beds are also reviewed in Chapter 2. In Chapter 3 the basic theoretical principles of DEM and CFD are briefly described, as they are employed in STAR-CCM+®. Chapter 4 describes the methods developed during this investigation, for the explicit simulation of the flow through packed beds, to ensure accurate results with a reasonable degree of confidence. Particular focus was given to factors such as mesh independence, turbulence modelling and the treatment of contact points between particles. Chapter 4 also contains detail of the setups used for all DEM and CFD simulations. Chapter 5 contains the quality analysis of the DEM generated beds, results from the validation process, and the main results for pressure drop and friction factor from the CFD simulations. Comparisons between the results from the CFD simulations and predictions from correlations described in Chapter 2 are also shown. Chapter 6 concludes the document with a summary of the investigation, conclusions that were made from the results, and recommendations for future studies on the topic.

The objectives of this investigation are stated in Section 1.3. In order to reach these objectives, the first step was to review the literature available on the flow through packed beds. This review is given in the next chapter.

Chapter 2

Literature survey

Many theoretical correlations have been developed in the attempt to accurately predict the pressure drop over cylindrical packed beds. Some of these methods have been proven to be accurate under specific conditions. However, existing correlations which predict the pressure drop over cylindrical packed beds for small aspect ratios do not present values that compare well with the pressure drops from empirical studies. The geometrical complexities of these beds have thus far prevented the detailed understanding of the flow between randomly packed bed particles.

A comprehensive literature survey was done. The goal of the survey was to gain insight and understanding of packed bed structures, methods to predict pressure drops and the discrepancies between theoretical and empirical studies.

2.1 Packed bed definition

A packed bed can be described as a fixed column or cylinder which is packed with particles, where the particles can vary in shape and size. The basic principle of all packed beds is that a working fluid is passed over the bed, thus between the particles, causing numerous flow-, thermal- and chemical effects. The flow through such a packed bed is applied in many processes in the engineering industry, with examples such as: filtration, ion exchange, drying, heterogeneous catalysis, thermal heat exchangers and nuclear packed bed reactors (Dolejs and Machac, 1995; Mueller, 2010).

The design of a packed bed is heavily dependent on the pressure drop of the fluid over the bed, mechanisms of heat and mass transfer, and in some cases mechanisms of chemical reactivity. When considering the design of a fluid-system which incorporates a packed bed, the pressure drop over the bed is one of the crucial variables which have to be predicted accurately (Winterberg and Tsotsas, 2000; Eisfeld and Schnitzlein, 2001). All the design considerations, including pressure drop, are influenced by the bed structure.

2.2 Packed bed structure

The structure of a cylindrical packed bed consisting of mono-sized spherical particles can be described with a number of methods. Though the most common of the methods are the aspect ratio and porosity, some other methods are described in this section as well.

2.2.1 Aspect ratios

The aspect ratio, α, of a packed bed is the ratio of the cylinder diameter, D, to the diameter of the particles, d:

$$\alpha = \frac{D}{d} \tag{2.1}$$

This definition of the aspect ratio is only applicable to cylindrical packed beds, with mono-sized spherical particles. This ratio is arguably the most important parameter which characterises a cylindrical packed bed, since it is directly related to the bed porosity and packing structure, which in turn influences the permeability of the bed.

2.2.2 Porosity

Porosity, ε, also known as the void fraction, is characterised as a volumetric structural property and has a value between 0 and 1. It is a basic packing parameter of fixed packed beds that gives an indication of the volume available for fluid flow, and the permeability of the bed (Mueller, 1997). Porosity is defined as the fraction of the volume of voids to the total volume. Thus,

$$\varepsilon_b = \frac{V_v}{V_t} = \frac{V_t - V_s}{V_t} = 1 - \frac{V_s}{V_t} \tag{2.2}$$

where ε_b is the bulk porosity, V_v the volume of the voids, V_s the solid volume and V_t the total volume, as defined by Mueller (2010).

Bai et al. (2009) gave an analytical expression to calculate the bulk porosity of beds consisting of mono-sized spherical particles, where N is the number of particles and L the axial length of the bed:

$$\varepsilon_b = 1 - \frac{2Nd^3}{3LD^2} \tag{2.3}$$

Du Toit (2008) developed analytically-based numerical procedures to evaluate the variation in the porosity of a cylindrical packed bed consisting of spherical particles in the axial and radial directions, when the centre coordinates and diameters of the particles are known. The axial porosity $\varepsilon(z)$ at a given level z is given as:

$$\varepsilon(z) = 1 - \frac{\sum A_i(z)}{A_c(z)} \tag{2.4}$$

where $A_c(z)$ is the cross-section area of the cylinder at level z, and $A_i(z)$ the area of the intersection between the sphere i and the axial plane. The radial porosity $\varepsilon(r)$ at a given radial position r is given as:

$$\varepsilon(r) = 1 - \frac{\sum A_i(r)}{A_{cyl}(r)} \tag{2.5}$$

with $A_{cyl}(r)$ is the area of the cylindrical plane at the radius r between axial heights z_1 and z_2, and $A_i(r)$ the area of the intersection between the sphere i and the cylindrical plane. These procedures provide the area-based porosity at the selected positions as opposed to the volume-based porosity obtained by Mueller (1992).

Du Toit and Rosslee (2012) used eq. (2.6) to calculate the bulk porosity of packed beds numerically, where z_{min} to z_{max} are the minimum and maximum axial coordinates respectively and z' the number of planes from z_{min} to z_{max}.

$$\varepsilon_b = \frac{\sum_{k=1}^{z'-1}\left[\frac{1}{2}\cdot\left(\varepsilon(z_k)+\varepsilon(z_{k+1})\right)\cdot\left(z_{k+1}-z_k\right)\right]}{\left(z_{max}-z_{min}\right)} \tag{2.6}$$

2.2.3 Packing

Graton and Fraser (1935) showed that when systematically packing spherical particles, various layouts can occur in a single layer of spheres. The most basic being the square and simple rhombic layouts, as shown in Fig. 2.1.

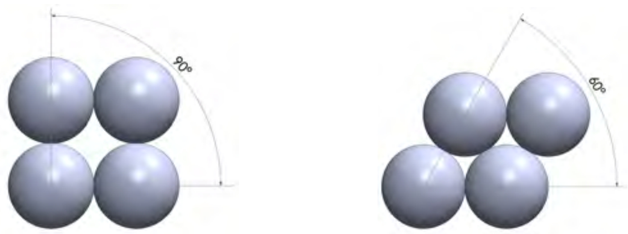

(a) Square. **(b)** Rhombic.

Figure 2.1: Types of layers formed by spherical particles.

From these two configurations in a layer, several different 3D structures can be obtained. These packings are shown in Fig. 2.2. The structures for cases 1, 2 and 3 are shown as resting on square layers, and cases 4, 5 and 6 on simple rhombic layers.

The structures shown in Fig. 2.2 are idealistic packings without the influence of external boundaries. Graton and Fraser (1935) noted that spheres packed in a cylinder are unable to start and retain any simple structural packing due to the interference of the cylinder wall. As the influence of the cylinder wall on the structure is propagated throughout the entire packing, only small regions of case 6 packings (Fig. 2.2f) could be observed. Thus, the structure in cylindrical packed beds of mono-sized spherical particles can typically be considered as random. Mueller (1992) also noted that packings far from the cylinder wall display a randomised configuration.

(a) Case 1: Cubic. **(b)** Case 2: Orthorhombic. **(c)** Case 3: Rhombohedral.

(d) Case 4: Orthorhombic. **(e)** Case 5: Tetragonal. **(f)** Case 6: Rhombohedral.

Figure 2.2: Packing structures.

Regarding the density between packed bed packings, two different types can be obtained namely loose packings and dense packings (De Klerk, 2003). Loose packings are obtained when the particles are simply dropped into the container and left to settle only through gravity. Dense packings are obtained when the container is tapped or shaken after the particles were added, forcing the particles to shift and form a more rigid packing.

2.2.4 Voronoi tessellation

Voronoi (1908) developed a concept that indicates the distinctive features of particle arrangements by tessellating the packing into so-called Voronoi polyhedra. A Voronoi polyhedron is the shape obtained via spacial discretization of the space between adjacent particles, each with the following features (Voronoi, 1908; Cheng et al., 1999; Cheng and Yu, 2013):

1. A boundary plane of the polyhedron is a perpendicular bisector of the line segment which joins the element point to a neighbouring element point.
2. A side of the polyhedron is the line segment which is equidistant from the element point and two neighbouring element points.
3. A vertex of the polyhedron is the point which is equidistant from the element point and three neighbouring element points.
4. When a new point is arbitrarily given in the space divided into the Voronoi polyhedra, the closest element point to this point is that of the Voronoi polyhedron which contains this point.
5. When the element points are located arbitrarily, the polyhedra obtained are convex and their shapes vary according to the arrangement of the element points.

When these features are applied to randomly packed beds consisting of mono-sized spherical particles, the element points are the centroids of the particles. Fig. 2.3 shows schematically the features of Voronoi tessellation for a Two-Dimensional (2D) packing and a typical 3D Voronoin polyhedron.

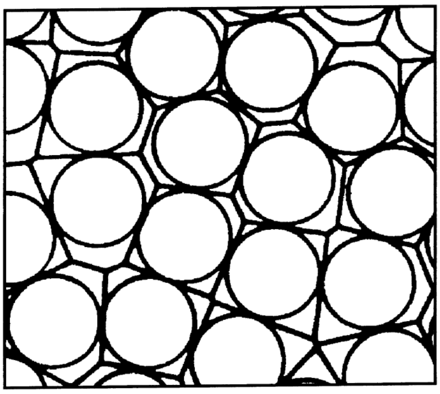

(a) Voronoi tessellation of a 2D packing.

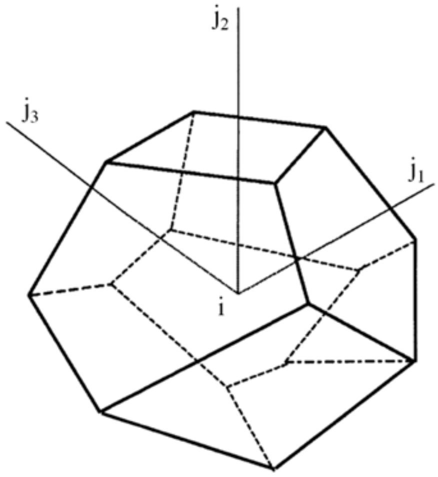

(b) Typical 3D Voronoi polyhedron. Each face represents a connection between particles, e.g. particle i with particles j_1, j_2, j_3 etc.

Figure 2.3: Schematic illustration of Voronoi tessellation in (a) two and (b) three dimensions (Cheng et al., 1999).

In order to simplify modelling the heat transfer between particles, Cheng et al. (1999) used Voronoi tessellation to represent randomly packed beds in the form of Voronoi polyhedra. They then model the heat transfer within a polyhedron and between neighbouring polyhedra. Cheng et al. (1999) focussed on the effective thermal conductivity due to conduction between particles, and Cheng and Yu (2013) proposed a numerical approach to calculate the radiation heat transfer between particles based on Voronoi tessellation. Though the Voronoi polyhedra has been of great importance in the analysis of the heat transfer between packed bed particles, it is not relevant for the current explicit investigation of the flow through packed beds.

2.2.5 Coordination number

The coordination number is defined as the number of particles in contact with the particle under consideration, and is useful to model transport phenomena through packed beds. Du Toit et al. (2009) made a summary of the correlations proposed by various authors to predict the average coordination number, as a function of the bulk porosity. They observed significant differences when the coordination numbers predicted by these correlations were compared with one another. They also showed that the coordination number in the near wall region differs significantly from that predicted by the correlations for the bulk region.

2.2.6 Contact angles between adjacent particles

Du Toit et al. (2009) also defined a contact angle between two particles in contact with each other as the angle between the line connecting the particle centroids, and the line perpendicular to the direction of the heat flux. Thus, a contact angle of $0°$ implies that the heat transfer between two particles in contact does not contribute to the heat flux in the relevant coordinate system, and on the other hand a contact angle of $90°$ implies maximum contribution to the heat flux. Though using contact angles holds potential in simulating the effective thermal conductivity between adjacent particles, it is not of great relevance for the current investigation.

2.3 Porosity variations

As mentioned in Section 2.1, the design of a packed bed is based on the pressure drop of the fluid through the bed as well as mechanisms of heat and mass transfer. These mechanisms are all influenced by the bed porosity (Du Toit, 2008). For flow through a porous medium the permeability increases with the porosity (White and Tien, 1987).

2.3.1 Porosity variations in the radial direction

Radial porosity variations is a geometrical characteristic of packed beds and is particularly prominent at aspect ratios of $\alpha \leq 10$ (Mueller, 1997; De Klerk, 2003). These variations occur because of the influence of the cylinder walls, see Section 2.3.2. Radial porosity variations for cylindrical packed beds with mono-sized spheres have been investigated using various experimental and systematic methods (Mueller, 2010). Most of these investigations assume axi-symmetry and average the porosity tangentially.

Experimental investigations

Roblee et al. (1958) performed the first experiments to investigate the variation of porosity in the radial direction in randomly packed beds. This was achieved by packing cork spheres into a cardboard cylinder which was then filled with paraffin wax. After solidification, slabs were cut from the bed and each slab cut into annular rings. These annular rings were used to determine the fraction of voids (wax). The cylinder wall had a definite influence on the porosity of the bed. Oscillatory variations of the porosity was observed further than 2 particle diameters into the bed, the amplitude decreasing with increasing distance from the wall.

Benenati and Brosilow (1962) made packed beds by filling cylindrical containers with lead shot. The bed voids were then filled with epoxy resin and left to cure. The solid cylinder was then machined in stages to successively smaller diameters and the weight loss noted. They found that the porosity distribution took the form of a damped oscillatory wave with a maximum of 1.0 at the wall and the oscillations damped out at roughly 4 to 5 particle diameters from the wall.

Ridgway and Tarbuck (1966) followed a technique whereby a cylinder with balls was revolved at speeds of over 1000 rpm. Measuring the thickness of an annular layer of water, whilst gradually adding water, the radial porosity distribution was calculated. Their results were similar to that of Benenati and Brosilow (1962), with the porosity showing damped oscillatory behaviour within 5 particle diameters from the wall.

Goodling et al. (1983) made packed beds by filling a cylindrical plastic pipe with polystyrene spheres and then filling the voids with a mixture of epoxy and finely ground iron particles. After hardening, thin annular rings were cut from the bed perimeter over the whole length on a lathe. Noting the weight loss after each cut. They also found the porosity to show damped oscillatory behaviour within 5 particle diameters of the wall.

Sederman et al. (2001) used magnetic resonance imaging volume-visualisation in combination with image analysis techniques to analyse the porosity distribution in cylindrical packed beds filled with ballotini spheres. Their results were similar to that of Goodling et al. (1983).

The porosity variations in the near wall region of cylindrical packed beds have been experimentally investigated by numerous researchers. De Klerk (2003) compiled the radial porosity distributions obtained by some of the researchers mentioned above, see Fig. 2.4. He concluded that, even though the experimental work was approached in different ways, the results were in general agreement.

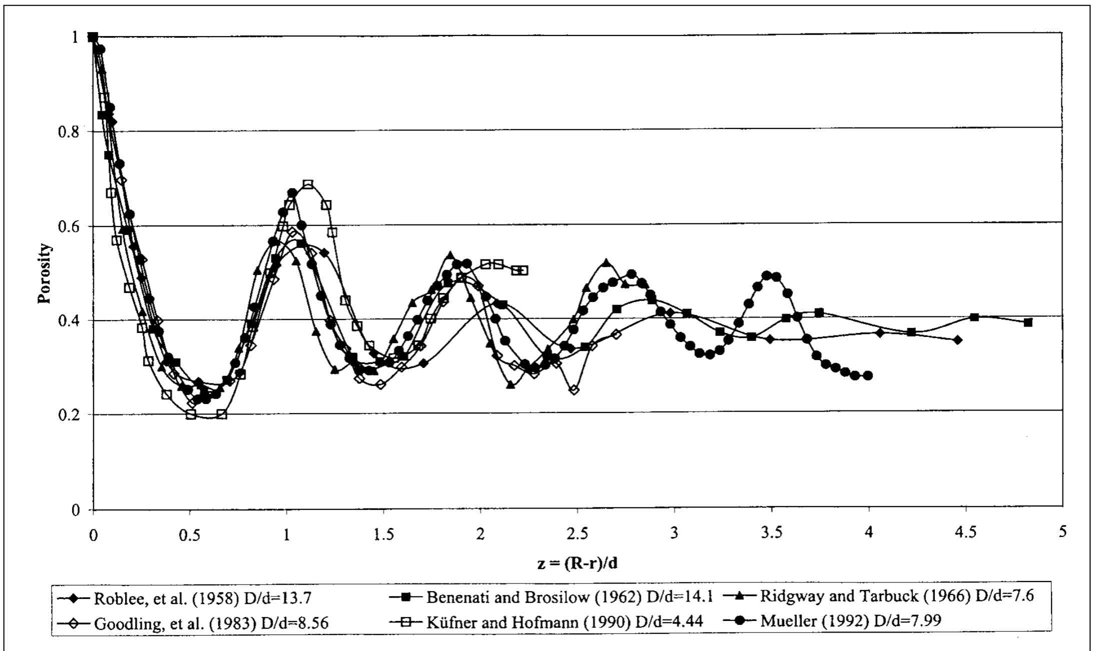

Figure 2.4: Radial porosity variation, De Klerk (2003).

Modelling of porosity variations

Various attempts at modelling the near-wall porosity variations have been presented in literature. These efforts to predict the porosity vary from entirely empirical in nature to semi-analytical predictive expressions (Mueller, 2012). Most of the recent models succeed in describing both the oscillatory and damping characteristics of the porosity variations (De Klerk, 2003).

Van Antwerpen et al. (2010) gives a summary of relevant correlations to determine the oscillatory porosity variations in cylindrical packed beds. They also concluded that there is a tendency to move away from purely empirical correlations to the analysis of numerically simulated packed beds. However, what is of importance is that methods do exist which make it possible to obtain the radial porosity variations in a cylindrical packed bed of spherical particles, when the coordinates of the centres of the spheres are known.

2.3.2 Effect of cylinder wall on porosity

As mentioned in Section 2.3.1, Benenati and Brosilow (1962) performed an experimental study to obtain the radial porosity distribution in packed beds. They found that the porosity distribution took the form of a damped oscillatory wave which damped out at roughly 5 particle diameters from the wall. They also investigated the porosity variations in the radial direction in large packed beds containing a central steel rod. They observed the same oscillatory behaviour of the porosity regardless of whether it was the inner surface (steel rod) or the outer surface (cylinder wall). This showed that the presence of any distinct boundary or wall causes the observed oscillatory porosity variations.

Mariani et al. (2009) used Computed Tomography (CT) techniques to obtain the particle centre distribution for a packed bed with an aspect ratio of $\alpha = 5.04$. They found that the first layer of particles adjacent to the wall was highly ordered, with almost all of the particle centres being at a distance of a particle radius from the wall. The second layer showed a definite disorder in the distribution of the particle centres in the radial direction. This development of decreasing order in the positions of the particle centres from the cylinder wall continues toward the centre of the bed.

Mueller (2010) presented a particle centre distribution for a packed bed with an aspect ratio of $\alpha = 7.99$. His findings was similar to that of Mariani et al. (2009), as shown in Fig. 2.5.

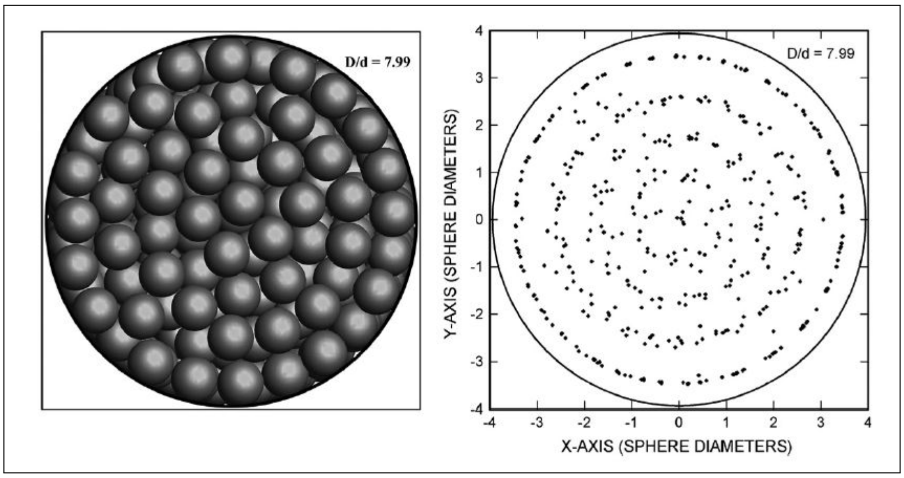

Figure 2.5: Distribution of the centre coordinates of the spheres of a bed with $\alpha = 7.99$, Mueller (2010).

Wensrich (2012) also used CT scans of packed beds with various aspect ratios to examine the effect of the cylinder boundaries on the packing structure. As with previous studies, they found the particles against the wall to have a great deal of order. This is because the wall, which is two-dimensional in nature, forces a two-dimensional ordered structure in the first layer of particles.

2.3.3 Porosity variations in the axial direction

As mentioned in Section 2.3.2, the presence of any distinct boundary or wall in a packed bed causes oscillatory porosity variations near the wall due to the ordered structure of the packing of the near wall particles. This is also true for the top/bottom walls of the bed.

Zou and Yu (1995) described the influence on the porosity variations in a cylindrical packed bed, due to the top/bottom walls as well as the length of the bed, as the length effect. They observed that most investigations on porosity variations in packed beds considered only the side wall effect, whilst implicitly assuming the length effect to be negligible. They also stated that the error due to this assumption is usually small, but must be considered when the length of the bed is small compared to its diameter. Zou and Yu (1995) studied the influence of the bed length to particle diameter ratio (L/d) on the bulk porosity by considering a packed bed with an aspect ratio of $\alpha = 24.66$. They found that for $L/d \leq 20$ the bulk porosity increased from $\varepsilon_b = 0.395$ to $\varepsilon_b = 0.46$ at $L/d = 2.5$.

2.3.4 Porosity variations as a function of the aspect ratio

Leva and Grummer (1947) made packed beds using a steel pipe and glass spheres. Knowing the number of particles in the bed, particle diameter, packing height and cylinder diameter they calculated the bed average porosity. Using this method they measured the average porosity of numerous beds with different aspect ratios, for loose and dense packings.

De Klerk (2003) performed similar experiments as Leva and Grummer (1947), with loose packings. Fig. 2.6 shows that they observed similar results. It is clear that the average bed porosity increases for $\alpha \leq 12$.

Dixon (1988) made packed beds with aspect ratios of $1 \leq \alpha \leq 10$, and measured the bulk porosity of each bed using a weighing method. He repeated the experiment for each aspect ratio with two different cylinder lengths, in order to eliminate the length effect. Using his own measurements, as well as data from literature, he derived correlations which predict the bulk porosity of packed beds, as a function of the reciprocal of the aspect ratio. The correlation by Dixon (1988) which predicts the bulk porosity is shown in eq. (2.7), where d/D is the reciprocal of α. Fig. 2.7 shows a plot of the bulk porosities predicted by eq. (2.7).

$$\varepsilon_b = \begin{cases} 0.4 + 0.05\,(d/D) + 0.412\,(d/D)^2 & \text{for} \quad d/D \leq 0.5 \\ 0.528 + 2.464\,((d/D) - 0.5) & \text{for} \quad 0.5 \leq d/D \leq 0.536 \\ 1 - 0.667\,(d/D)^3\,(2\,(d/D) - 1)^{-0.5} & \text{for} \quad 0.536 \leq d/D \end{cases} \tag{2.7}$$

Benyahia and O'Neill (2005) measured the bulk porosities of packed beds with aspect ratios of $1.5 \leq \alpha \leq 50$, using a water displacement method. Using their measurements, they also

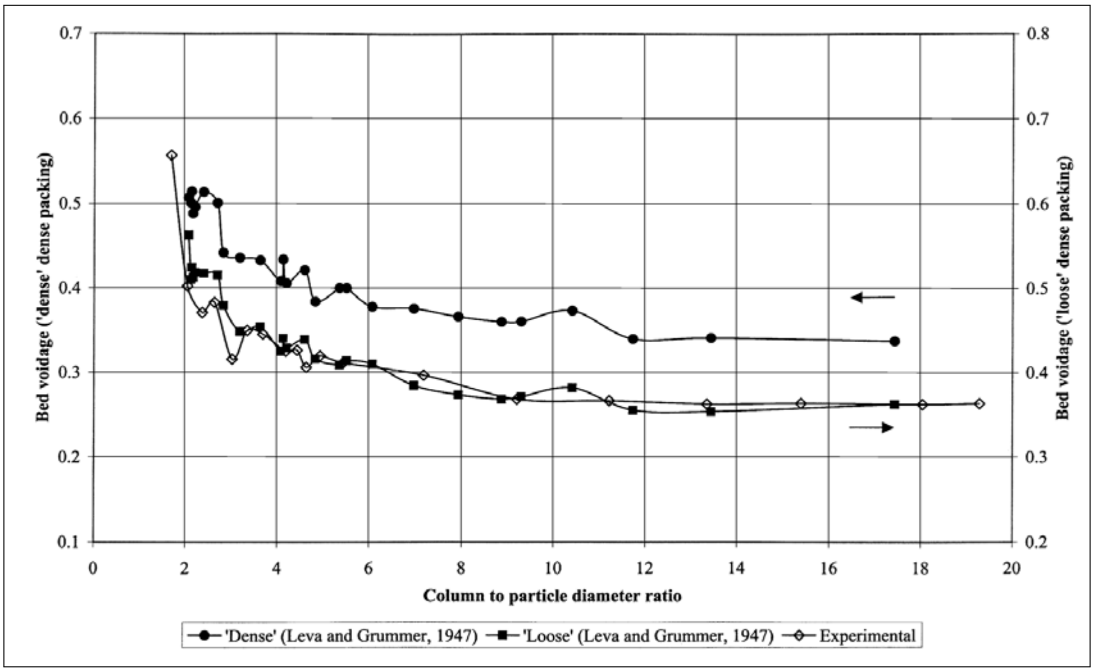

Figure 2.6: Average bed porosity as a function of the aspect ratio, De Klerk (2003).

developed a correlation, eq. (2.8), which predicts the bulk porosity of packed beds, as a function of the aspect ratio.

$$\varepsilon_b = 0.39 + \frac{1.74}{(\alpha + 1.14)^2} \tag{2.8}$$

Fig. 2.7 shows the bulk porosities predicted by eqns. (2.7) and (2.8), by Dixon (1988) and Benyahia and O'Neill (2005) respectively. It should be noted that both Dixon (1988) and Benyahia and O'Neill (2005) used packed beds long enough to eliminate the length effect.

2.3.5 Conclusions on porosity

Considering the literature mentioned in this section, the following important conclusions can be made regarding the porosity variations in cylindrical packed beds consisting of mono-sized spherical particles:

1. Particles in the near wall region have an ordered packing due to the two-dimensionality of the wall.
2. The porosity varies in an oscillatory fashion in the near-wall region.
3. The amplitude of the oscillations are increasingly damped out as the distance from the wall increases.
4. The presence of any distinct boundary or wall causes the above mentioned oscillatory porosity variations.

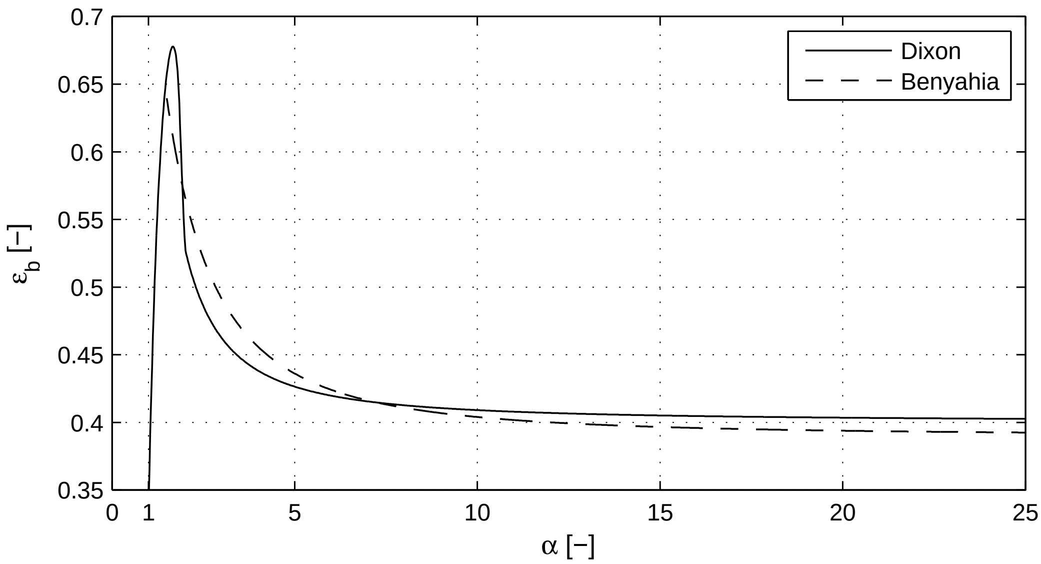

Figure 2.7: Bulk porosities predicted by Dixon (1988) and Benyahia and O'Neill (2005).

5. Methods do exist which make it possible to obtain the radial porosity variations, when the coordinates of the centres of the spheres are known.

6. Due to the nature of randomly packed beds, the porous structure of a packed bed will be unique. However, packed beds may be described in terms of general characteristic parameters for system design purposes.

2.4 The wall effect

Porosity variations in the near wall region of a packed bed have profound effects on the fluid flow, thus the flow characteristics in the near wall region is different from that in the bulk region. This phenomenon is referred to as the wall effect, even though an explicit definition for the wall effect cannot be found in literature. As the porosity variations in the near wall region become larger with decreasing aspect ratios (see Fig. 2.6), so does the influence of the wall effect on the fluid flow. The wall effect is an important factor when considering the analysis and design of equipment which uses beds with low aspect ratios (Mueller, 1992).

Mehta and Hawley (1969) noted that the influence of the wall effect is small for large aspect ratios, but become larger for $\alpha < 50$. Cohen and Metzner (1981) on the other hand said that the wall effect can be neglected for $\alpha > 30$. Though the exact limit where the wall effect may be neglected is uncertain, Cohen and Metzner (1981) and Mueller (1997) noted that for $\alpha \leq 10$ there is no definite bulk region, and wall effects are significant across the whole bed.

Cohen and Metzner (1981) proposed a multi-regional model which describes the pressure drop over beds, and observed an increase in fluid velocity in the near wall region. White and Tien (1987) predicted the velocity profile using a closed-form solution from the volume averaged second order momentum equation, and also observed a sharp peak in the velocity near the wall, as shown in Fig. 2.8. Winterberg and Tsotsas (2000) stated that with the increased

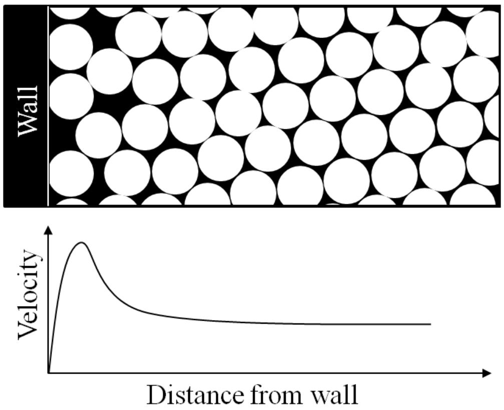

Figure 2.8: Schematic illustration of a packed bed with a typical velocity profile in the near wall region, White and Tien (1987).

porosity in the near wall region the permeability of the bed also increases, and hence also the fluid velocity. However, Winterberg and Tsotsas (2000) also noted that viscous friction in the wall region is complex and cannot be neglected.

It has been concluded that the wall effect has two contradicting effects on the pressure drop. In creeping flow regimes the pressure drop may increase due to the additional wall friction. On the other hand, in turbulent regimes the pressure drop may decrease due to the increased porosity and permeability (Eisfeld and Schnitzlein, 2001; Di Felice and Gibilaro, 2004). Thus the wall effect is Reynolds number dependent (Cheng, 2011). Experimental observations in this respect have been reviewed by Eisfeld and Schnitzlein (2001).

2.5 Prediction of pressure drop

Predicting the pressure drop has been the topic of many theoretical and experimental studies, and general agreement has been achieved on how to describe the influence of the Reynolds number and the bulk porosity on the pressure drop through infinite beds. However, the exact influence of the wall effect is still uncertain (Eisfeld and Schnitzlein, 2001). A common method to address this problem is to use experimental data to build correlations based on dimensionless variables that attempt to predict the pressure drop.

2.5.1 Background

One of the most common methods used to describe the pressure drop through packed beds makes use of the hydraulic diameter concept proposed by Blake (1922), which is analogous to the flow through pipes. Blake (1922) proposed two dimensionless groups to characterise the pressure loss through packed beds:

$$\Psi = \frac{\Delta p}{\rho U^2} \cdot \frac{d}{L} \cdot \frac{\varepsilon_b^3}{1 - \varepsilon_b} = \frac{\Delta p}{\rho U_i^2} \cdot \frac{D_H}{L} \tag{2.9}$$

$$Re_m = \frac{Re_p}{1-\varepsilon} \qquad ; \qquad Re_p = \frac{\rho U d}{\mu} \tag{2.10}$$

with U_i the interstitial velocity, U the superficial velocity, D_H the hydraulic diameter, Re_p the particle Reynolds number, ρ the fluid density and μ the fluid dynamic viscosity. The two groups, Ψ and Re_m, are known as the modified friction factor and the modified Reynolds number respectively. However, the hydraulic diameter concept suggested by Blake (1922) was derived for infinite beds, and excluded the effect of the wall on the hydraulic diameter. Also, Ergun (1952) stated that these early attempts to describe the pressure drop through packed beds failed, because they did not consider the fact that the pressure drop is caused by simultaneous kinetic and viscous effects.

2.5.2 Types of equations

Reynolds (1900) was the first to correlate the resistance offered by friction to the motion of the fluid as the sum of the viscous and kinetic energy losses:

$$\frac{\Delta p}{L} = a\mu U + b\rho U^n \tag{2.11}$$

with the term $a\mu U$ representing viscous energy losses, $b\rho U^n$ kinetic energy losses, and $n = 2$. Various authors have found the viscous energy loss to be proportional to $(1-\varepsilon_b)^2/\varepsilon_b^3$ and the kinetic energy loss to $(1-\varepsilon_b)/\varepsilon_b^3$. Ergun (1952) expressed these proportionalities as:

$$a = a' \cdot \frac{(1-\varepsilon_b)^2}{\varepsilon_b^3} \qquad ; \qquad b = b' \cdot \frac{(1-\varepsilon_b)}{\varepsilon_b^3} \tag{2.12}$$

where values for a' and b' were obtained empirically. Substituting eq. (2.12) into eq. (2.11), and rewriting in terms of the friction factor for the general case yields:

$$\Psi = \frac{\Delta p}{\rho U^2} \cdot \frac{d}{L} \cdot \frac{\varepsilon_b^3}{1-\varepsilon_b} = \frac{a'}{Re_m} + \frac{b'}{(Re_m)^{2-n}} \tag{2.13}$$

Eq. (2.13) is the most general form of the friction factor for fluid flow through packed beds, based on the hydraulic diameter concept. Two main variations exist on this general form:

1. Ergun-type equations.
   Ergun-type equations are variations of eq. (2.13) for which $n = 2$, as originally proposed by Reynolds (1900). These equations are arguably the most widely used correlations to predict the pressure drop through packed beds.

2. Carman-type equations.
   Carman-type equations are variations of eq. (2.13) for which $1.9 \leq n \leq 1.95$, as proposed by Carman (1937).

Known as the Ergun equation, Ergun (1952) originally obtained values for the constants as $a' = 150$ and $b' = 1.75$, by fitting eq. (2.13) to 640 experimental data points. These data points included pressure drop measurements for the flow through beds packed with particles of various shapes and sizes, such as various sized spheres, sand and pulverized coke. The Ergun equation is valid within the ranges of $1 < Re_p < 2500$ and $0.36 \leq \varepsilon_b \leq 0.4$.

The Ergun equation, however, assumes the influence of the containing walls to be negligible and does not take the wall effect into account. As a result, many researchers have fitted eq. (2.13) to their own experimental data for beds with different aspect ratios, attempting to include the wall effect in the empirically determined constants a' and b'. Therefore, a large number of these correlations exist, of which only a few are relevant for the current investigation.

Carman (1937) originally obtained values for the constants as $a' = 180$ and $b' = 2.871$, which is known as the Carman equation. Even though a number of variations of Carman-type equations do exist, they are less known and have not received as much attention or credit as Ergun-type equations.

2.5.3 The KTA correlation

A 50-member German research group known as the Nuclear Safety Standard Commission, "Kerntechnischer Ausschuss" (KTA), made a considerable effort to develop a correlation which predicts the pressure drop over packed beds consisting of mono-sized spherical particles, over a large range of Reynolds numbers (KTA, 1988). The derivation of the correlation was based on the investigation of various correlations from literature. The new correlation was obtained from a regression analysis of the semi-empirical data obtained from each correlation. The correlations used in the analysis had to adhere to the following criteria:

- The wall effect had to be negligible.
- The bulk porosity had to be known from the original documents.
- All beds had to have length to particle diameter ratios of $L/d > 4$.
- Correlations had to be developed from randomly packed beds.
- Experiments with $d < 1$ mm were not considered.

In order to ensure that the wall effect was indeed negligible, KTA (1988) took experimental investigations from various authors and chose points for α and Re_m where the influence of the containing walls was reported to be negligible. By plotting these values for α against Re_m, they were able to estimate the KTA limiting line (Fig. 1.1), which indicates the range above which the wall effect is negligible. However, the theoretical basis for this line is unclear.

From the regression analysis of the semi-empirical data obtained from each correlation, KTA (1988) proposed a new correlation with values for the constants as $a' = 160$, $b' = 3$ and $n = 1.9$:

$$\Psi_{KTA} = \frac{160}{Re_m} + \frac{3}{(Re_m)^{2-1.9}} \tag{2.14}$$

Eq. (2.14) is known as the KTA correlation, which is a Carman-type equation (KTA, 1981). The KTA correlation is valid for cylindrical packed beds containing mono-sized spheres, within the following limits:

- Reynolds number: $10^0 < Re_m < 10^5$.
- Porosity: $0.36 < \varepsilon < 0.42$.
- Bed length: $L > 5d$.
- Aspect ratios above the limiting line in accordance with Fig. 1.1.

2.5.4 The Eisfeld and Schnitzlein correlation

Eisfeld and Schnitzlein (2001) investigated the influence of the cylinder wall on the pressure drop, with the goal of establishing which existing correlations are valid when the wall effects are not negligible. They made a comparison between the predictions of 24 published pressure drop correlations, including both Ergun- and Carman-type equations, with more than 2300 experimental data points. Assuming an Ergun-type equation to be valid, they found that the Reichelt (1972) approach of modifying eq. 2.13 was the most promising. Eisfeld and Schnitzlein (2001) improved on the Reichelt (1972) equation, and determined values for the constants in the correlation, to obtain the best fit for the correlation's predictions to the experimental data. They stated that their improved correlation does not degrade for small aspect ratios of $\alpha \leq 10$. Eqns. (2.15) and (2.16) is the correlation proposed by Reichelt (1972), with the modifications by Eisfeld and Schnitzlein (2001), where E and E' are functions which account for the wall effect. Eisfeld and Schnitzlein (2001) found the constants to be $e = 154$, $e' = 1.15$ and $e'' = 0.87$ for spherical particles.

$$\Psi_{ES} = \frac{e \cdot E^2}{Re_p} \cdot (1 - \varepsilon_b) + \frac{E}{E'} \tag{2.15}$$

$$E = 1 + \frac{2}{3\alpha\,(1 - \varepsilon_b)} \qquad ; \qquad E' = \left(e'\alpha^{-2} + e''\right)^2 \tag{2.16}$$

Eq. (2.15), the Eisfeld & Schnitzlein (ES) correlation, is the most important Ergun-type equation considered in this investigation, as it is valid within the following limits:

- Reynolds number: $0.01 < Re_p < 17635$.
- Porosity: $0.33 < \varepsilon < 0.882$.
- Aspect ratios: $1.624 \leq \alpha \leq 250$.

Finally, Eisfeld and Schnitzlein (2001) found that the Carman-type equations generally presented slightly better results for spherical particles. However, neither fitting the coefficients of the Carman-type equations nor combining them with the wall correction approach, eq. (2.16), could improve the results relative to that based on the Ergun-type equation.

2.5.5 The Wentz and Thodos correlation

It is uncertain whether or not the same general pressure drop correlations apply for the flow through structured packed beds, since little research has been done on the subject. However, Wentz and Thodos (1963) did thorough experiments on the flow through structured packed beds consisting of mono-sized spherical particles. They took pressure drop measurements for the flow through beds arranged in cubic, body-centred cubic and face-centred cubic orientations. Their beds were made of plastic phenolic spheres, which were fixed in space with short lengths of wire. Each packing arrangement had five layers of particles in the axial direction. The beds were machined to fit into a cylindrical wind tunnel by removing excess portions of the external spheres, to eliminate the wall effect. Wentz and Thodos (1963) used their experimental data to empirically correlate the friction factor to the Reynolds number for the total pressure drop across the bed:

$$\Psi = \frac{0.396}{Re_m^{0.05} - 1.2} \tag{2.17}$$

Wentz and Thodos (1963) also took pressure drop measurements for a single layer of particles in the middle of each bed, to eliminate any entrance and exit effects. From these measurements, they obtained the following correlation:

$$\Psi_{Wentz} = \frac{0.351}{Re_m^{0.05} - 1.2} \tag{2.18}$$

In this investigation eq. (2.18) is considered as the Wentz and Thodos correlation, because it was derived from measurements which eliminated any entrance and exit effects.

2.5.6 Final remarks

Many authors have attempted to derive correlations based on dimensionless variables which can be used to predict the pressure drop over packed beds. However, the exact influence of the wall effect is still uncertain (Eisfeld and Schnitzlein, 2001). Also, many authors have compared the predictions of various correlations to measurements from numerous experiments. However, it is important to note that due to the nature of randomly packed beds, the porous structure of a packed bed will be unique. This introduces a source of error in the prediction of the pressure drop, regardless of the method (Hassan and Kang, 2012).

2.6 Discrete Element Modelling

First introduced by Cundall and Strack (1979), Discrete Element Modelling (DEM) is an explicit numerical scheme which simulates the dynamic and static behaviour of assemblies of particles based on contact mechanics. It is usually assumed that particles displace independently, interact only at contact points and are rigid bodies.

Zhu et al. (2007) reviewed the theoretical developments in DEM up to 2006. They noted the two most common types of DEM: soft particle and hard particle approaches. Cundall and Strack (1979) originally developed the soft particle approach in which particles are permitted to suffer minute deformations. These deformations are used to calculate elastic, plastic and frictional forces between particles. With the hard particle approach, a sequence of collisions is processed, one collision at a time. Being instantaneous, often the forces between particles are not explicitly considered. Zhu et al. (2007) also noted that DEM, particularly the soft particle approach, has been extensively used to study various phenomena, such as particle packing, heaping and piling processes, hopper flow and mixing. They also stated that the models for calculating the contact forces between particles have improved and that more forces have been implemented, which makes DEM more applicable to particulate research. For more information, Section 3.1 gives a theoretical background of DEM as employed in STAR-CCM+®.

With regards to DEM used in studying packed beds, Eppinger et al. (2011) generated randomly packed beds by initialising spherical particles within a cylindrical domain, which dropped to the bottom of the tube due to gravity. For each particle a force balance was solved which took into account the forces of gravity, interaction between particles and interaction between particles and the cylinder wall. They found good agreement for global bed porosity and radial porosity distributions between their DEM results and results found in literature. Theron (2011) investigated the capability of STAR-CCM+® to perform DEM simulations. He generated randomly packed beds with aspect ratios of $1.39 \leq \alpha \leq 4.93$, using a similar method as Eppinger et al. (2011), and validated the results using experimental data. The DEM results compared well with the experimental data and showed similar trends for porosity variations in the axial direction. Theron (2011) concluded that DEM is an appropriate tool for simulating packed bed arrangements.

2.7 Computational Fluid Dynamics

Computational Fluid Dynamics (CFD) is the analysis of systems involving fluid flow, heat transfer and associated phenomena such as chemical reactions by means of computer based simulations (Versteeg and Malalasekera, 2007). CFD allows for the explicit simulation of fluid flow between packed bed particles, taking each particle's position and geometric properties into account. With the tremendous increase in computational power, and the parallel development of various numerical techniques, CFD has become a viable method to analyse the complex flows in packed beds (Eppinger et al., 2011; Reddy and Joshi, 2010).

2.7.1 CFD and packed beds

Calis et al. (2001) used a commercial CFD package to simulate the flow through structured packed beds consisting of 16 particles and aspect ratios of $1 \leq \alpha \leq 2$. The local velocity profile on a cross section of the bed, predicted by the CFD simulation, agreed well with the profile measured in their experimental study. They concluded that CFD is a viable method to predict the pressure drop over packed beds, with an average error of about 10%.

Hassan (2008) simulated the flow between spherical particles with a rhombohedral packing (Fig. 2.2c). Hassan (2008) stated that most previous experimental studies were restricted to understanding the global parameters, and that local information of the flow velocity and patterns were scarce. However, his study showed that with the new developments in computational techniques, it is now possible to gain detailed insight into the flow between bed particles.

Bai et al. (2009) performed experiments and CFD simulations for both structured and random packings with up to 150 particles. Their predicted pressure drops matched well with the experimental measurements, with errors less than 10%. They also noticed a discrepancy between empirical correlations which predict the pressure drop at low aspect ratios, and their CFD predictions.

Reddy and Joshi (2010) described the deviations between the pressure drop predicted by the Ergun equation and experimental results at low aspect ratios, by simulating the flow through randomly packed beds with aspect ratios of $\alpha = 3$, 5 and 10 at $0.1 < Re_p < 10000$. Their CFD results showed an increase in pressure drop at low Reynolds numbers, and a decrease at high Reynolds numbers, thus giving evidence to the wall effect.

Eppinger et al. (2011) used STAR-CCM+® to investigate the flow patterns in randomly packed beds with aspect ratios of $3 \leq \alpha \leq 10$ in laminar, transition and turbulent regimes. They compared their CFD results for porosity and pressure drop with results from literature, and confirmed that physically correct results for flow characteristics in packed beds can be obtained using CFD. Theron (2011) performed a similar investigation and also found good agreement between his CFD results and that found in literature.

CFD investigations on the flow between packed bed particles have increased drastically in recent years due to the increase of computational power and the development of numerical techniques. Many authors have found good agreement between their own CFD predictions, experimental measurements and results from literature. However, some key issues with regards to modelling the flow through these complex geometries still exist, such as (1) mesh generation, (2) contact treatment and (3) turbulence solvers (Theron, 2011).

2.7.2 Meshing packed beds

Calis et al. (2001), Hassan (2008), Bai et al. (2009) and Reddy and Joshi (2010) generated meshes consisting of tetrahedral cells, due to the complexity of the geometry, where the mesh density is characterised by the edge length of a tetrahedral element. Calis et al. (2001) also added a number of prism layer cells to solve viscous effects in the boundary layer (Fig. 2.9). In each of these studies, the mesh density was determined in a mesh independence study. However, unstructured tetrahedral mesh generation in complex geometries such as fixed beds is a complex task because of triangulation (Reddy and Joshi, 2010).

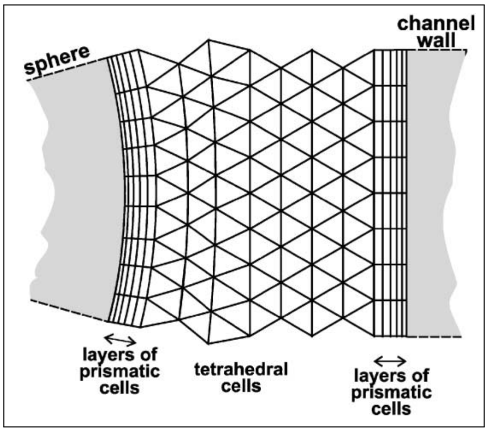

Figure 2.9: Schematic of the mesh between a particle and the cylinder wall, Calis et al. (2001).

Eppinger et al. (2011) and Preller (2011) used polyhedral and thin volume meshes respectively. Both investigated the influence of the number of prism layers used, and found that 2 prism layers offer the highest quality cells, without an excessive cell count.

Though the number of CFD investigations on the flow between packed bed particles have increased in recent years, the best practice for cell type and mesh density has not yet been established conclusively. However, with the ongoing expansion of meshing techniques, performing a mesh independence study is an integral part of any CFD investigation.

2.7.3 Contact treatment

A crucial point for the mesh generation in packed beds is the cell quality near the contact points between particles, and between particles and the cylinder wall. Due to its geometric nature, the contact points force the flow area around it to be very small, thin and acute. The cells near the contact points are usually either highly skewed or highly refined. High numbers of skewed cells lead to convergence problems during the calculation, whereas highly refined regions increase the number of cells and as a direct consequence the computational time (Eppinger et al., 2011). Several methods to overcome this problem has been presented in literature.

Calis et al. (2001), Reddy and Joshi (2008) and Reddy and Joshi (2010) eliminated contact points entirely by reducing their particle diameters by 1.0% without changing the particle positions, thus creating a gap between particles which improves the generated mesh. Bai et al. (2009) followed the same principle by reducing their particle diameter by 0.5%. Reddy and Joshi (2008) showed that the fluid velocity in the gap between the spheres is practically zero, and concluded that the gap does not affect the flow pattern. However, the particle shrinkage directly affects the packing porosity and therefore also the pressure drop. Since the pressure drop is known to be very sensitive to the bed porosity, these authors needed correction factors for porosity and pressure drop to be able to compare their CFD results with the predicted values from correlations.

Eppinger et al. (2011) introduced a method which flattens the particles locally at the contact points as soon as the minimum distance between two surfaces falls below an adequate and predefined value. This creates a gap between the particles which allows for a higher quality mesh. Since the method does not require changing the particle diameter, and the velocity within the gap is practically zero (Reddy and Joshi, 2008), it has a very small influence on the porosity and pressure drop. Their resulting geometry and mesh is shown in Fig. 2.10.

Lee et al. (2007) did an in depth investigation of the contact treatment between pebbles for CFD analysis, specifically the difference between pebbles in contact, and pebbles for which the contact point are approximated with gaps. They found that in the case of pebbles in contact, numerous differences in the flow fields and heat transfer could be found compared to the cases using gap approximations. With pebbles in contact, additional hot spots and large vortices were found near the contact area which were not observed in the gap approximations. They concluded that approximating the contact point between pebbles as gaps may give inaccurate information about the local flow fields and temperature distributions, despite the advantages these methods hold for mesh generation and calculation simplification.

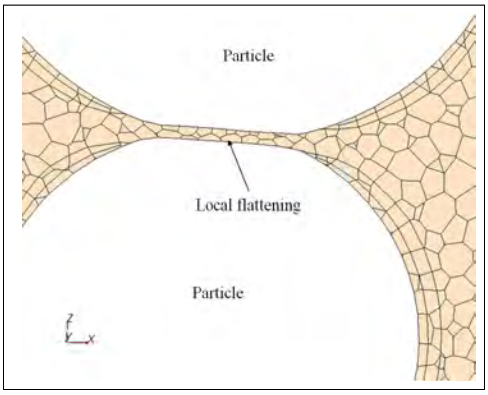

Figure 2.10: Artificial gap between two spheres, Eppinger et al. (2011).

Reyneke (2009) approximated the contact between particles by connecting particles at the contact point with a small cylindrical shape, thus removing the region near the contact point from the fluid domain. His results showed that the macroscopic flow properties, such as pressure drop, were not influenced by the cylinders. Reyneke (2009) did not investigate the method's influence on porosity or temperature distribution.

Dixon et al. (2013) did an in depth investigation of the influence of four different contact treatments on the flow through packed beds. They tested two global methods in which particles were either enlarged or shrunk uniformly, and two local methods in which particles were locally flattened, similar to Eppinger et al. (2011), and locally connected with bridges, similar to Reyneke (2009). Dixon et al. (2013) investigated the influence of the different methods on drag coefficients as well as heat transfer between particles. They found that global methods gave high errors in both drag coefficient and heat transfer rates between particles, unless the particle enlargements or shrinkages were very small, in which case the method does not solve the meshing problems. They found good results for drag coefficients for local methods. However, the method suggested by Eppinger et al. (2011), which creates small gaps between particles, presented unrealistic results for heat transfer between particles. Dixon et al. (2013) recommended a local bridging method with a suitably defined effective thermal conductivity for the bridge material.

Dixon et al. (2013) also noted that their recommendations were based solely on reducing effects of contact point modifications on the fluid flow and heat transfer between particles, and did not consider implementation. They also noted that their analysis does not replace the need for mesh independence studies or validation of simulations against experimental data.

2.7.4 Turbulence models

In any CFD calculation, the selection of an appropriate turbulence model is of great importance in order to obtain accurate predictions and capture the details of the flow parameters. Many methods exist to describe or solve turbulence effects, for which detailed descriptions can be found in Versteeg and Malalasekera (2007) or CD-Adapco (2012), however the three main approaches to modelling turbulence are:

1. Turbulence models for Reynolds-Average Navier-Stokes (RANS) equations.
   Prior to the application of the numerical methods the Navier-Stokes equations are time

averaged. Thus turbulence is modelled by focussing on the effects of turbulence on mean flow properties. The computational resources required for reasonably accurate solutions are modest. Common models used in the RANS approach are $k-\epsilon$ models, $k-\omega$ models and Reynolds Stress Models (RSM).

2. Large Eddy Simulation (LES).
   LES is an inherently transient technique which solves the behaviour of large 3D eddies, while the effects of small eddies on the flow are treated using sub-grid models. Explicitly solving large scales of turbulence provides more accurate solutions compared to RANS models, but also requires more computational resources.

3. Direct Numerical Simulation (DNS).
   DNS computes all turbulent velocity fluctuations, and provides extremely detailed and accurate solutions for turbulence. However, DNS demands extremely fine meshes and is even more computationally intensive than LES.

Calis et al. (2001) investigated the difference between the RSM and $k-\epsilon$ models, and found that the more computationally intensive RSM model yielded only slightly better pressure drop results. They considered the difference too small to justify the extra computational demand, and thus used the $k-\epsilon$ model.

Bai et al. (2009) examined different RANS turbulence models to understand their effects on the accuracy of the pressure drop prediction. They simulated the flow over a single packed bed, while varying only the turbulence model, and compared the CFD predictions with their own experimental results. Bai et al. (2009) found no significant difference among various $k-\epsilon$ and $k-\omega$ models, with variations of pressure drop less than 4.0%. The RSM model's predicted pressure drops were closest to the experimental measurements. However, it took 3 times longer to solve, while the $k-\epsilon$ model results were within 3.0% of the RSM model results. The extra computation effort required by the RSM model was not justified, thus they used the $k-\epsilon$ model.

Hassan (2008) used LES in his study of the flow within a segment of a pebble bed core, after weighing the advantages and disadvantages of RANS, LES and DNS. Hassan (2008) stated that LES is a compromise between DNS and RANS, as it is more accurate than RANS and less computationally intensive than DNS.

Preller (2011) did a comprehensive study to determine which turbulence models are appropriate for flows in packed beds by comparing various factors from the Realisable $k-\epsilon$, RSM and LES models. He found that the predicted pressure drops between these models varied less than 3.0% for a wide range of Reynolds numbers. He concluded then that more computationally intensive models, such as LES and RSM, offer little improvement in accuracy over the $k-\epsilon$ models.

2.7.5 Inlet boundary condition

For the sake of simplicity, Bai et al. (2009), Reddy and Joshi (2010) and Eppinger et al. (2011) all specified uniform velocity profiles at the inlet boundary. Fig. 2.11a shows such a profile, where $U(r)$ is the velocity profile as a function of the cylinder radius, and U_{avg} the average velocity. However, a constant velocity profile is an ideal case where the flow is considered to be inviscid.

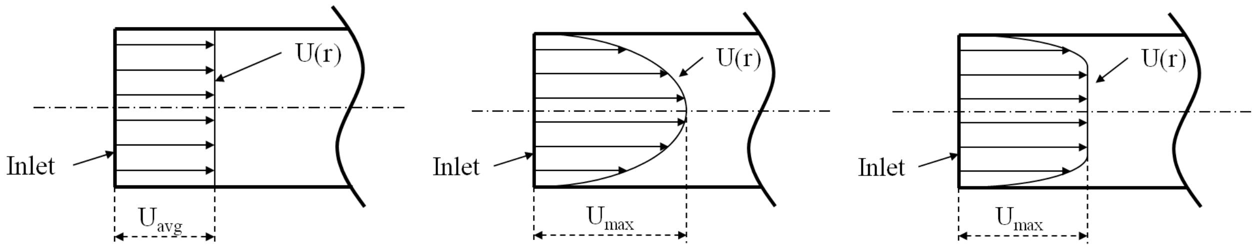

(a) Inviscid. **(b)** Laminar. **(c)** Turbulent.

Figure 2.11: Typical velocity profiles in a cylindrical pipe.

A more realistic representation of the flow entering the packed bed would be fully developed viscous flow. Figs. 2.11b and 2.11c show velocity profiles for fully developed laminar and turbulent flows respectively, where U_{max} is the maximum velocity. A simple method to determine a velocity profile for fully developed flow is to calculate $U(r)$, as derived from the shear stress in viscous flow. Eqns. (2.19) and (2.20) provide $U_L(r)$ and $U_T(r)$ for laminar and turbulent flows respectively (Munson et al., 2010), where R is the cylinder radius. The value of n' is a function of the pipe Reynolds number, see Munson et al. (2010, p. 407) for specific values.

$$U_L(r) = 2U_{avg}\left(1 - \left(\frac{r}{R}\right)^2\right) \tag{2.19}$$

$$U_T(r) = U_{avg}\left(\frac{(n'+1)(2n'+1)}{2(n')^2}\right)\left(1 - \frac{r}{R}\right)^{\frac{1}{n'}} \tag{2.20}$$

Another method to determine the velocity profile is explicitly solving for fully developed flow in a pipe using CFD, to generate a library of velocity values which can be introduced into the main computation at the inlet. This method is accurate due to its explicit nature, but requires additional computations to generate the velocity profiles (Tabor and Baba-Ahmadi, 2010).

2.7.6 Inlet and outlet regions

To minimise the influence of the boundary conditions at the inlet and outlet, Calis et al. (2001), Bai et al. (2009) and Reddy and Joshi (2010) extended their volume meshes roughly one cylinder diameter in the axial direction at the inlet and outlet. Eppinger et al. (2011) extended the volume mesh at the inlet by 3 particle diameters ($L_I = 3d$) and the outlet by 10 particle diameters ($L_O = 10d$).

Versteeg and Malalasekera (2007, p. 283) also suggest to place outlet boundaries much further downstream than 10 times the width of the last obstacle in the flow. This reduces the influence of the outlet boundary on the solution, since outlet boundaries can rarely handle reversed flow induced by recirculation. Fig. 2.12 shows a schematic of a packed bed domain with extended inlet and outlet regions.

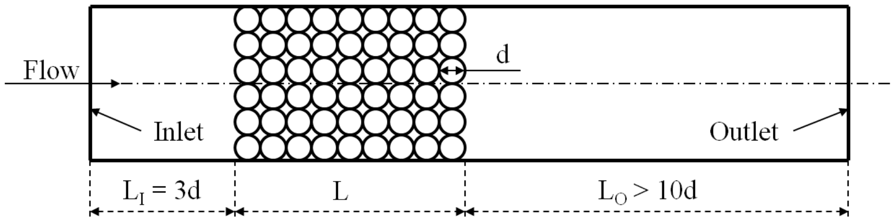

Figure 2.12: Schematic illustration of a packed bed domain with $L_I = 3d$ and $L_O > 10d$.

2.7.7 Pressure drop measurement

In order to measure the pressure drop from their CFD simulations, Reddy and Joshi (2010) and Eppinger et al. (2011) calculated the difference in pressure between the inlet and outlet boundaries. Keep in mind the respective lengths of the inlet and outlet regions used by each author, as described in Section 2.7.6. Bai et al. (2009) employed a similar method, and calculated the difference in pressure between $P_1 - P_2$, as shown in Fig. 2.13. These authors did not, however, indicate whether or not their measurements could be influenced by local pressure variations.

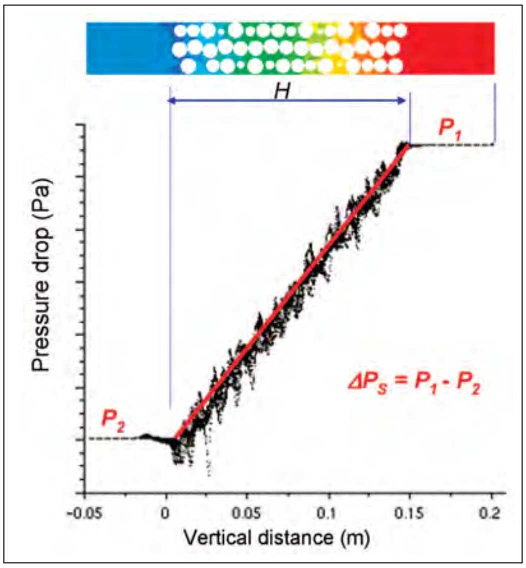

Figure 2.13: Profile of pressure as a function of the axial distance, Bai et al. (2009).

2.8 Summary

The goal of the survey was to gain insight and understanding of packed bed structures, methods to predict pressure drops and the discrepancies between theoretical and empirical studies. It was found that the parameters most commonly used to describe the structure of packed bed particles, are the aspect ratio and porosity. In infinite randomly packed beds the porosity can be considered uniform. However, particles in finite randomly packed beds form structured packings on the bed boundaries, which result in large variations in porosity in the near-boundary regions. This phenomenon is commonly known as the wall effect, and becomes increasingly prominent at low aspect ratios. Since the wall effect is related to the bed permeability, the flow distribution cannot be assumed to be uniform over the diameter of finite beds.

A number of semi-empirical correlations exist to describe the pressure drop through infinite beds. However, at small aspect ratios the wall effect presents numerous difficulties when attempting to predict the pressure drop, as it is dependent on both the aspect ratio and Reynolds number. Numerous authors have attempted to improve on these correlations to take the wall effect into account. As a result of these attempts, a large number of correlations exist. Only two of these correlations are relevant to this investigation, namely the Eisfeld & Schnitzlein and KTA correlations. The Eisfeld & Schnitzlein correlation does take the wall effect into account, whereas the KTA correlation does not.

It was found that previous investigations which simulated the flow through DEM generated beds explicitly, presented realistic results. However, the influence of some factors, such as the contact treatment and turbulence modelling, on the simulation of the fluid flow between particles are still uncertain. In Chapter 4, the influence of these factors are investigated, and a methodology is developed to set-up both DEM and CFD simulations using STAR-CCM+®. However, first a background of the theoretical principles of DEM and CFD as employed in STAR-CCM+®, are given in the next chapter.

Chapter 3

Modelling theory

Both Discrete Element Modelling and Computational Fluid Dynamics form an integral part of this investigation. In this chapter, the basic theoretical principles of DEM and CFD are described, as they are employed in STAR-CCM+®. Note that these principles are described only briefly, and more detailed information can be found in CD-Adapco (2012) and Versteeg and Malalasekera (2007).

3.1 Discrete Element Modelling

First introduced by Cundall and Strack (1979), Discrete Element Modelling (DEM) is an explicit numerical scheme which simulates the dynamic and static behaviour of assemblies of particles based on contact mechanics. It is usually assumed that particles displace independently, interact only at contact points and are rigid bodies. In STAR-CCM+®, DEM is an extension of Lagrangian modelling methodology which includes dense particle flows. The distinct characteristic is that inter-particle contact forces are included in the equations of motion. STAR-CCM+® uses a classical mechanics method to model DEM, which is based on a soft particle approach. The particles are allowed to develop a minute overlap that is proportional to the calculated contact force. The contact force is thus proportional to the overlap, particle material and geometric properties (CD-Adapco, 2012).

3.1.1 Momentum balance

The momentum balance for DEM particles is derived from the momentum balance of material particles, eq. (3.1). The DEM model introduces an extra body force representing inter-particle interactions due to contacts between particles and between particles and boundaries, eq. (3.2).

$$\begin{aligned} m_p \cdot \frac{dU_p}{dt} &= (\mathbf{F}_S) + (\mathbf{F}_B) && (3.1) \\ &= (\mathbf{F}_d + \mathbf{F}_{pg} + \mathbf{F}_{vm}) + (\mathbf{F}_g + \mathbf{F}_{ud} + \mathbf{F}_{sct}) && (3.2) \end{aligned}$$

In eq. (3.1), m_p is the mass of a particle, U_p is the velocity of that particle, and $\mathbf{F}_S$ and $\mathbf{F}_B$

represent the the forces acting on the surface of the particle and the body forces respectively. In eq. (3.2), $\mathbf{F}_d$ is the drag force, $\mathbf{F}_{pg}$ is the pressure gradient force, $\mathbf{F}_{vm}$ is a virtual mass force, $\mathbf{F}_g$ is the gravity force and $\mathbf{F}_{ud}$ is a user-defined body force. For detail on each of these forces see CD-Adapco (2012, p. 4343). $\mathbf{F}_{sct}$ is the sum of the contact forces acting on a particle:

$$\mathbf{F}_{sct} = \sum_{\text{Particles}}^{\text{Neighbour}} \mathbf{F}_{ct} + \sum_{\text{Boundaries}}^{\text{Neighbour}} \mathbf{F}_{ct} \tag{3.3}$$

where $\mathbf{F}_{ct}$ is the contact force by particle-particle or particle-boundary interactions. It should be noted that the exact formulation of contact forces is controlled by a user specified contact model. These contact models are described in the next section.

3.1.2 Contact force modelling

STAR-CCM+® provides the Hertz-Mindlin no-slip model for modelling the forces at contact points. The formulation of contact forces in STAR-CCM+® is a variant of the non-linear spring-dashpot model. The spring represents the forces which push particles apart, and the dashpot represents viscous damping and allows collision types other than perfectly elastic to be simulated. The forces between two particles are described as:

$$\mathbf{F}_{ct} = \mathbf{F}^n + \mathbf{F}^t \tag{3.4}$$

where $\mathbf{F}^n$ is the force component in the normal direction and $\mathbf{F}^t$ the force component in the tangential direction. The forces in the normal direction is defined as:

$$\mathbf{F}^n = -K^n d_o^n - J^n U_p^n \tag{3.5}$$

where K is the spring stiffness, d_o the particle overlap and J the damping coefficient. Similarly, the forces in the tangential direction is:

$$\mathbf{F}^t = \begin{cases} -K^t d_o^t - J^t U_p^t & \text{if} \quad |K^n d_o^n| C_{fs} > |K^t d_o^t| \\ K^n d_o^n C_{fs} d_o^t / |d_o^t| & \text{if} \quad |K^n d_o^n| C_{fs} \leq |K^t d_o^t| \end{cases} \tag{3.6}$$

where C_{fs} is a static friction coefficient. Note that K^n, K^t and J are all functions of an equivalent Young's modulus, equivalent shear modulus, equivalent particle diameter and equivalent particle mass. For particle-boundary collisions the Hertz-Mindlin model remains unchanged. However, the boundary diameter and mass are assumed to the infinite, which reduces the equivalent diameter and mass to only that of the particle. CD-Adapco (2012) states that the resulting code of the Hertz-Mindlin contact model is computationally efficient while still matching experimental data.

3.2 Computational Fluid Dynamics

Computational Fluid Dynamics (CFD) is the analysis of systems involving fluid flow, heat transfer and associated phenomena by means of computer based simulations (Versteeg and Malalasekera, 2007). In order to simulate these phenomena, the conservation laws of physics must be upheld (Versteeg and Malalasekera, 2007, p. 9):

1. The mass of a fluid is conserved.
2. The rate of change of momentum equals the sum of the forces on a fluid particle (Newton's second law).
3. The rate of change of energy is equal to the sum of the rate of heat addition to and the rate of work done on a fluid particle (first law of thermodynamics).

This section describes the equations which are based on these laws, and how they are discretized and applied to a finite number of control volumes.

3.2.1 Transport equations

The mechanics of physics continua are described by transport equations derived from the assumption that mass, momentum, energy and entropy are conserved in the continuum. The transport equation for a general variable ϕ can be written as:

$$\frac{\partial \rho\phi}{\partial t} + \nabla \cdot (\rho\phi\mathbf{u}) = \nabla \cdot (\Gamma \nabla \phi) + S_\phi \tag{3.7}$$

where $\mathbf{u}$ is the vector velocity field, Γ a the diffusion coefficient, ∇ the del operator and S_ϕ all the source terms for the property ϕ. In words, eq. (3.7) is:

Rate of change of ϕ. + Convective term. = Diffusion term. + Source terms.

By setting ϕ equal to 1, u, v, w and ν respectively, and selecting appropriate values for Γ and source terms, the system of equations which govern the time-dependent three-dimensional fluid flow and heat transfer of a compressible Newtonian fluid can be obtained:

$$\frac{\partial \rho}{\partial t} + \nabla \cdot (\rho\mathbf{u}) = 0 \tag{3.8}$$

$$\frac{\partial \rho u}{\partial t} + \nabla \cdot (\rho u\mathbf{u}) = -\frac{\partial p}{\partial x} + \nabla \cdot (\mu \nabla u) + S_x \tag{3.9}$$

$$\frac{\partial \rho v}{\partial t} + \nabla \cdot (\rho v\mathbf{u}) = -\frac{\partial p}{\partial y} + \nabla \cdot (\mu \nabla v) + S_y \tag{3.10}$$

$$\frac{\partial \rho w}{\partial t} + \nabla \cdot (\rho w\mathbf{u}) = -\frac{\partial p}{\partial z} + \nabla \cdot (\mu \nabla w) + S_z \tag{3.11}$$

$$\frac{\partial \rho \nu}{\partial t} + \nabla \cdot (\rho \nu \mathbf{u}) = -p \nabla \cdot \mathbf{u} + \nabla \cdot (\kappa \nabla T) + \Upsilon + S_\nu \tag{3.12}$$

$$p = p\,(\rho, T) \qquad ; \qquad \nu = \nu\,(\rho, T) \tag{3.13}$$

Eq. (3.8) is the continuity equation. Eqns. (3.9), (3.10) and (3.11), also known as the Navier-Stokes equations, are the momentum equations in the x, y and z directions respectively and u, v and w the components of $\mathbf{u}$. Eq. (3.12) is the energy equation with ν the specific internal energy, κ the conduction heat transfer coefficient and Υ a dissipation function. Eq. (3.13) represents the equations of state which relate other variables to the two state variables, ρ and T, where T is the fluid temperature. Eqns. (3.8) to (3.13) are the governing equations of the conservation laws of physics for fluid flow.

3.2.2 Finite volume method

In order to apply the governing equations of the conservation laws of physics to a solution domain, the domain is discredized into a finite number of non-overlapping control volumes. These control volumes correspond to the cells of a computational grid. The gaol is to obtain a set of algebraic equations, which can be solved using an algebraic multi-grid solver. First, eq. (3.7) is integrated over one of these control volumes, labelled λ:

$$\int_V \frac{\partial \rho \phi}{\partial t}\, \mathrm{d}V + \int_V \nabla \cdot (\rho \phi \mathbf{u})\, \mathrm{d}V = \int_V \nabla \cdot (\Gamma \nabla \phi)\, \mathrm{d}V + \int_V S_\phi\, \mathrm{d}V \tag{3.14}$$

where V is the volume of the control volume λ. When considering a steady state calculation, the first term equates to zero. Applying Gauss's divergence theorem to the convection and diffusion terms give:

$$\int_{\partial V} (\rho \phi \mathbf{u}) \cdot \mathrm{d}\mathbf{S} = \int_{\partial V} (\Gamma \nabla \phi) \cdot \mathrm{d}\mathbf{S} + \int_V S_\phi\, \mathrm{d}V \tag{3.15}$$

where ∂V is the control volume boundary and $\mathrm{d}\mathbf{S}$ an outward pointing surface vector on said boundary. The control volume consists of ϑ flat faces, thus the surface integral can be decomposed as the sum of the integrals over the different faces that surrounds the control volume:

$$\sum_{\varphi=1}^{\vartheta} \int_\varphi (\rho \phi \mathbf{u}) \cdot \mathrm{d}\mathbf{S} = \sum_{\varphi=1}^{\vartheta} \int_\varphi (\Gamma \nabla \phi) \cdot \mathrm{d}\mathbf{S} + \int_V S_\phi\, \mathrm{d}V \tag{3.16}$$

where φ is the control volume face number. For continuous functions under the integrals, the midpoint integration rule can now be applied to the integrals:

$$\sum_{\varphi=1}^{\vartheta} (\rho \phi \mathbf{u})_\varphi \cdot \mathbf{A}_\varphi = \sum_{\varphi=1}^{\vartheta} (\Gamma \nabla \phi)_\varphi \cdot \mathbf{A}_\varphi + (S_\phi V)_\lambda \tag{3.17}$$

where $\mathbf{A}$ is the outward pointing face area vector. The face number and the centre of the faces are labelled with the subscript φ. For continuous flow properties the values of the individual properties can be interpolated to the faces:

$$\sum_{\varphi=1}^{\vartheta} \rho_\varphi \phi_\varphi \mathbf{u}_\varphi \cdot \mathbf{A}_\varphi = \sum_{\varphi=1}^{\vartheta} \Gamma_\varphi \left(\nabla \phi\right)_\varphi \cdot \mathbf{A}_\varphi + \left(S_\phi V\right)_\lambda \tag{3.18}$$

Eq. (3.18) is the discrete form of eq. (3.7) for a steady state calculation as employed in STAR-CCM+®.

3.2.3 Turbulence

Many flows of engineering significance are turbulent, however the random nature of turbulent flow presents a challenge when attempting to simulate the turbulent regime. This section gives a brief introduction to the modelling of turbulence as employed in STAR-CCM+®.

RANS turbulence models

To obtain the Reynolds-Average Navier-Stokes (RANS) equations, the Navier-Stokes equations, eqns. (3.9) to (3.11), are time averaged and decomposed into a mean value and a fluctuating component. The resulting equations for the mean values are essentially identical to the original equations, however an additional term appears on the right hand side of the momentum transport equations. This additional term is known as the Reynolds stress tensor, and represents the fluctuating component. Written in the form of eq. (3.7), the RANS equations are:

$$\frac{\partial \bar{\rho} \Phi}{\partial t} + \nabla \cdot \left(\bar{\rho} \Phi \mathbf{U}\right) = \nabla \cdot \left(\Gamma \nabla \Phi\right) + \mathbf{T} + S_\Phi \tag{3.19}$$

$$\mathbf{u} = \mathbf{U} + \mathbf{u}' \qquad ; \qquad \Phi = \frac{1}{\Delta t} \cdot \int_0^{\Delta t} \phi(t)\,\mathrm{d}t \tag{3.20}$$

where $\mathbf{U}$ and $\mathbf{u}'$ are the mean and fluctuating components of $\mathbf{u}$ respectively, Φ the time average of the property ϕ, t the time, and the over-bar indicates time averaged. The Reynolds stress tensor, $\mathbf{T}$, is:

$$\mathbf{T} = -\frac{\partial(\overline{\rho u' \phi'})}{\partial x} - \frac{\partial(\overline{\rho v' \phi'})}{\partial y} - \frac{\partial(\overline{\rho w' \phi'})}{\partial z} \tag{3.21}$$

where ϕ' is the fluctuating component of ϕ. The challenge is thus to model the Reynolds stress tensor in terms of mean flow quantities. One of the most widely used methods is to use the turbulent viscosity, μ^τ, to model $\mathbf{T}$. These models are known as eddy-viscosity models. Presently, the $k-\epsilon$ models are the most widely used and validated of all eddy-viscosity models (Versteeg and Malalasekera, 2007, p. 67). Many variations of the model exist, however the common principle between all $k-\epsilon$ models is that a velocity scale/intensity, γ, and length scale, ℓ, are defined which represent the large scale turbulence:

$$\gamma = \gamma\left(k\right) \qquad ; \qquad \ell = \ell\left(k, \epsilon\right) \tag{3.22}$$

where k is the turbulent kinetic energy and ϵ the turbulent dissipation rate. The turbulent viscosity used to model $\mathbf{T}$ is then:

$$\mu^{\tau} = \mu^{\tau}\left(\rho k \epsilon\right) \qquad ; \qquad \mathbf{T} = \mathbf{T}\left(\mu^{\tau} \rho k\right) \tag{3.23}$$

In STAR-CCM+® the eddy-viscosity models also solve additional transport equations for quantities such as k and ϵ to derive μ^{τ}.

Large Eddy Simulation

LES is an inherently transient technique which solves the behaviour of large 3D eddies, while the effects of small eddies on the flow are treated using sub-grid models. The equations solved for LES are obtained through a filtering process of the unsteady Navier-Stokes equations. The filtered equations look similar to the unsteady RANS equations, however $\mathbf{T}$ now represents the sub-grid scale stresses. This tensor is modelled using the Boussinesq approximation:

$$\mathbf{T} = 2\mu^{\tau}\mathbf{S} - \frac{2}{3}\left(\mu^{\tau}\nabla \cdot \mathbf{u} + \rho k\right)\delta \tag{3.24}$$

where $\mathbf{S}$ is a strain rate tensor and δ a function similar to the Kronecker delta.

Note that one of the difficulties with LES is defining appropriate turbulent conditions at inlet boundaries. STAR-CCM+® uses a Synthetic Eddy Method (SEM) to automatically provide turbulent eddies across inlet boundaries.

3.2.4 Mesh generation

Generating a proper mesh is an integral part of any CFD simulation, since the quality and density of the mesh have a great impact on the stability and accuracy of the solution. STAR-CCM+® contains tools which can be used to generate a volume mesh, starting from a surface. The volume mesh is the mathematical description of the domain of the problem being solved. It is in turn constructed of the following:

1. Vertices.
   A vertex is a point in space defined by a position vector.
2. Faces.
   A face consists of an ordered collection of vertices, such that they define a 3D surface. Faces may have any number of vertices.
3. Cells.
   A cell is an ordered collection of faces, which define a closed volume. These cells are the control volumes to which the transport equations, eq. (3.18), are applied. Cells may have any number of faces, as long as it contains enough faces to create a closed volume.

Cells of arbitrary polyhedral shape are also permitted, which allows for the generation of unstructured meshes.

The mesh parameters, such as meshing models and cell sizes, are contained within mesh continua. STAR-CCM+® allows many meshing parameters to be set, and many are specific to certain meshing models, however the most basic parameters are:

1. Base size, B.
   The base size value is a characteristic dimension of the geometry of the problem being solved. Usually, all other properties are set relative to the base size.
2. Surface size.
   The surface size allows values to be set which determine the resultant size of the cells next to the surfaces of the domain. It is usually set with a target and minimum size, where the target value is the desired edge cell length on the surface, and the minimum value controls the lower limit of the edge cell length.
3. Surface growth rate.
   The surface growth rate controls the rate at which the lengths of cell edges can vary from one cell to its neighbour. This parameter is useful when local refinement of the volume mesh is required.

Rough meshes often lead to unstable and inaccurate solutions, while dense meshes demand more computational resources. In any CFD simulation, a compromise must be made between the accuracy of the results and the time and effort needed for an accurate solution. CD-Adapco (2012, p. 1902) also notes that it is likely that several iterations might be required to obtain appropriate mesh parameters for a simulation.

3.3 Summary

In this chapter, the basic theoretical principles of DEM and CFD were described, as they are employed in STAR-CCM+®. The momentum balance for DEM particles was given, and the modelling of contact forces between particles was described. The analytical form of the transport equations necessary to simulate fluid flow within a control volume was shown. The discrete form of these equations, as applied to a finite number of control volumes or cells, was derived. The basic principles of turbulence modelling and mesh generation were also described. In the next chapter a methodology is developed to simulate the flow through DEM generated beds explicitly using STAR-CCM+®. These simulations employ the principles described in this chapter.

Chapter 4

Methodology

This chapter describes the steps taken during the numerical analyses of the flow through packed beds, to ensure accurate solutions with a reasonable degree of confidence. The commercial CFD package STAR-CCM+® was used for all analyses, as Preller (2011) and Theron (2011) proved that STAR-CCM+® is an appropriate platform to generate packed beds using DEM, and performing CFD analysis of the flow through packed beds.

4.1 DEM simulation setup

This section contains detail on the DEM simulation setup which was used to generate all the beds needed for the CFD simulations of the flow through the beds. The default values for the relevant parameters in STAR-CCM+® version 7.06 were used, unless stated otherwise.

4.1.1 Geometry and boundaries

Simple cylindrical domains were created using SolidWorks, which were imported into STAR-CCM+® as surface meshes. These domains had diameters equal to the cylinder diameters of the final beds, D, and axial lengths of L_{DEM}. See Section 4.1.2 for more detail on L_{DEM}. The cylinder- and particle surfaces were set as wall boundaries, with no slip.

4.1.2 Particle injection

To accommodate particle generation, L_{DEM} was made 20% larger than the expected length of the final bed, L. Thus, $L_{DEM} = 1.2d\,(L/d)$, where $L/d = 10$. The L/d relation is described in more detail in Section 4.8. Particles were generated at the top of the domain using a point injector, and simulated to fall in the z-direction with a gravitational acceleration of -9.81 m/s^2. The point injector was set on the cylinder centreline, one particle diameter from the top surface of the cylinder. Particles were generated at a rate of one particle per second.

4.1.3 Mesh continua

CD-Adapco (2012) states that the best practice for DEM is to use a coarser mesh than typical CFD applications, and Theron (2011) used mesh base sizes of roughly a quarter of the particle diameters. Thus, mesh base sizes of $B = d/4$ were used. The meshing models used for the mesh generation were:

- Surface remesher.
- Polyhedral volume mesher.

The relatively rough meshes created a curvature deviation on the cylinder surfaces (Fig. 4.1), which could influence the final positions of the particles. This curvature deviation was reduced by increasing the number of points per circle from the default value, 32, to 72.

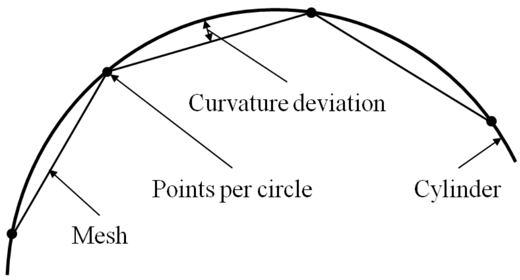

Figure 4.1: Schematic of curvature deviation in the DEM domain due to rough meshing.

4.1.4 Physics continua

As per the best practices proposed by CD-Adapco (2012), and the methodology developed by Theron (2011), the physics models used for all DEM simulations were:

- Implicit unsteady.
- Coupled implicit solver.
- Ideal gas: Air.
- Laminar.
- Gravity.
- Lagrangian multiphase.
  - DEM particles.
  - Solid.
  - Constant density.
  - Spherical particles.
- Multiphase interaction.
  - Particle-particle interactions.
  - Particle-cylinder interactions.
  - Hertz-Mindlin no slip contact model.

DEM simulations are inherently transient, thus the implicit unsteady model was selected. An implicit unsteady time step of 0.05 s and a DEM time scale of 0.05 s was set within the implicit unsteady model. Since it was not necessary to take any fluid flow effects into account, the coupled implicit solver was frozen. This means that the coupled implicit solver, the working fluid and the regime did not have any influence on the DEM results. These models were only selected because STAR-CCM+® requires a selection. The gravity model added the body force induced by gravity. The Lagrangian multiphase model is used to define the solid particles in the simulation. The physical properties of the particles are defined in this model. The multiphase interaction model is used to define how the particles behave when they collide with one another and the region walls. For detail on the Hertz-Mindlin contact model see Section 3.1.2.

4.1.5 Material

The material used for both the cylinder boundaries and the particles were Poly(methyl methacrylate) (PMMA). The material properties of PMMA, shown in Tab. 4.1, are similar to the that of the materials used in the experiments by Rosslee (2009) and Hassan and Kang (2012).

Table 4.1: Material properties of Poly(methyl methacrylate) (PMMA).

Property	Value	Unit
Density	1190.00	[kg/m^3]
Young's modulus	2500.00	[MPa]
Poisson coefficient	0.37	[-]
Static friction coefficient	0.30	[-]

4.1.6 Stopping criteria

Keeping in mind that particles were generated at a rate of one particle per second, the maximum physical time was specified as the number of expected particles to be generated, plus three seconds. Thus, in these last three seconds no new particles were generated and the bed was allowed to settle via gravity. This means that the DEM generated beds had loose packings, since no vibration of the container was simulated after the particles settled. Through inspection of the simulation results it was found that the particles settled roughly one second after the last particle was injected. However, in order to ensure that the velocities of the particles were practically zero, an additional three seconds were added after the last particle was injected. The particles were taken to be settled when the magnitudes of their velocities were $U_p < 1 \times 10^{-4}$ m/s. Fig. 4.2 shows examples of finished DEM simulations for beds with aspect ratios of $\alpha =$ 3.00 and 6.33. The colour bars show that the magnitudes of the velocities of the particles were $U_p < 5.2 \times 10^{-8}$ m/s and $U_p < 2.1 \times 10^{-8}$ m/s for $\alpha = 3.00$ and 6.33 respectively.

(a) $\alpha = 3.00$. **(b)** $\alpha = 6.33$.

Figure 4.2: Examples of finished DEM simulations with particle velocities practically zero.

4.2 CFD simulation setup

This section contains detail on the CFD simulation setup which was used to simulate the flow through the beds. The default values for the relevant parameters in STAR-CCM+® version 7.06 were used, unless stated otherwise.

4.2.1 Geometry

Domains for the CFD simulations of the flow through the beds were created using SolidWorks, by importing the centre coordinates of the particles obtained from the DEM simulations. This step was necessary since the version of STAR-CCM+® used for this investigation was not yet capable of converting DEM particles to solid bodies. The version used also did not provide the tools needed for contact treatment, whereas SolidWorks did. Figs. 4.3a and 4.3b show two examples of these domains as created in SolidWorks, for beds with aspect ratios of $\alpha = 3.00$ and $\alpha = 6.33$ respectively.

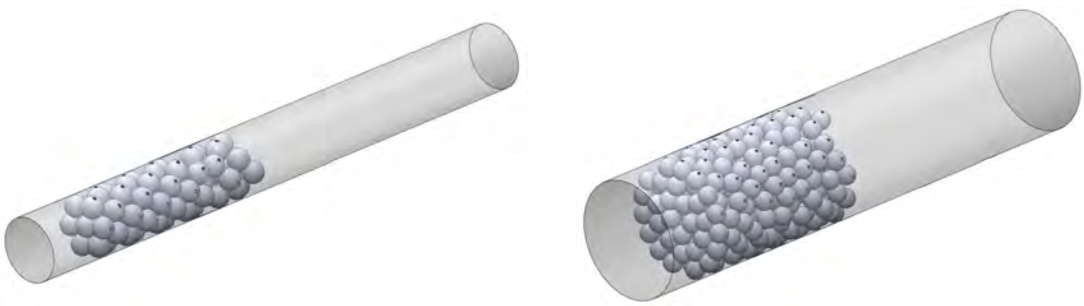

(a) $\alpha = 3.00$. **(b)** $\alpha = 6.33$.

Figure 4.3: Examples of domains used for CFD simulations created in SolidWorks.

The domains were created with inlet and outlet regions as described in Section 2.7.6, with the inlet region extending a length of $L_I = 3d$ from the bed and the outlet region extending a length of $L_O = 10d$ from the bed, as shown in Fig. 4.4. The contact treatment was also applied using eq. (4.1). These domains created in SolidWorks were then imported into STAR-CCM+® as surface meshes.

4.2.2 Boundaries

The domains imported into STAR-CCM+® were split into four different regions, with boundary conditions as given in Tab. 4.2. As an example, Fig. 4.4 shows where the regions were specified for a bed with $\alpha = 6.33$.

Table 4.2: Regions and boundaries used for CFD simulations.

Region	Boundary condition
Inlet	Velocity inlet
Outlet	Pressure outlet
Cylinder	Wall with no slip
Particles	Wall with no slip

Velocity profiles for fully developed laminar and turbulent flows were specified at the inlet boundaries as a function of the radial coordinate, as described in Section 4.7. Also note that the assumption was made that the control volume was adiabatic, thus no heat transfer over the boundaries were modelled. An ambient temperature of $T_a = 300$ K and ambient pressure of $p_a = 101.325$ kPa were used for all simulations.

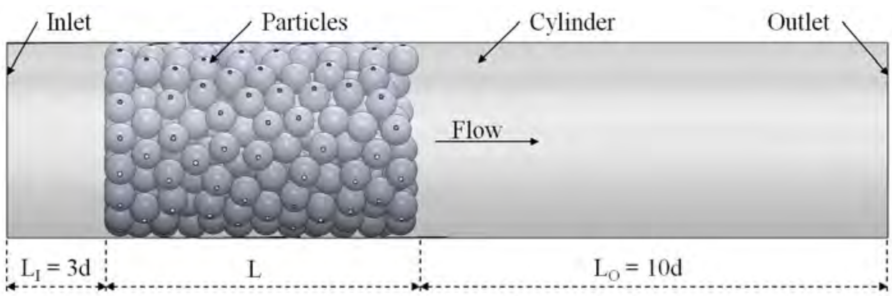

Figure 4.4: Illustration of the regions specified for the CFD simulations, for a bed with $\alpha = 6.33$.

4.2.3 Mesh continua

Following the results of Section 4.5, the mesh independence study, the following meshing models were used for all CFD simulations:

- Surface remesher.
- Polyhedral volume mesher.
- Prism layer mesher.

Tab. 4.3 shows the relative values of the most important parameters used for the mesh generation. For more information on the mesh parameters see Section 3.2.4.

Table 4.3: Parameter values for mesh generation of CFD simulations.

Parameter	Value
Base size, B	Eq. (4.2)
Surface size, minimum	$0.25B$
Surface size, target	$1.00B$
Number of prism layers	2
Prism layer thickness	$0.20B$

4.2.4 Physics continua

As per the results of Section 4.6, the investigation of the influence of different turbulence models, and the best practices suggested by CD-Adapco (2012), the physics models used for all CFD simulations were:

- Steady.
- Coupled implicit solver.
- Ideal gas: Air.
- Turbulent.
  - Realisable $k - \epsilon$ turbulence model.
  - Two-layer all y^+ wall treatment.

4.2.5 Solvers and stopping criteria

Due to the complex nature of the flow of the compressible fluid between the particles, the coupled implicit solver's Courant number was given a value 1.0. In order to decrease convergence time, the Continuity Convergence Accelerator (CCA) was also enabled, with an under relaxation factor of 0.01. Simulations were accepted as converged and complete when all residual values were smaller than 10^{-3}, and a steady state solution was achieved.

4.3 Reference bed

Development of the methodology was done on a single packed bed which was generated using DEM. This reference bed contained $N = 10$ particles and had an aspect ratio of $\alpha = 2.01$. Fig. 4.5 shows a schematic of the bed, and Tab. 4.4 shows the basic parameters of the reference bed geometry. The aspect ratio and number of particles of the reference bed was relatively small in order to save on computational time.

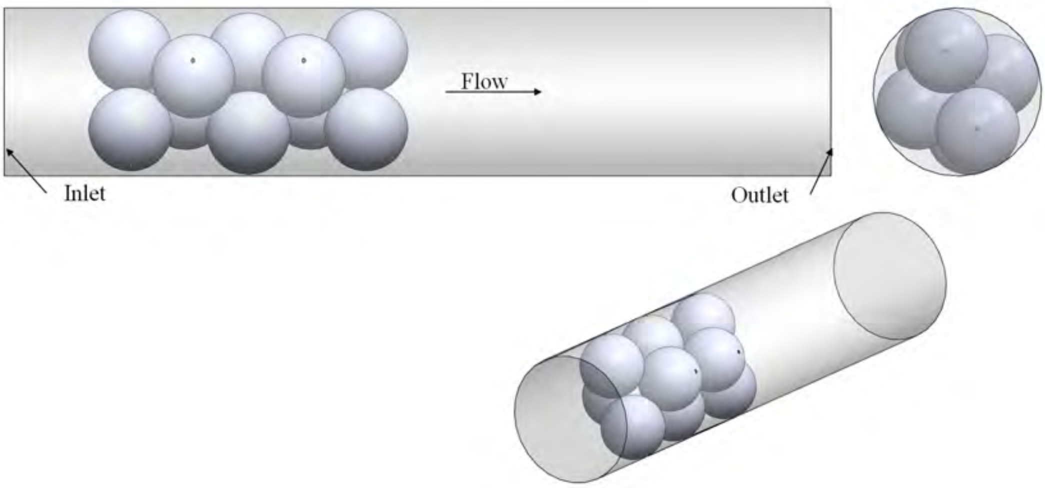

Figure 4.5: Reference bed used for the development of the methodology, see Tab. 4.4 for parameter values.

Table 4.4: Reference bed geometric information.

Parameter	Value	Unit
α	2.01	[-]
D	100.00	[mm]
d	49.80	[mm]
N	10	[-]
L_I	50.00	[mm]
L_O	250.00	[mm]

4.4 Working fluid

Considering the goal of the investigation, the particular fluid used was not of great importance. However, it was important to use the same fluid properties in the CFD simulations, as was used to calculate the pressure drops using semi-empirical correlations. For validation purposes, simulating either compressible or incompressible flow would have been appropriate, since the most common working fluids used in experiments from literature were water and air. It was decided to use air as a compressible ideal gas for all CFD simulations, with the goal of developing the methodology needed to simulate compressible flow in packed beds.

4.5 Mesh independence study

Generating a proper mesh is an integral part of any CFD simulation, since the quality and density of the mesh have a great impact on the stability and accuracy of the solution. Low resolution meshes often lead to unstable and inaccurate solutions, while dense meshes demand more computational resources. A compromise had to be made between the accuracy of the results and the time and effort needed for an accurate solution.

The main goal of the mesh independence study (MIS) was to determine the mesh requirements in terms of mesh type, contact treatment and mesh density needed to obtain a mesh independent solution. As a starting point, the flow through the reference bed (Fig. 4.5) was simulated with air as an ideal gas, with the Realisable $k - \epsilon$ turbulence model, and with the inlet boundary specified as a uniform velocity profile as shown in Fig. 2.11a.

4.5.1 Parameters used for mesh quality analysis

The following three parameters were chosen to evaluate the quality of the mesh generated in the reference bed domain:

1. Mesh density influences the overall mesh quality on a global scale. The mesh needed to be sufficiently dense to adequately capture the flow characteristics. The effects of the mesh density on the solution was investigated and is described in Section 4.5.4.

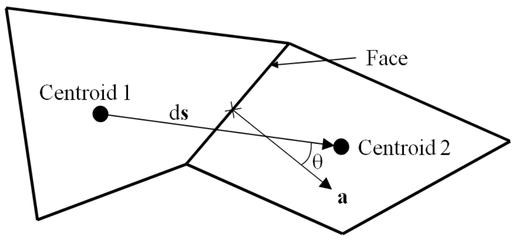

Figure 4.6: Illustration of two adjacent cells connected with a skewness angle θ.

2. The cell skewness angle, θ, is the angle between the area vector of the surface connecting two cells, **a**, and the vector connecting the two cell centroids, d**s**, as shown in Fig. 4.6. To avoid any impact on the simulation robustness, the mesh should not have cells with skewness angles of $\theta > 85°$ (CD-Adapco, 2012).

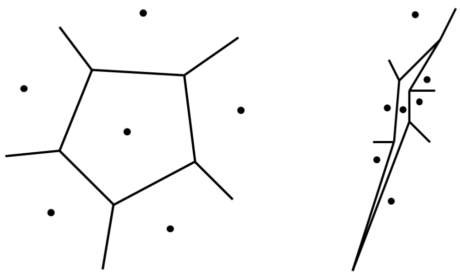

(a) Good cell. **(b)** Degenerate cell.

Figure 4.7: Schematic illustration of cells with qualities of (a) $\zeta \to 1$ (b) $\zeta \to 0$.

3. The cell quality metric, $0 < \zeta < 1$, is a function of the relative geometric distribution of cell centroids of the face-neighbour cells and the orientation of the cell faces. Cells with qualities approaching 1 are considered perfect cells (Fig. 4.7a), while degenerate cells have qualities approaching zero (Fig. 4.7b).

4.5.2 Meshing model and contact treatment

Following the discussion in Section 2.7.3, it was decided to use a similar approach as Reyneke (2009) for contact treatment. Particles were connected to each other without changing the particle diameter. This was achieved by creating a fillet, with a specified radius f, on all intersection points between particle-particle and particle-cylinder surfaces, as shown in Fig. 4.8.

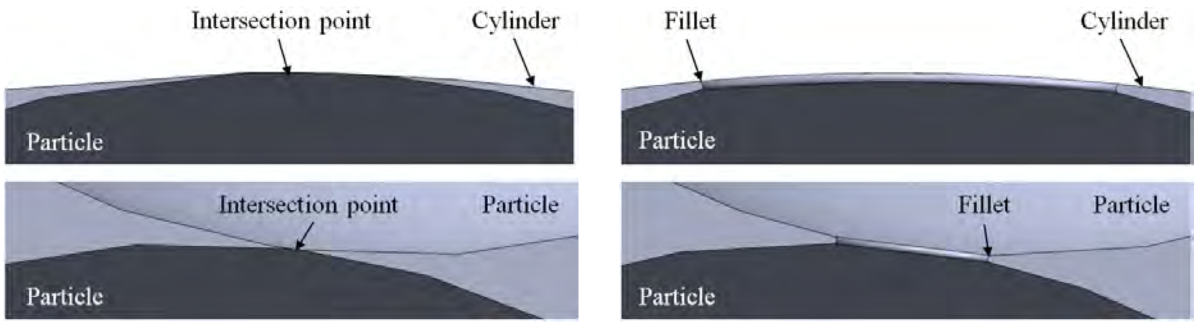

(a) No fillet at contact point. **(b)** Fillet at contact point.

Figure 4.8: Examples of contact points between particle-particle and particle-cylinder surfaces, with and without contact treatment.

Tab. 4.5 shows the five meshing cases which were analysed, and Fig. 4.9 shows the mesh structure at a contact point between two particles for each case. In cases 2 and 5, 2 prism layers were used, as Preller (2011) found that 2 prism layers offer the highest quality cells, without an excessive cell count. The mesh base size was specified as $B = 3$ mm for all 5 cases, and a radius of $f = 0.1$ mm was used for the fillets at the contact points for cases 4 and 5.

Table 4.5: Mesh quality results for selected meshing models and contact treatment.

Case	Meshing model	Prism layers	Contact treatment	Cells ($\times 10^6$)	Skewed cells ($\theta > 85°$)	Degenerate cells ($\zeta < 0.05$)
1	Polyhedral	-	No	0.996	2922	2975
2	Polyhedral	2	No	1.302	3009	3799
3	Thin	-	No	1.030	427	808
4	Polyhedral	-	Yes	1.138	267	300
5	Polyhedral	2	Yes	1.455	261	218

STAR-CCM+® re-meshed the surfaces of the geometry as the first step in the meshing process, to ensure that a high quality volume mesh could be created from it (CD-Adapco, 2012). However, during surface re-meshing STAR-CCM+® created extremely thin flow regions at the contact points of cases 1, 2 and 3, which did not have any contact treatment. High numbers of skewed- and degenerate cells were generated in these extremely thin regions. These re-meshed surfaces also created gaps between particles which would negatively influence the simulation of heat transfer between particles. From Tab. 4.5 it can be seen that case 5 had the least number of skewed cells with $\theta > 85°$, as well as the least number of low quality cells with $\zeta < 0.05$. The use of 2 prism layers increased the cell count, however according to CD-Adapco (2012), prism layers greatly enhance the accuracy of the simulation as they are necessary to simulate boundary layers.

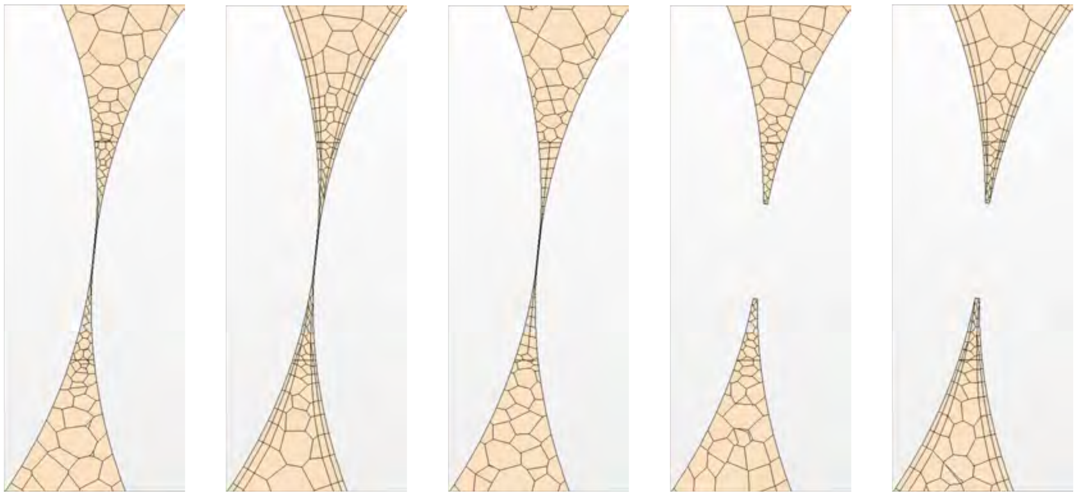

(a) Case 1. **(b)** Case 2. **(c)** Case 3. **(d)** Case 4. **(e)** Case 5.

Figure 4.9: Mesh structure at a contact point between two particles, as per Tab. 4.5.

With these results, as well as the recommendations of Dixon et al. (2013) in Section 2.7.3, case 5 was chosen as the primary meshing method, with a polyhedral meshing model, 2 prism layers and fillets created at the contact points.

4.5.3 Contact area

Fig. 4.10 shows schematically that specifying a fillet, with a radius f, at the contact point between two particles also inherently specifies the size of the diameter of the contact area, D_C, and the contact area itself, C.

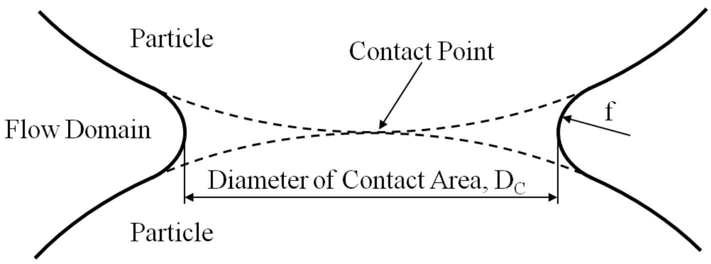

Figure 4.10: Schematic illustration of a contact point between two particles with a filler radius f.

Though the influence of the contact area on the heat transfer between particles was not analysed in this investigation, it will be an important factor for future studies considering the temperature distributions within packed beds. The influence of the size of the contact point fillet on the pressure drop was investigated. The flow through the reference bed was simulated with five different values for f, as shown in Fig. 4.11. The mesh base size was specified as $B = 2$ mm for all five cases, which resulted in roughly 1.359×10^6 cells. Tab. 4.6 shows the five different values used for f, as well as their corresponding contact diameters, D_C, and contact areas, C.

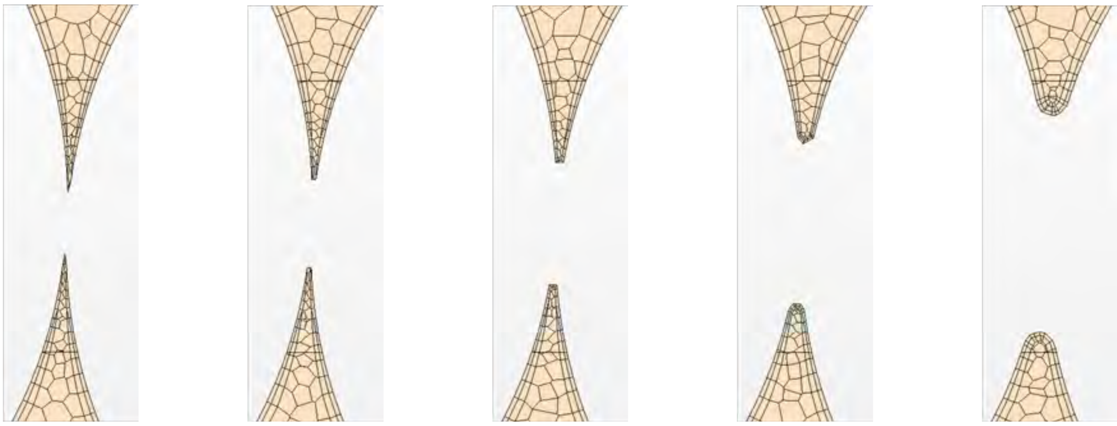

(a) $f = 0.05$ mm. **(b)** $f = 0.1$ mm. **(c)** $f = 0.2$ mm. **(d)** $f = 0.4$ mm. **(e)** $f = 0.8$ mm.

Figure 4.11: Mesh structure at a contact point between two particles for different values of f.

Table 4.6: Corresponding values between f, D_C, and C.

f	[mm]	0.05	0.10	0.20	0.40	0.80
D_C	[mm]	3.21	4.38	6.00	8.22	11.16
C	[mm^2]	8.09	15.07	28.27	53.07	97.82

Fig. 4.12a shows that the pressure drop increased for $f > 0.1$ mm, due to the increased flow restriction, and increased for $f < 0.1$ mm, due to low cell quality in the contact region. Thus, fillets with $f = 0.1$ mm had the smallest influence on the fluid flow, while still limiting the number of low quality cells. A fillet radius of $f = 0.1$ mm was chosen for the reference bed, however in order to scale the fillet radius to beds with different aspect ratios, f was calculated as a percentage of the particle diameter:

$$f = \frac{0.2d}{100} \tag{4.1}$$

4.5.4 Mesh density

The influence of the mesh density on the simulation was analysed by simulating the flow through the reference bed, while decreasing the mesh base size, B, and consequently increasing the cell count and mesh density. Fig. 4.12b shows that the pressure drop over the bed was mesh independent above roughly 1.2×10^6 cells, since the pressure drop $\Delta p\,(B = 2)$ was within 1.0% of $\Delta p\,(B = 1.4)$. In order to have a mesh independent solution without an excessive cell count, a mesh density which corresponded to $1.7 \leq B \leq 2$ mm was chosen for the reference bed. Fig. 4.13 shows the structure of the mesh in the reference bed, with $B = 2$ mm. In order to scale the mesh base size to beds with different aspect ratios, B was calculated as a percentage of the particle diameter:

$$B = \frac{4d}{100} \tag{4.2}$$

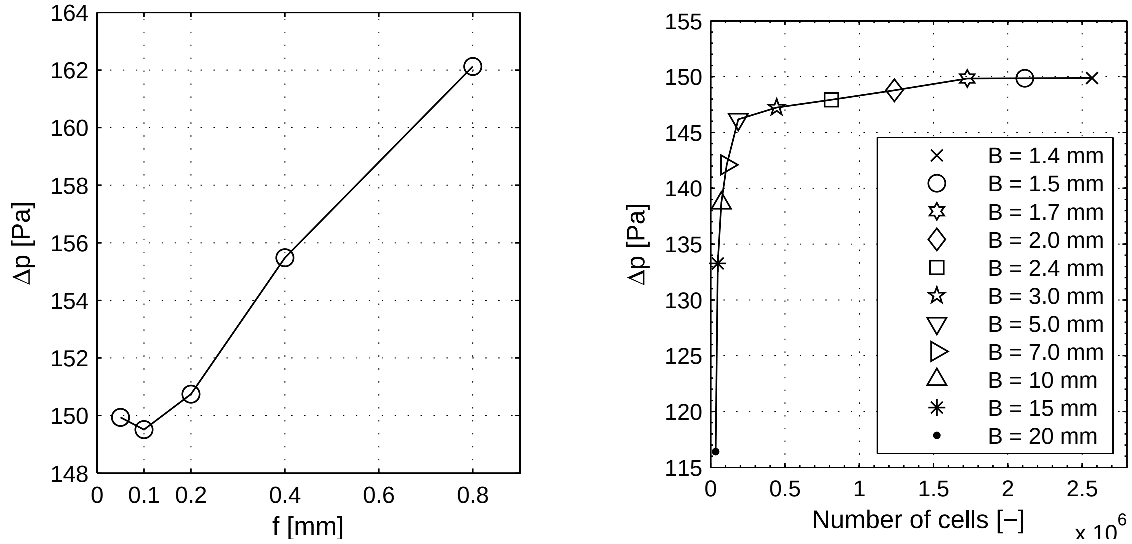

(a) Δp vs. f.

(b) Δp vs. number of cells.

Figure 4.12: Pressure drop over the reference bed, at $Re_p = 10^4$, as a function of (a) the contact point fillet radius and (b) the mesh density.

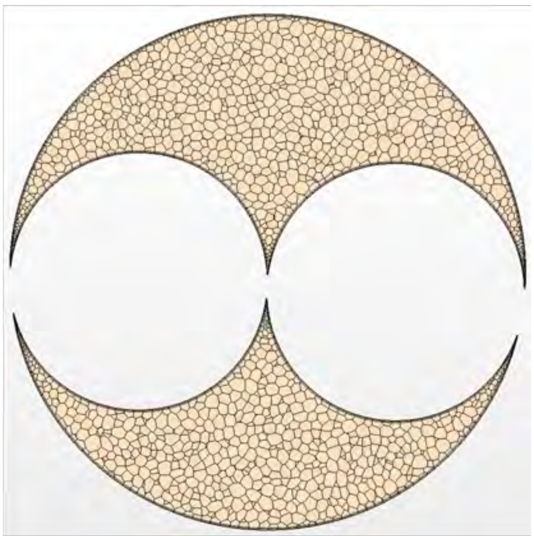

Figure 4.13: Mesh structure in the reference bed, with $B = 2$ mm.

4.5.5 Wall treatment and y^+ values

Near the wall boundaries the flow is influenced by viscous effects. These effects can either be modelled by using a wall function, or resolved if the mesh is fine enough. It is standard practice to express the near wall mesh resolution in the form of the dimensionless wall distance, y^+. CD-Adapco (2012) states that significant errors could occur if the near wall mesh resolution is not consistent with the modelling assumptions, and suggests typical y^+ values for different applications and wall functions. These guidelines are as follows for different wall treatments:

1. High y^+ wall treatment.
   The viscous effects near the wall boundaries are modelled and a rough mesh can be used with $15 < y^+ < 500$. However, this model is not suitable for highly turbulent applications where surface drag is of importance.

2. Low y^+ wall treatment.
   No explicit assumptions are made and the flow near the wall boundaries are resolved. The wall shear stress is calculated as it would be in a Direct Numerical Simulation. However, this wall treatment requires extremely fine meshes and is generally only suitable for low Reynolds numbers.

3. All y^+ wall treatment.
   This treatment uses a blended wall law to estimate shear stress, and the results are similar to the low y^+ wall treatment if the mesh is fine enough. CD-Adapco (2012) suggests that the all y^+ wall treatment be used whenever STAR-CCM+® allows it to be used. The all y^+ wall treatment can only be selected after the appropriate meshing models were chosen. CD-Adapco (2012) also suggests to generate the mesh so that $y^+ < 3$ when drag is of importance.

Calis et al. (2001) found it difficult to meet the y^+ criterium everywhere on particle surfaces when using high y^+ type wall treatments, because of large deviations in velocity around particles. Keeping this in mind, as well as the guidelines by CD-Adapco (2012), it was decided to use the all y^+ wall treatment with $y^+ < 3$ for all simulations.

4.6 Turbulence modelling

Section 2.7.4 showed that many authors have investigated the influence of turbulence solvers on the simulation of the flow through packed beds. Most concluded that more computationally demanding models, such as LES and RSM, offer little improvement in accuracy over less computationally demanding models such as $k - \epsilon$ models. The differences between the results of various $k - \epsilon$ models were also small.

In the current investigation the influence of the Realisable $k - \epsilon$ model and LES on the flow through packed beds were investigated. This was done using the reference bed with the mesh conditions as described in Section 4.5, with $B = 2$ mm.

Figs. 4.14a and 4.14b show the transient solutions for Δp using LES, for $Re_p = 10^3$ and $Re_p = 10^4$ respectively. The $Re_p = 10^3$ case was simulated for 30 s, and the $Re_p = 10^4$ case for 3 s. In order to obtain representative average values of the pressure drop for the transient solutions, running averages were calculated by integrating Δp over a time interval using the trapezium rule. For the case with $Re_p = 10^3$ running averages with intervals of 5 and 10 s were calculated, and for $Re_p = 10^4$ the intervals were 0.5 and 1.0 s. These running averages were compared with the steady state solution for Δp of the $k-\epsilon$ model, as shown in Fig. 4.15.

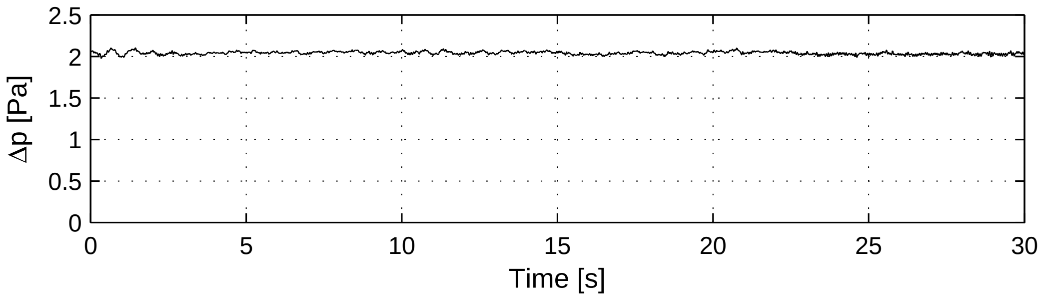

(a) $Re_p = 10^3$ for 30 s.

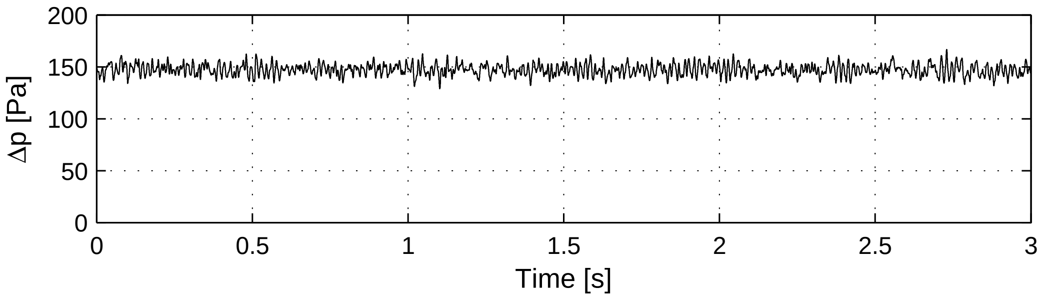

(b) $Re_p = 10^4$ for 3 s.

Figure 4.14: Pressure drop over the reference bed using LES.

Fig. 4.15 shows that the differences in Δp between the $k-\epsilon$ model and LES were small. The difference in Δp between $k-\epsilon$ and LES 30 s being 0.77% for $Re_p = 10^3$, and 1.01% between $k-\epsilon$ and LES 3 s for $Re_p = 10^4$. These small differences did not justify the additional computational effort required by LES, thus it was decided to use the Realisable $k-\epsilon$ model as the turbulence solver in the current investigation.

4.7 Inlet boundary conditions

As described in Section 2.7.5, a realistic representation of the flow entering a packed bed is fully developed viscous flow. Thus, in order to simulate realistic conditions, it was decided to specify fully developed flow at the inlet boundary. Velocity profiles for fully developed laminar and turbulent flows were calculated with eqns. (2.19) and (2.20) respectively. These velocity profiles were specified at the inlet boundaries as a function of the radial coordinate, r. In the case of turbulent flow, a viscosity ratio of $\mu^\tau/\mu = 10$ and turbulence velocity intensity of $\gamma = 0.01$ was specified. These are the default values proposed by STAR-CCM+®.

4.8 Packed bed length

Section 2.3.3 described the porosity variations in the axial direction as the length effect. However, the limit where the influence of the length effect on the fluid flow can be neglected is still

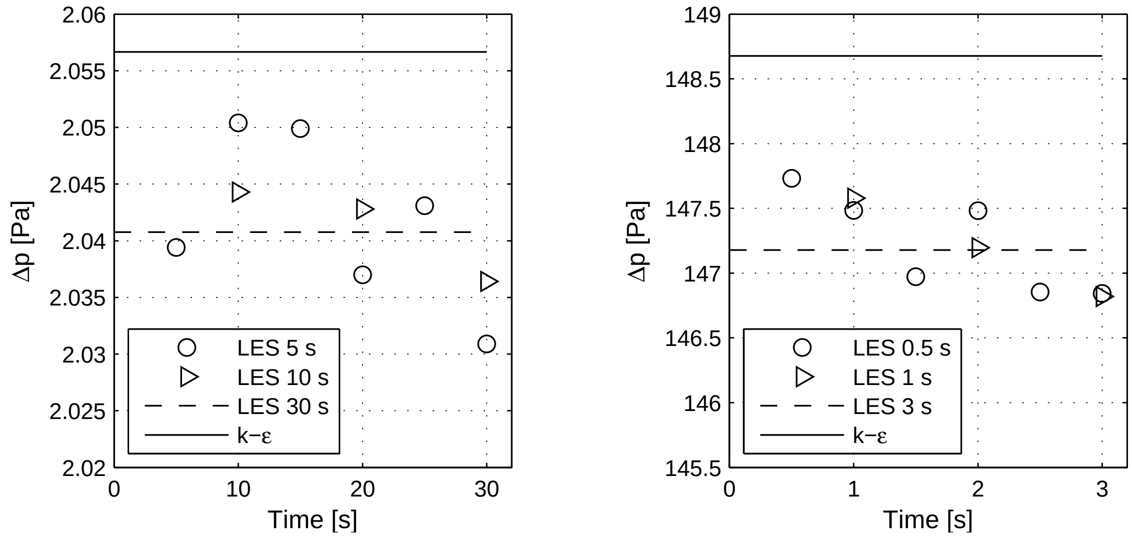

(a) $Re_p = 10^3$. (b) $Re_p = 10^4$.

Figure 4.15: Comparison between the $k - \epsilon$ model and LES, with running averages for LES.

not well defined. The influence of the axial length of the test bed on the pressure drop was investigated. Fig. 4.16 shows that Δp increases linearly with increasing L/d.

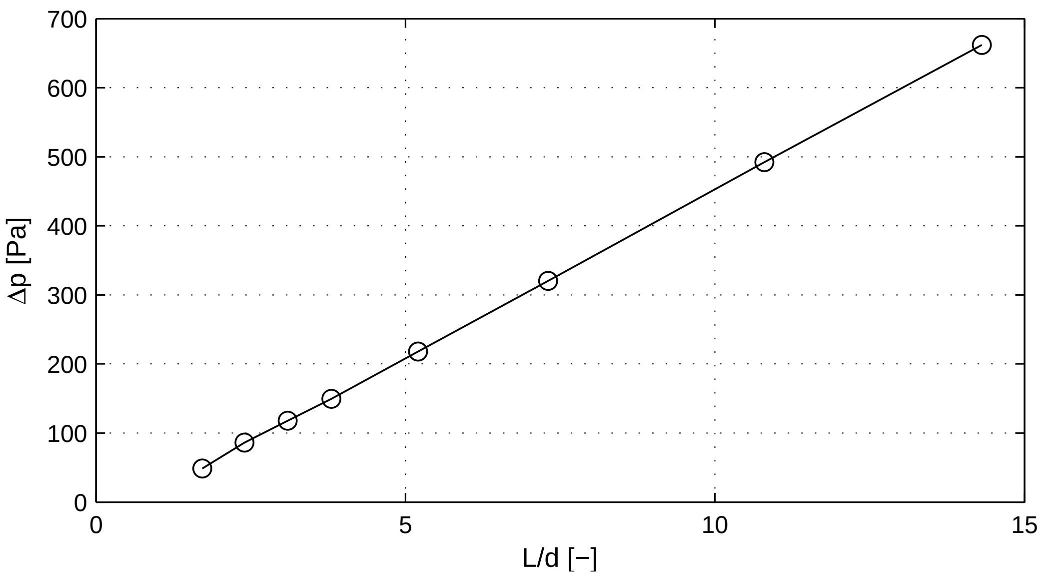

Figure 4.16: Pressure drop over the reference bed as a function of the axial length of the bed, L, at $Re_p = 10^4$.

Reddy and Joshi (2010) used L/d ratios of 7.13, 7.05 and 13.08 for their CFD analyses of beds with aspect ratios of 3, 5 and 10 respectively. Eppinger et al. (2011) simulated the flow over beds with aspect ratios of $3 \leq \alpha \leq 10$, and used beds with $L/d \simeq 12$ for all aspect ratios.

In order to keep the influence of the length effect on the fluid flow as low as reasonably possible, while also considering the increased computational demand of higher L/d ratios, it was decided to use ratios of $L/d \simeq 10$ for all simulations.

4.9 Pressure drop measurement

The change in static and total pressures as a function of the axial coordinate, z, of the bed was analysed using the reference bed, containing 20 particles with a uniform diameter of $d = 49.8$ mm. The bed was divided into a number of cross sections, with the distance between each section $z_{k+1} - z_k = 1.0$ mm. The pressures were then monitored by calculating the average pressure on each cross section, at a level z. Fig. 4.17 shows the change in total and static pressure as a function of the dimensionless axial coordinate, z/d, as well as the variation in porosity in die axial direction. The plotted pressure is relative to atmospheric pressure.

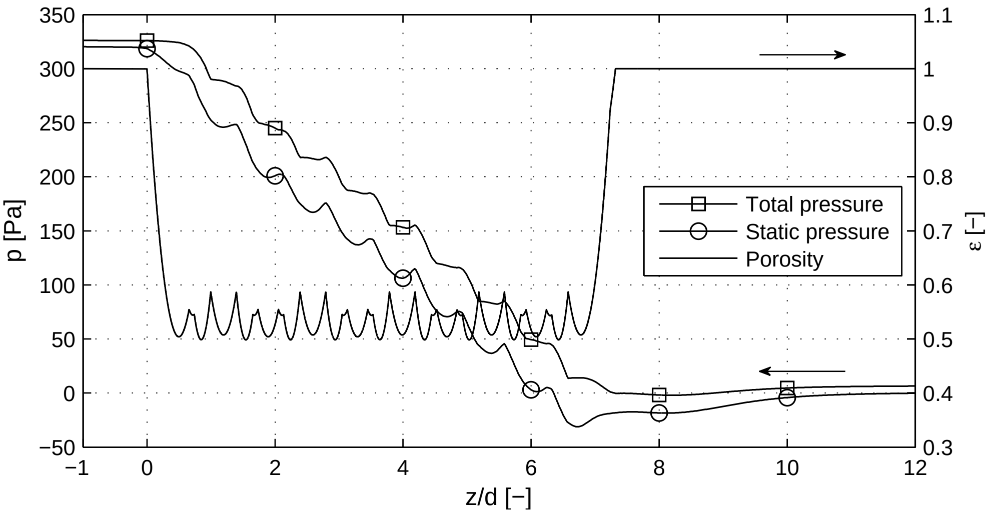

Figure 4.17: Change in total and static pressure as a function of the dimensionless axial coordinate of the reference bed, $\alpha = 2.01$ with 20 particles, at $Re_p = 10^4$.

Localised recovery of static pressure can be observed, which coincide with approximately every second upward peak of the porosity. Considering the structure of the reference bed, with an aspect ratio of $\alpha = 2.01$, each second upward peak of $\varepsilon(z/d)$ coincides with the start of new particles. This indicates that the localised recovery of static pressure is a result of the variation in porosity, as well as stagnation points in the flow. Similar variations in pressure can be observed in Fig. 2.13. However, Bai et al. (2009) did not give detail on how they measured the results presented the Fig. 2.13. It can also be seen that a region with negative pressure forms just after the particles, and extends for approximately five particle diameters towards the outlet, after which it recovers to atmospheric pressure. This low pressure region formed due to vortices just after the last particles in the bed.

Because of the localised recovery of static pressure, and the region with negative pressure just after the particles, it was decided to take the measurement of the pressure drop over the bed as the pressure difference between the pressure at the inlet boundary and atmospheric pressure. That is $\Delta p = p(z/d = -1) - p(z/d = 12)$ on Fig. 4.17. This method is similar to that employed by Eppinger et al. (2011), Reddy and Joshi (2010) and Bai et al. (2009) and ensured that the measurements of Δp would not be influenced by local pressure variations.

Localised recovery of total pressure can also be observed in Fig. 4.17. At first glance this might seem erroneous, however Issa (1995) demonstrated that total pressure could indeed increase in turbulent, viscid flows, particularly around stagnation points. Issa (1995) also noted that localised rises of total pressure can only occur at the expense of depletion of total pressure elsewhere in the flow, as mechanical energy stays conserved. Thus, the localised recovery of total pressure can also be attributed to the variation in porosity and stagnation points in the flow. The consequences that these local rises of total pressure may have on the flow through packed beds, however, fall beyond the scope of the current investigation. Further analysis will be needed to determine the influence that these rises might have on the temperature distribution within packed beds.

The recovery of total pressure between the last particles and the outlet in Fig. 4.17, could be a result of vortices forming after the particles, as the energy contained in the vortices may not be properly accounted for with total pressure. However, this increase might also be due to the outlet boundary having an effect on the upstream flow.

4.10 Summary

This chapter described the steps taken during the numerical analyses of the flow through packed beds, to ensure accurate solutions with a reasonable degree of confidence. Preller (2011) and Theron (2011) proved that STAR-CCM+® is an appropriate platform to generate packed beds using DEM, and performing CFD analysis of the flow through packed beds. This chapter extended on the work done by Theron (2011).

Detail of the setup used for the DEM simulations to generate all the beds was given, as well as detail of the setup used for the CFD simulations of the flow through the beds. The geometry of the reference bed was described, which was used to analyse the influence of some key factors on the simulation of the fluid flow between particles. These factors included the mesh density, contact treatment, turbulence modelling, boundary conditions and measurement of the pressure drop. The influence of these factors on the simulations was also described in detail. The methods developed and setups described in this chapter were used to simulate the flow through DEM generated packed beds explicitly. The results of these simulations are presented in the next chapter.

Chapter 5

Results

This chapter contains the results from the CFD simulations of the flow through DEM generated packed beds. All DEM and CFD simulations were run with the methods developed in Chapter 4. The results provide evidence of the global effects that the geometry and the flow parameters, as characterised by the aspect ratio and the Reynolds number respectively, have on the flow through the packed beds considered. Since this investigation focussed on these global effects, the results are presented as an overview, without excessive detail of the flow.

5.1 Analysis of DEM generated beds

Tab. 5.1 shows the values of important parameters pertaining to the beds generated with DEM. Beds with aspect ratios $1.6 \leq \alpha \leq 25.0$ were generated, with $L/d \simeq 10$. This section contains the analysis of the DEM generated beds in terms of quality and structure.

Table 5.1: Parameters of DEM generated beds.

α [-]	D [mm]	d [mm]	L [mm]	L/d [-]	N [-]
1.60	100	62.50	612.801	9.80	12
2.01	100	49.80	505.517	10.15	28
2.50	100	40.00	411.362	10.28	44
3.00	100	33.33	340.476	10.21	74
3.65	100	27.397	281.828	10.29	102
4.00	100	25.00	258.578	10.34	125
5.00	100	20.00	208.448	10.42	210
6.33	100	15.798	160.597	10.17	335
10.00	100	10.00	105.175	10.52	890
15.00	105	7.00	71.430	10.20	1970
20.00	100	5.00	52.507	10.50	3640
25.00	100	4.00	42.113	10.53	5750

5.1.1 Particle overlaps

The quality of the DEM generated beds were assessed by calculating the overlap, d_o, between adjacent particles (Du Toit and Rosslee, 2012). Ideally there should be no overlap. The distance d_{ij} between spheres i and j was calculated using eq. (5.1), where x_i, y_i, z_i and x_j, y_j, z_j are the coordinates of the centres of the spheres. The percentage overlap, d_o, was then calculated using eq. (5.2), and Fig. 5.1a shows the maximum and minimum overlaps. It can be seen that the overlaps between adjacent particles in the beds generated using DEM were small, with $d_{o,max} < 0.08\%$ for all beds.

$$d_{ij} = \sqrt{(x_i - x_j)^2 + (y_i - y_j)^2 + (z_i - z_j)^2} \tag{5.1}$$

$$d_o = \begin{cases} (d - d_{ij}) \times 100/d & \text{for} \quad d > d_{ij} \\ 0 & \text{for} \quad d \leq d_{ij} \end{cases} \tag{5.2}$$

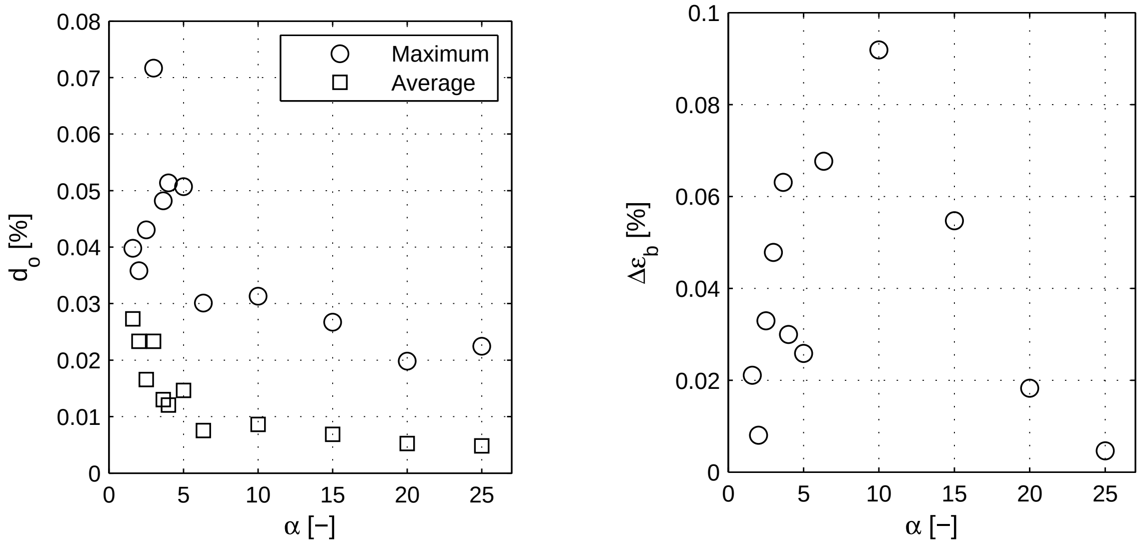

(a) Overlap between particles. **(b)** Difference between eqns. (2.3) and (2.6).

Figure 5.1: Quality analysis of the DEM generated packed beds, with values given in Tab. 5.1.

5.1.2 Porosity and structure

Bulk porosities were calculated with both the analytical expression of Bai et al. (2009), eq. (2.3), and the numerical expression of Du Toit and Rosslee (2012), eq. (2.6). These porosities were calculated taking z_1 as the lowest and z_{n-1} as the highest point in the bed, and $\Delta z = 0.01d$. Fig. 5.1b shows the percentage difference between these calculated bulk porosities. It can be seen that there is a good agreement between the analytically and numerically calculated values for ε_b, where $\Delta\varepsilon_b < 0.1\%$ for all beds. Note that the numerical solution tended to the analytical solution as $\Delta z \to 0$.

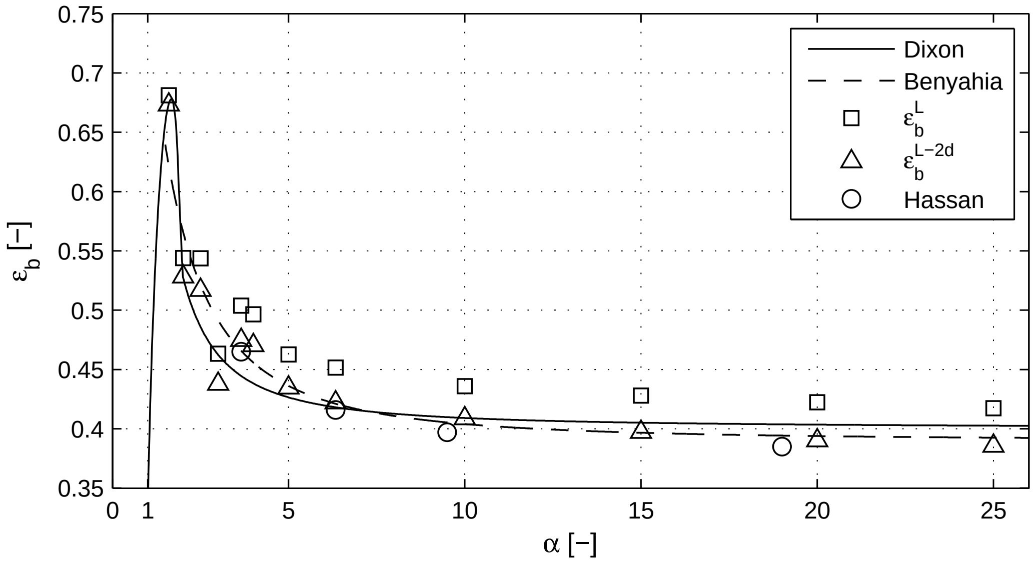

Figure 5.2: Bulk porosities of the DEM generated beds.

The bulk porosities of the beds generated with DEM were also compared with the bulk porosities predicted by the correlations proposed by Dixon (1988), eq. (2.7), and Benyahia and O'Neill (2005), eq. (2.8). Fig. 5.2 shows this comparison, with ε_b^L the bulk porosity based on the entire length of the bed. However, ε_b^L included the effect of the bottom and top particles and therefore suffered from the length effect (see Section 2.3.3).

An approximation was made to exclude the length effect in an attempt to determine the bulk porosities. This was done by calculating the bulk porosities for the part of each bed between one particle diameter from the bottom and one particle diameter from the top, ε_b^{L-2d}. Fig. 5.3 shows the porosity variation in the axial direction as a function of the dimensionless length, z/d, for the bed with $\alpha = 6.33$, and shows schematically the lengths on which ε_b^L and ε_b^{L-2d} were based.

Fig. 5.2 shows that there was a better agreement between the predicted values for bulk porosity and ε_b^{L-2d}, than between the predicted values and ε_b^L. This suggests that the length of the DEM generated beds, with $L/d \simeq 10$, was insufficient to completely eliminate the length effect as was done by Dixon (1988). Fig. 5.2 also shows the bulk porosities measured by Hassan and Kang (2012), which are also in agreement with the predicted values.

The variation in porosity in the axial direction calculated with eq. (2.6), as a function of the dimensionless length, z/d, for all DEM generated beds is shown in Fig. 5.4. Zou and Yu (1995) observed disordered, random packings for aspect ratios of $3.906 \leq \alpha$, and ordered packings for $\alpha \leq 1.859$. They also noted that the transition from ordered to random structures is not so smooth, and results in a transition region for $1.859 \leq \alpha \leq 3.906$. Similar results could be observed from Fig. 5.4, where at low aspect ratios the structure was ordered, and at higher aspect ratios the structure became random. However, Fig. 5.4 show that ordered structures could be observed for $\alpha \leq 2.01$, and that the limits of the transition region could not be easily defined. Fig. 5.4a shows that the porosity increased sharply for $\alpha = 1.60$, which corresponded to the increase in bulk porosity for $\alpha < 2$, as shows in Fig. 5.2. Fig. 5.4c shows sharp peaks in the porosity for $\alpha = 2.50$. Fig. 5.4d shows a very long length effect compared to other

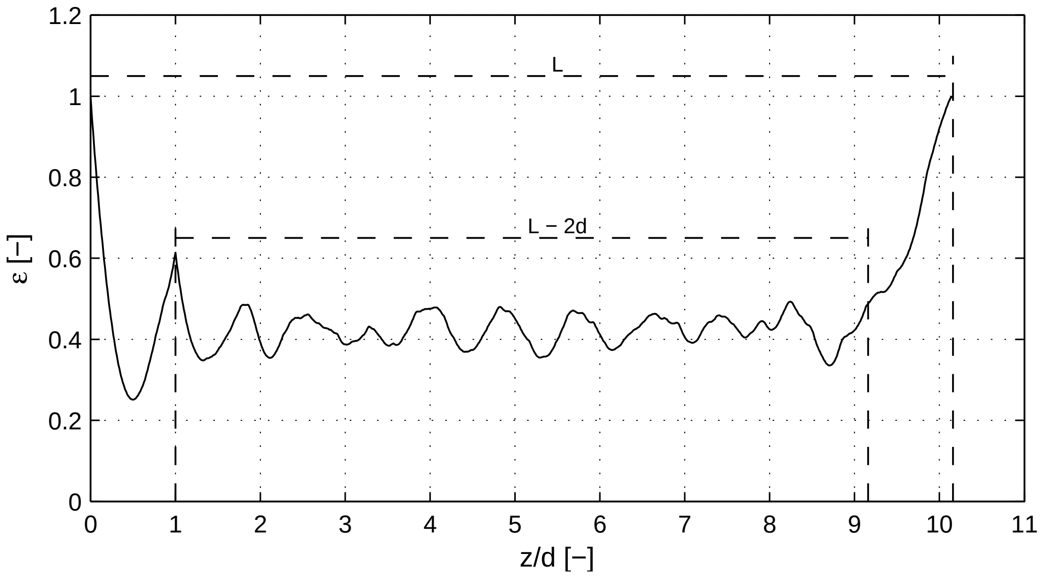

Figure 5.3: Porosity variation in the axial direction for $\alpha = 6.33$, with bulk porosities including, L, and excluding, $L - 2d$, the length effect.

aspect ratios, reaching about 6 particle diameters into the bed and then suddenly shifting to a random structure. Figs. 5.4e to 5.4l show that the length effect increases in length and number of oscillations as the aspect ratio increases, for $3.65 \leq \alpha$. It can also be seen that for larger values of α, the effect of the bottom of the cylinder is similar to that of the cylinder wall, as depicted in Fig. 2.4.

Fig. 5.5 shows the coordinates of the centre points of the particles for each DEM generated bed, when looking down the length of the bed. For $2.50 \leq \alpha$ a structured packing could be observed for the particles adjacent to the cylinder wall. Also, as the aspect ratio increased, the influence of these structured particles on the overall packing decreased.

5.2 Computational resources

For each explicit simulation a minimum number of cells was required to have a mesh independent solution, as shown in Section 4.5.4. Also, as the number of cells increases, so does the computational time and resources needed to obtain a converged solution. The resources available at NWU could accommodate simulations with less than roughly 20 million cells. With the results from the mesh independence study, Section 4.5, and through trial and error, it was found that each bed required roughly 62000 cells per particle in the bed to have a mesh independent solution, using the methods developed in Chapter 4. This, unfortunately, meant that the flow through beds with more than about 320 particles could not be solved with the available resources. Looking at Tab. 5.1 for the number of particles, N, the largest aspect ratio for which the flow through the bed could be modelled was $\alpha = 6.33$.

As mentioned in Section 2.5, Hassan and Kang (2012) did experiments on beds with aspect ratios of $\alpha = 19$, 9.5, 6.33 and 3.65, and compared their experimental measurements for pressure drop with the values predicted by the KTA correlation. They found that the pressure drop

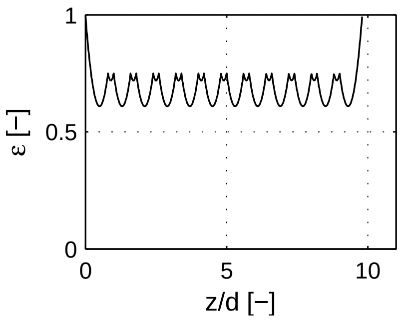

(a) $\alpha = 1.60$.

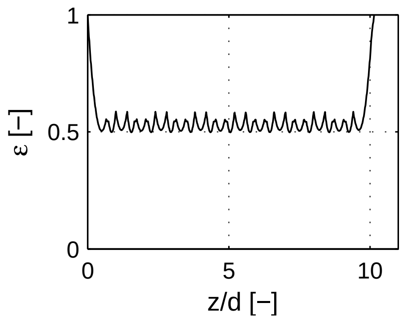

(b) $\alpha = 2.01$.

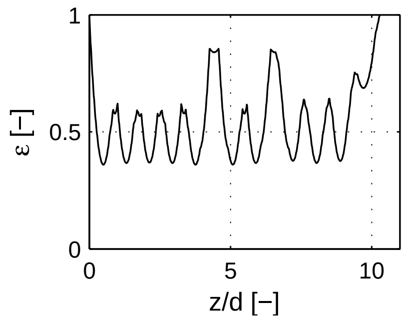

(c) $\alpha = 2.50$.

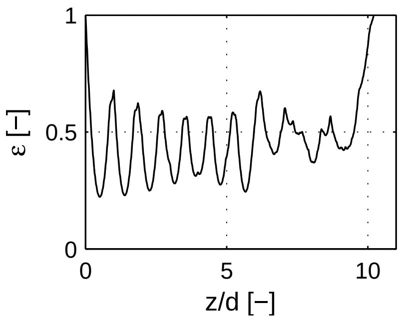

(d) $\alpha = 3.00$.

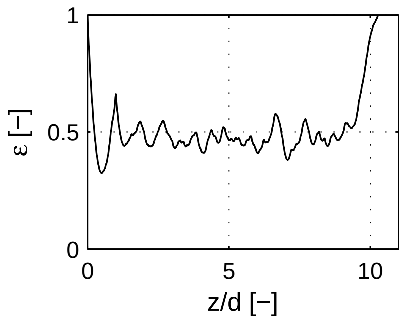

(e) $\alpha = 3.65$.

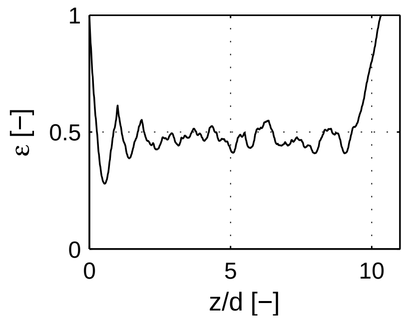

(f) $\alpha = 4.00$.

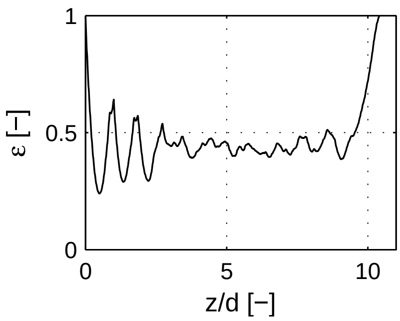

(g) $\alpha = 5.00$.

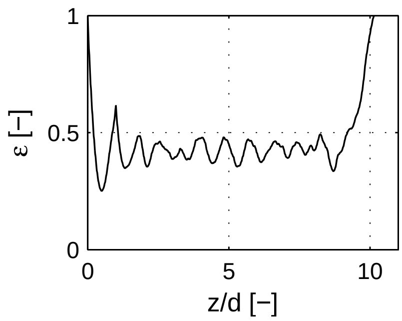

(h) $\alpha = 6.33$.

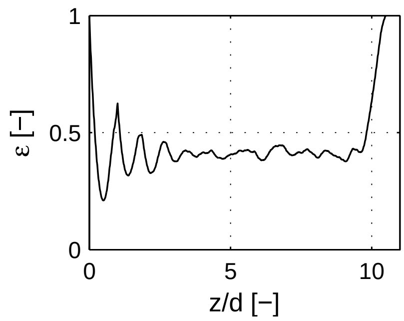

(i) $\alpha = 10.00$.

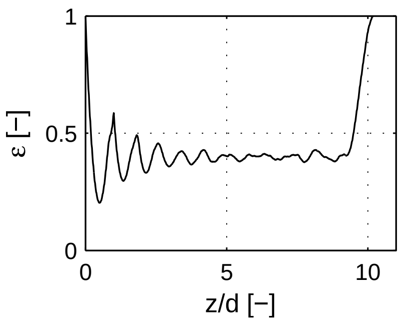

(j) $\alpha = 15.00$.

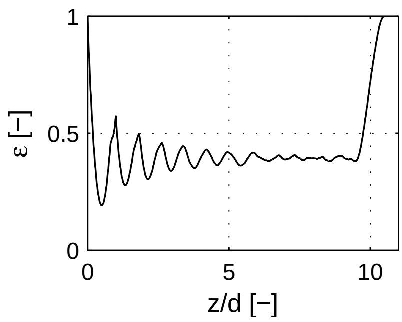

(k) $\alpha = 20.00$.

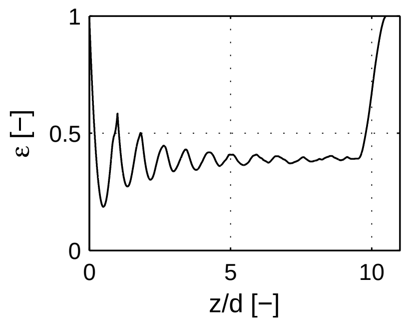

(l) $\alpha = 25.00$.

Figure 5.4: Porosity variation in the axial direction, calculated with eq. (2.6), as a function of the dimensionless length, z/d, for all DEM generated packed beds.

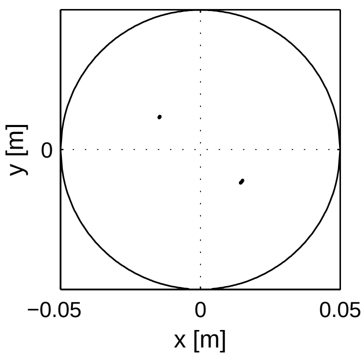

(a) $\alpha = 1.60$.

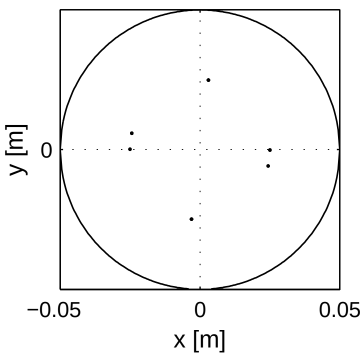

(b) $\alpha = 2.01$.

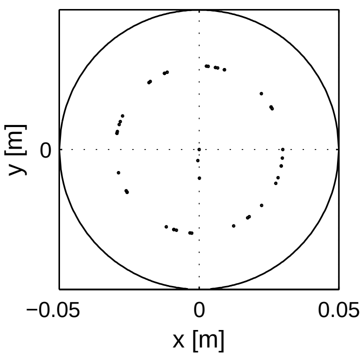

(c) $\alpha = 2.50$.

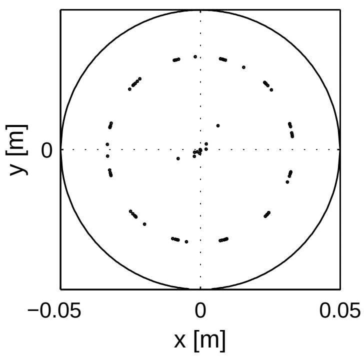

(d) $\alpha = 3.00$.

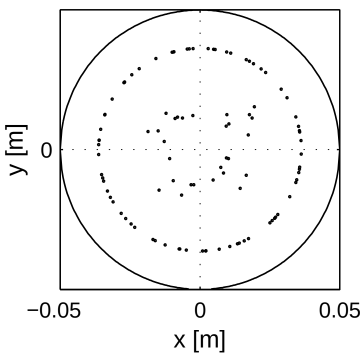

(e) $\alpha = 3.65$.

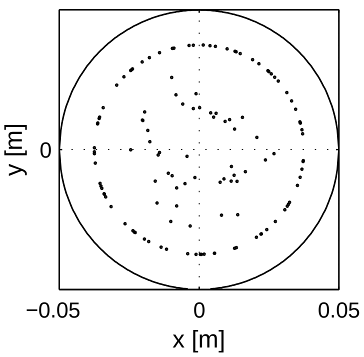

(f) $\alpha = 4.00$.

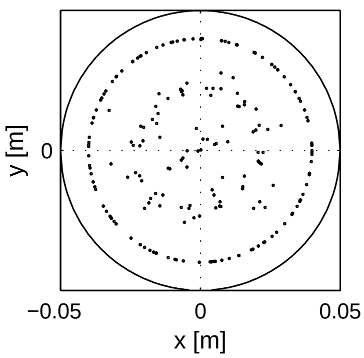

(g) $\alpha = 5.00$.

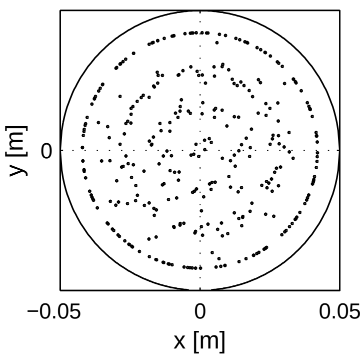

(h) $\alpha = 6.33$.

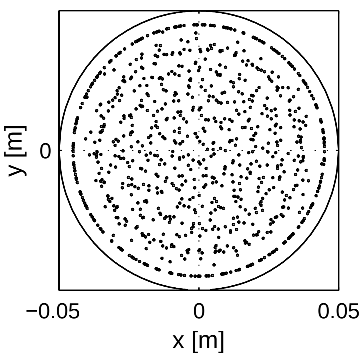

(i) $\alpha = 10.00$.

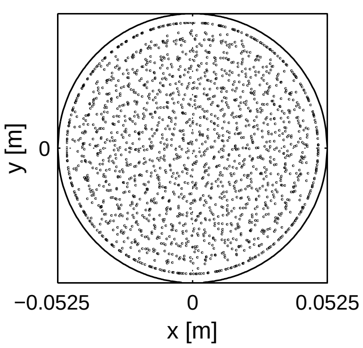

(j) $\alpha = 15.00$.

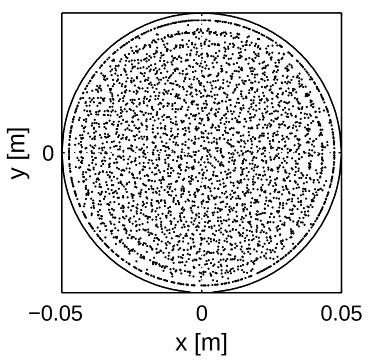

(k) $\alpha = 20.00$.

6

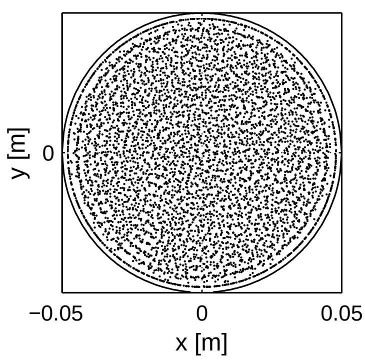

(l) $\alpha = 25.00$.

Figure 5.5: Plots of the coordinates of the centre points of the particles for each DEM generated bed.

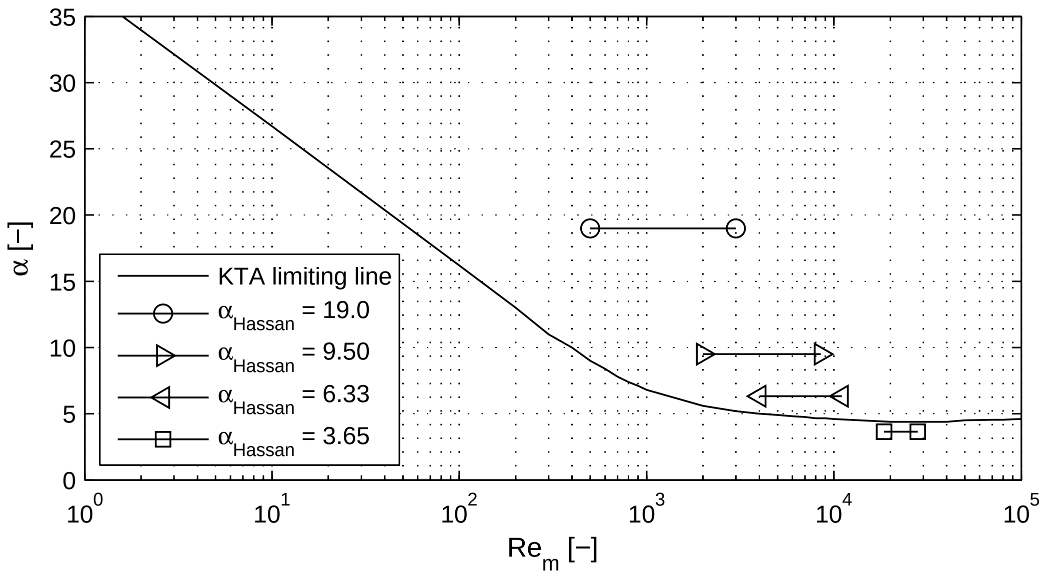

Figure 5.6: KTA limiting line with the ranges of the experiments done by Hassan and Kang (2012).

measurements for the beds with large aspect ratios ($\alpha = 19$, 9.5 and 6.33) matched very well with the values predicted by the KTA correlation. However, in the case of $\alpha = 3.65$, the values predicted by the KTA correlation did not correspond with the experimental measurements. Looking then at Fig. 5.6, which shows the KTA limiting line as well as the ranges of the experiments done by Hassan and Kang (2012), it could be concluded that the KTA limiting line is indeed valid within that range.

It was decided then to simulate the flow through beds with aspect ratios of $\alpha = 1.60$, 2.01, 2.50, 3.00, 3.65, 4.00, 5.00 and 6.33 for a wide range of Re_m, with the goal of confirming the results found by Hassan and Kang (2012). The results from these simulations could then be used to still reach the goals of the current investigation, despite the fact that the flow through beds with larger aspect ratios could not be simulated due to limited resources.

Fig. 5.7 shows the number of cells generated for each bed as a function of the number of particles in the bed. It can be seen that the number of cells, generated with the methods developed in Chapter 4, increases almost linearly with the number of particles in the bed.

5.3 Validation

In order to validate the methodology developed in Chapter 4, the flow through the beds was simulated for which experimental measurements for the pressure drop were available in literature. The two experimental studies used for validation was that of Hassan and Kang (2012) and Wentz and Thodos (1963). In this section the validation process is described and the pressure drops predicted by the CFD simulations are compared with the experimental measurements of Hassan and Kang (2012) and Wentz and Thodos (1963).

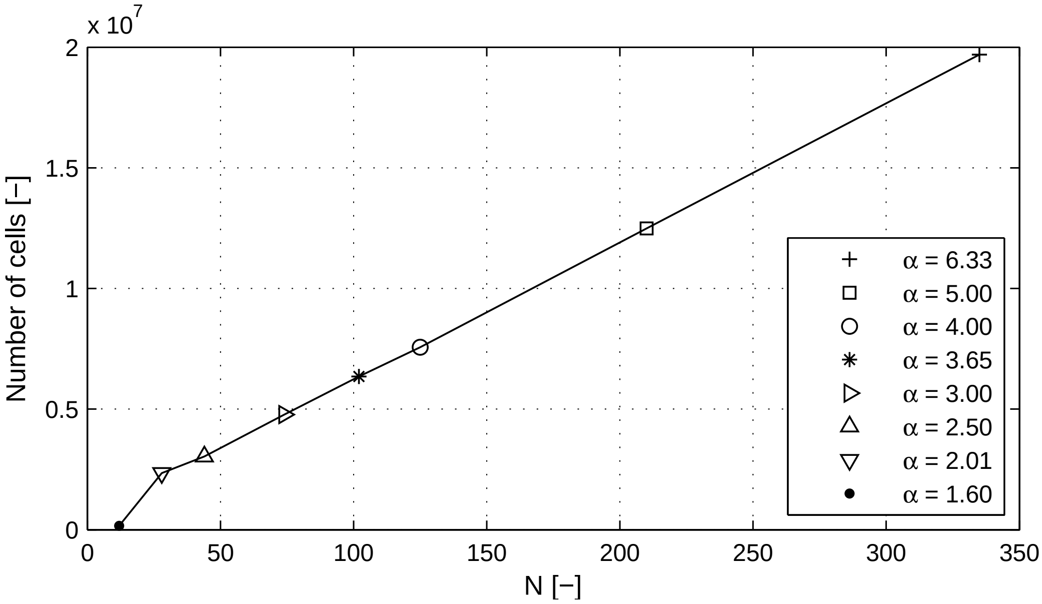

Figure 5.7: Number of cells generated for each bed as a function of the number of particles in the bed, N.

5.3.1 Wentz and Thodos

Wentz and Thodos (1963) made structured packed beds using plastic phenolic spheres, 1.23 in. in diameter, which were fixed in space with short lengths of wire. Their structured packings were arranged in cubic, body centred cubic and face centred cubic orientations. Each packing arrangement had five layers of particles in the axial direction. The beds were machined to fit into a cylindrical wind tunnel, 14 in. in diameter, by removing excess portions of the external spheres to eliminate the wall effect. The bottom of the wind tunnel was connected to the suction en of a centrifugal blower, and a sliding window permitted the flow of air to be varied from 2.5 to 13.4 ft./s. Two parallel perforated steel plates were placed 6 in. apart across the inlet of the wind tunnel to ensure uniform air velocities. The air velocity was measured 26 in. above the bed with a sliding pitot tube, which was connected to a micro-manometer. They measured the pressure drop through the bed using static pressure taps mounted perpendicularly into the walls of the wind tunnel, 5 in. upstream and 7.5 ft. downstream of the bed.

Table 5.2: Bulk porosities as measured by Wentz and Thodos (1963), and calculated from the DEM generated beds using eq. (2.6).

Parameter		Cubic structure	Body-centred structure
Wentz	ε_b	0.480	0.354
DEM	ε_b	0.471	0.365

The beds with cubic and body-centred cubic structures were recreated as simulation models, Fig. 5.8, and the flow through them was simulated using the methods developed in Chapter 4. Wentz and Thodos (1963) employed a water displacement method to measure the bulk porosities of the beds. Tab. 5.2 shows these measurements, as well as the porosities of the recreated simulation models. The small differences in the porosities could be a result of simulation models not capturing some of the detail of the beds made by Wentz and Thodos (1963), such as the wires that were used to connect the particles. The differences could also be a result of the simulation models not being an exact recreation, as the extent of the machining that Wentz and Thodos (1963) did on their beds is uncertain.

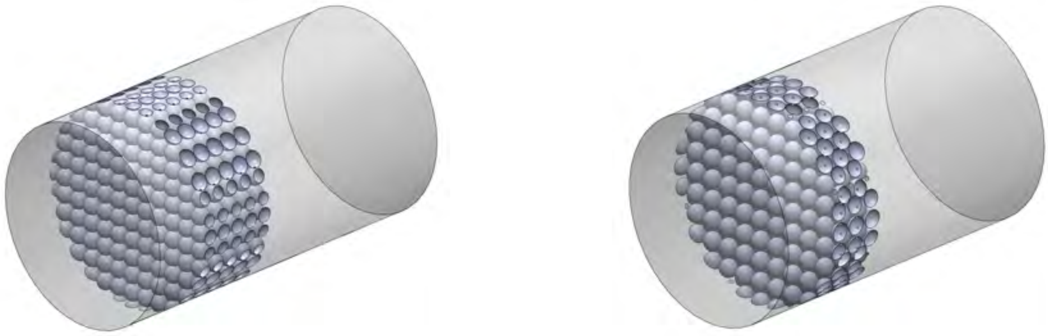

(a) Cubic structure. **(b)** Body-centred structure.

Figure 5.8: Recreated simulation models for validation with the experimental measurements by Wentz and Thodos (1963).

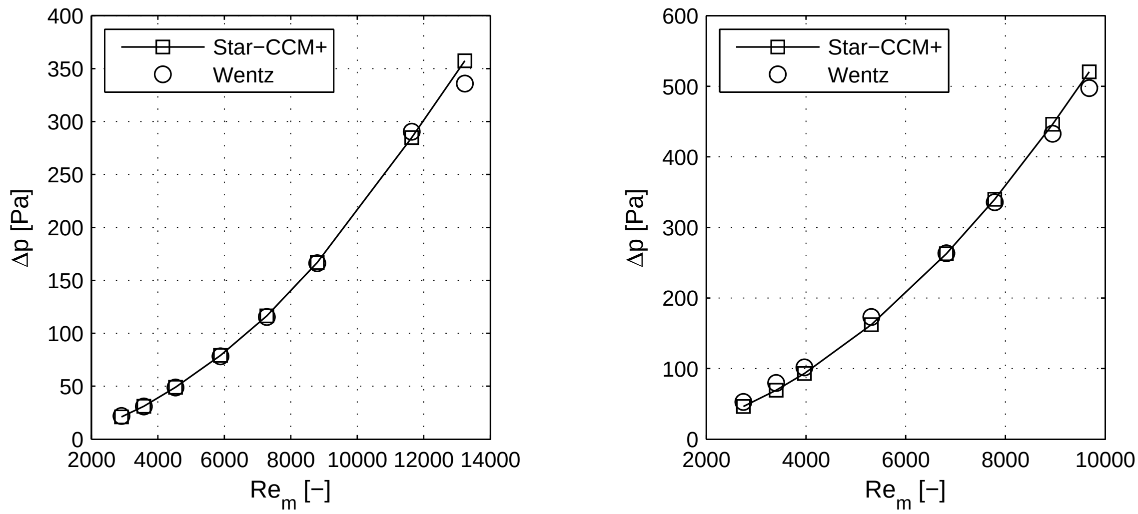

(a) Cubic structure. **(b)** Body centered structure.

Figure 5.9: Validation of CFD model results against measurements by Wentz and Thodos (1963).

Fig. 5.9 shows the pressure drops predicted by the CFD simulations as well as the experimental measurements by Wentz and Thodos (1963). A deviation in measured pressure drop by Wentz and Thodos (1963) can be observed at $Re_m \simeq 13200$ in Fig. 5.9a. This measurement deviates from the trend of the curve and could be attributed to experimental error, however the exact cause is uncertain. Note that a similar, but smaller, discrepancy can be observed in Fig. 5.9b at $Re_m \simeq 9900$. The Normalised Root Mean Square Deviation (NRMSD) for the pressure drop through the cubic- and body centered structures were 2.35% and 2.43% respectively. Fig. 5.9 also shows that the simulation predictions for pressure drop followed the same trend as the experimental measurements. Thus, the pressure drops predicted by the CFD simulations corresponded well with the experimental measurements by Wentz and Thodos (1963).

5.3.2 Hassan and Kang

Hassan and Kang (2012) designed an experimental setup to measure pressure drops over randomly packed beds with aspect ratios of $\alpha = 19$, 9.5, 6.33 and 3.65. Their cylindrical container, 12.065 cm in diameter and 152.4 cm in height, was constructed from Poly(methyl methacrylate) (PMMA) and was filled with PMMA beads. Both air and water were used as working fluids. For the setup that used air Hassan and Kang (2012) monitored the pressure at various pressure tabs along the length of the bed, using Magnehelic differential pressure gauges and inclined vertical manometers. The suction ends of two blowers were connected to the bottom of the container, and the bed had two knit meshes at the ends of both sides to ensure uniform air velocities. In order to use water, the experiment was modified to work in a closed loop configuration, and a 3 hp. pump drove the fluid. Piezoelectric pressure transducers were used to measure the pressure at the various pressure tabs along the length of the bed. A data acquisition system was used to capture the analog signals from the transducers.

The beds with aspect ratios of $\alpha = 6.33$ and 3.65 were recreated as simulation models, and the flow through them was simulated using the methods developed in Chapter 4. Hassan and Kang (2012) employed three different techniques to measure the bed bulk porosities, namely a water displacement method, weight method and particle counting method. The measurements of these three methods were then averaged to obtain the final values. Tab. 5.3 shows these measurements, as well as the porosities of the recreated simulation models. Note that ε_b^L is the bulk porosity of the entire bed, and ε_b^{L-2d} is the bulk porosity of the bed excluding the first and last particle diameters in the axial direction, in an attempt to reduce the length effect. The differences between the porosities could be attributed to the prominent length effect observed in the DEM generated beds. This is discussed in more detail in Section 5.1.2.

Table 5.3: Bulk porosities as measured by Hassan and Kang (2012), and calculated from the DEM generated beds using eq. (2.6).

Parameter		$\alpha = 6.33$	$\alpha = 3.65$
Hassan	ε_b	0.416	0.465
DEM	ε_b^L	0.452	0.504
DEM	ε_b^{L-2d}	0.422	0.475

Fig. 5.10 shows the pressure drops predicted by the CFD simulations as well as the experimental measurements by Hassan and Kang (2012). The flow of air was simulated through the bed with an aspect ratio of $\alpha = 6.33$, Fig. 5.10a, and the flow of water through the beds with $\alpha = 6.33$ and 3.65, Fig. 5.10b. Note that Hassan and Kang (2012) did not present measurements for the flow of air through the bed with $\alpha = 3.65$. It can be seen that the simulated values for $\Delta p/L$ were slightly lower than the measured values. This deviation could be attributed to the deviations in the bulk porosities between the beds, as shown in Tab. 5.3. Since the DEM generated beds had larger bulk porosities the permeability of the beds were higher, and thus the pressure drop lower. Despite the small deviations, these results show that there are good agreement between the pressure drops predicted by the CFD simulations and the experimental measurements of Hassan and Kang (2012).

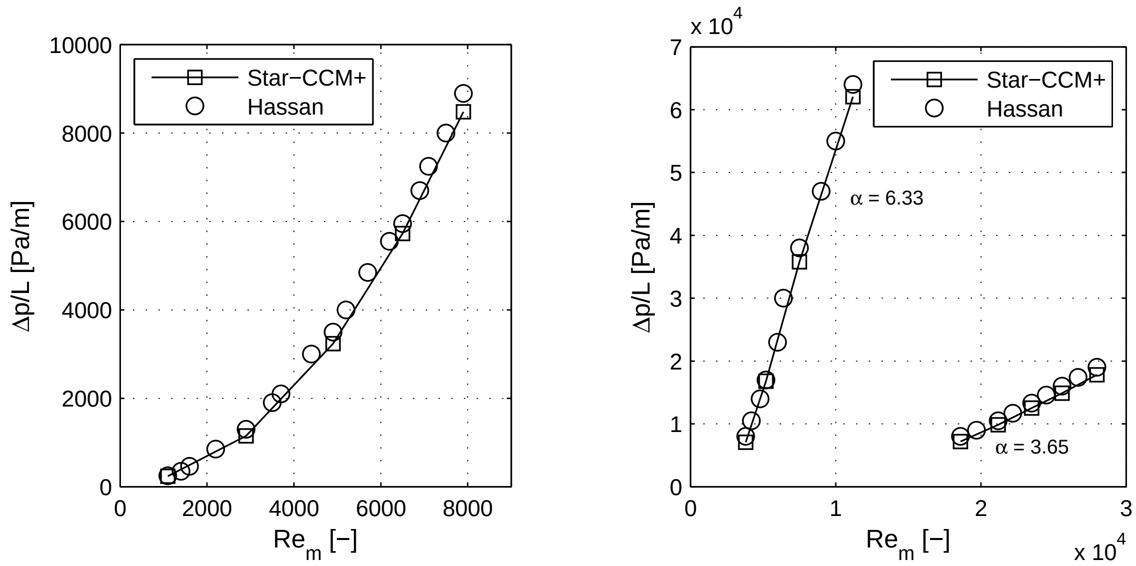

(a) Air, $\alpha = 6.33$.

(b) Water, $\alpha = 6.33$ and 3.65.

Figure 5.10: Validation of CFD model results against measurements by Hassan and Kang (2012).

5.4 Pressure drop

Fig. 5.11 shows the pressure drop predictions per unit length from the CFD simulations for each bed as a function of the modified Reynolds number. It can be seen that the pressure drop over packed beds follow a distinct trend with respect to Re_m. Also, the trend does not vary between beds with different aspect ratios, but differs only in magnitude.

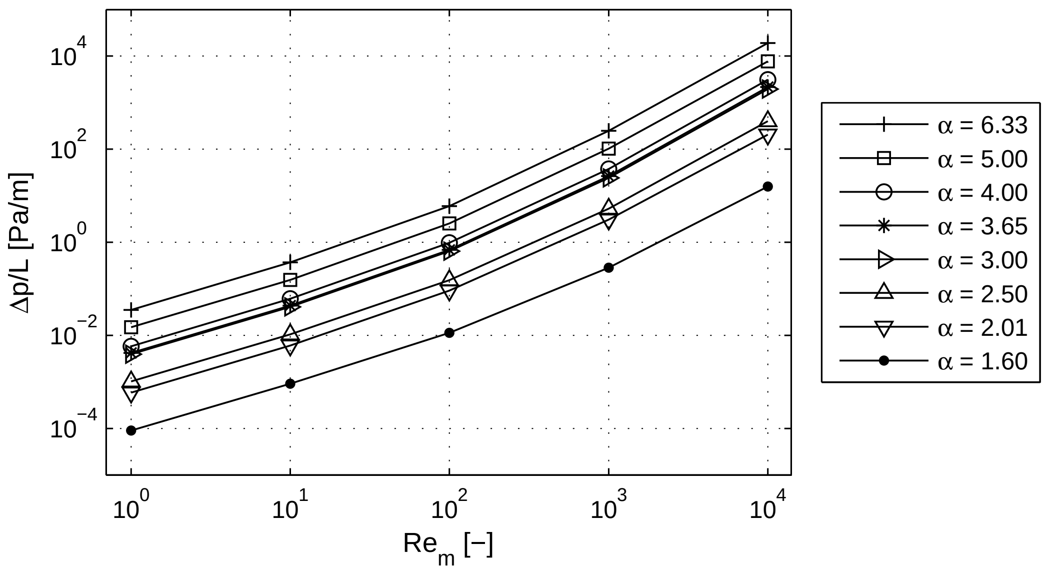

Figure 5.11: Pressure drop per unit length predicted by the CFD simulations as a function of Re_m.

5.5 Friction factor

It is common practice in literature to compare values for predicted friction factors, as it is dimensionless, to evaluate different correlations which were derived to predict the pressure drop over packed beds. The friction factors for the CFD simulations were calculated from the measured pressure drops using eq. (2.13). Fig. 5.12 shows the comparisons between the values for predicted friction factors from the CFD simulations, Ψ_{CFD}, the Eisfeld & Schnitzlein (ES) correlation, Ψ_{ES}, and the KTA correlation, Ψ_{KTA}, for the various cases that were considered.

It can be seen that Ψ_{CFD} compared well with Ψ_{ES} for all instances. Ψ_{CFD} fell within the 18% NRMSD, with a confidence level of 95%, of the ES correlation. Since the ES correlation was developed from more than 2300 experimental data points, the correspondence between Ψ_{CFD} and Ψ_{ES} is also a good indication of the accuracy of the CFD simulations.

However, Ψ_{KTA} did not correspond well with either Ψ_{CFD} or Ψ_{ES}, particularly at low aspect ratios and low modified Reynolds numbers. Fig. 5.12a, with $\alpha = 1.60$, shows a large discrepancy between Ψ_{KTA} and Ψ_{CFD} and Ψ_{ES}. This indicates the influence of the wall effect since the ES correlation takes the wall effect into account, whereas the KTA correlation does not. As the aspect ratio increases to $\alpha = 6.33$ in Fig. 5.12h, Ψ_{KTA} gradually moves closer to both Ψ_{CFD} and Ψ_{ES}. Which shows the influence of the wall effect decreasing with the increase in aspect ratio. Also, Ψ_{KTA} corresponded better with Ψ_{CFD} and Ψ_{ES} at high modified Reynolds numbers than at low modified Reynolds numbers. This result gives evidence of the fact that the wall effect is Reynolds number dependent, where the pressure drop may increase in creeping flow regimes due to the additional wall friction, and decrease in turbulent regimes due to the increased porosity and permeability.

Fig. 5.12 also shows that results similar to that of Hassan and Kang (2012) were found. Where Ψ_{CFD} corresponded better to Ψ_{KTA} for the bed with $\alpha = 6.33$ than $\alpha = 3.65$. Thus, these results confirm the conclusion by Hassan and Kang (2012) that the KTA correlation cannot be expected to predict accurate pressure drop values for beds with aspect ratios of $\alpha \leq 5$ at high modified Reynolds numbers of $20000 < Re_m < 30000$.

As mentioned above, Ψ_{CFD} compared well with Ψ_{ES} for all instances. Assuming then that the ES correlation predicts accurate values for friction factors within its limits, Ψ_{KTA} was evaluated further in terms of Ψ_{ES} using eq. (5.3).

$$\Delta\Psi_{ES-KTA} = \frac{(\Psi_{ES} - \Psi_{KTA}) \times 100}{\Psi_{ES}} \tag{5.3}$$

In eq. (5.3), $\Delta\Psi_{ES-KTA}$ is the percentage difference between Ψ_{ES} and Ψ_{KTA}. $\Delta\Psi_{ES-KTA}$ was calculated for a wide range of aspect ratios, by predicting the porosity for each aspect ratio using eq. (2.7) by Dixon (1988) (see Fig. 5.2). Fig. 5.13 shows the results of eq. (5.3) in the form of a contour plot as functions of α and Re_m. Keep in mind that the ES correlation has a NRMSD of 18%, thus by assuming the ES correlation is accurate within its limits values for $\Delta\Psi_{ES-KTA} < 18\%$ can be considered as acceptable. Fig. 5.13 also includes the KTA limiting line.

Fig. 5.13 shows that for $\alpha < 10$, the KTA correlation under predicts the friction factor at low modified Reynolds numbers, reaching a maximum deviation of 70% at the smallest aspect

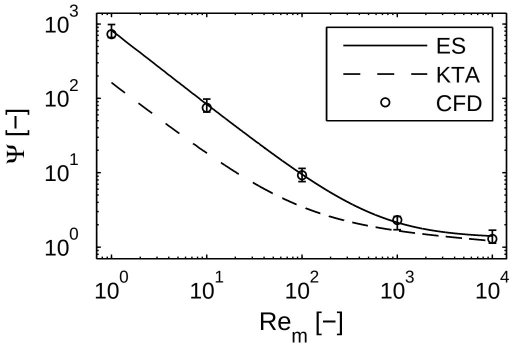

(a) $\alpha = 1.60$.

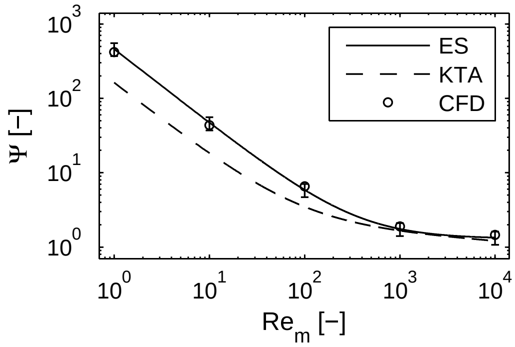

(b) $\alpha = 2.01$.

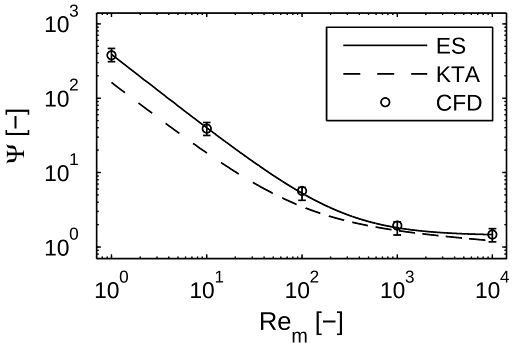

(c) $\alpha = 2.50$.

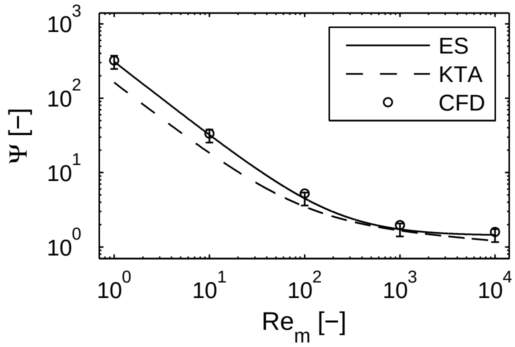

(d) $\alpha = 3.00$.

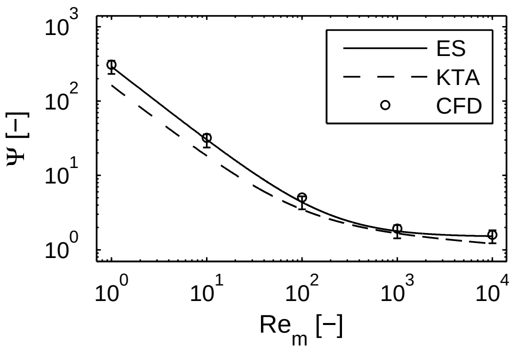

(e) $\alpha = 3.65$.

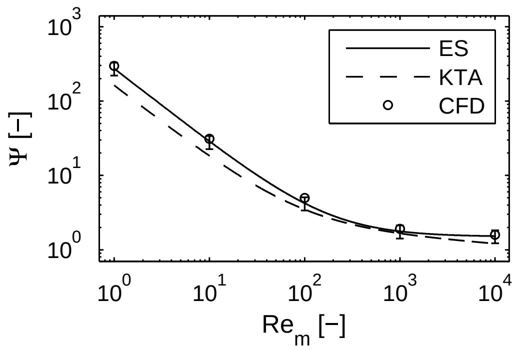

(f) $\alpha = 4.00$.

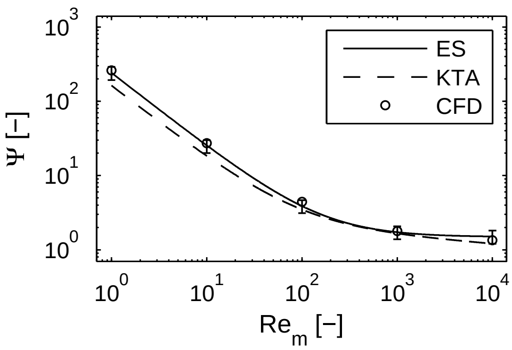

(g) $\alpha = 5.00$.

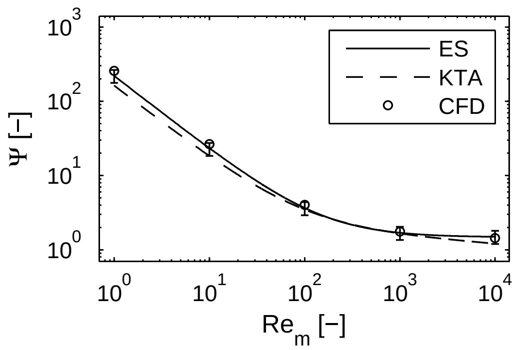

(h) $\alpha = 6.33$.

Figure 5.12: Comparison of friction factors between ES, KTA and CFD simulations as a function of Re_m.

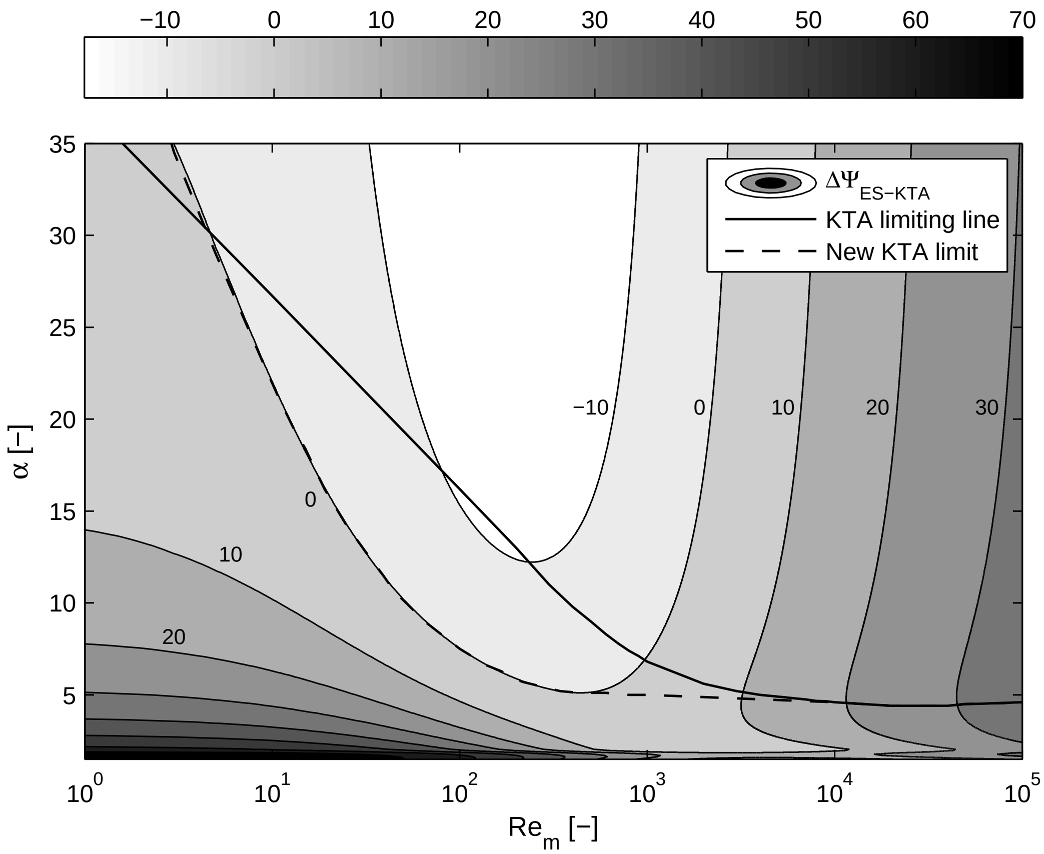

Figure 5.13: Contour plot of the percentage difference between Ψ_{ES} and Ψ_{KTA} as functions of α and Re_m.

ratios. This was to be expected as the same results were observed in Fig. 5.12. At high modified Reynolds numbers of $Re_m > 10^4$ the KTA correlation also under predicts the friction factor. However, it should be noted that the ES correlation is only valid for $Re_m < 3 \times 10^4$. This deviation at high Reynolds numbers can also be attributed to the fact that the ES correlation is based on the Ergun equation, which was developed from non-uniform packings, whereas the KTA correlation was developed using beds with mono-sized spherical particles. Thus, higher predictions for Ψ_{ES} than Ψ_{KTA} was to be expected at high modified Reynolds numbers.

Fig. 5.13 is comparable with the Moody diagram (Munson et al., 2010, p. 413), where at low Reynolds numbers the pressure drop is dominated by viscous effects of the boundary layer. Whereas at large Reynolds numbers the pressure drop is dominated by inertial effects, that is, the effect of the bed particles on the momentum exchange between fluid particles. In other words, at high modified Reynolds numbers the bed structure and permeability have a larger influence on the pressure drop than the wall friction. This indicates that the large values of $\Delta\Psi_{ES-KTA}$ for $Re_m > 10^4$ may not have a significant influence on the actual pressure drop.

Fig. 5.13 also shows that the KTA limiting line is valid, but not exact. It also shows a suggested new KTA limiting line, which falls on the zero line of $\Delta\Psi_{ES-KTA}$ at low Reynolds numbers. However, it is important to note the following assumptions on this new limiting line:

1. Ψ_{CFD} compared well with Ψ_{ES} for all instances simulated at low aspect ratios. Hence,

$\Delta\Psi_{ES-KTA}$ was calculated assuming that the ES correlation predicts accurate values for friction factors within its limits.

2. $\Delta\Psi_{ES-KTA}$ was calculated using values for porosity as predicted by eq. (2.7) as a function of the aspect ratio.

3. The ES correlation is only valid for $Re_m < 3 \times 10^4$ and has a NRMSD of 18% with a confidence level of 95%.

4. The KTA correlation has an uncertainty range of 15% with a confidence level of 95%.

5. The new limiting line was simply drawn on the $\Delta\Psi_{ES-KTA} = 0\%$ line for low Reynolds numbers, keeping in mind that at high Reynolds numbers the packing structure has a larger influence on the pressure drop than the friction factor.

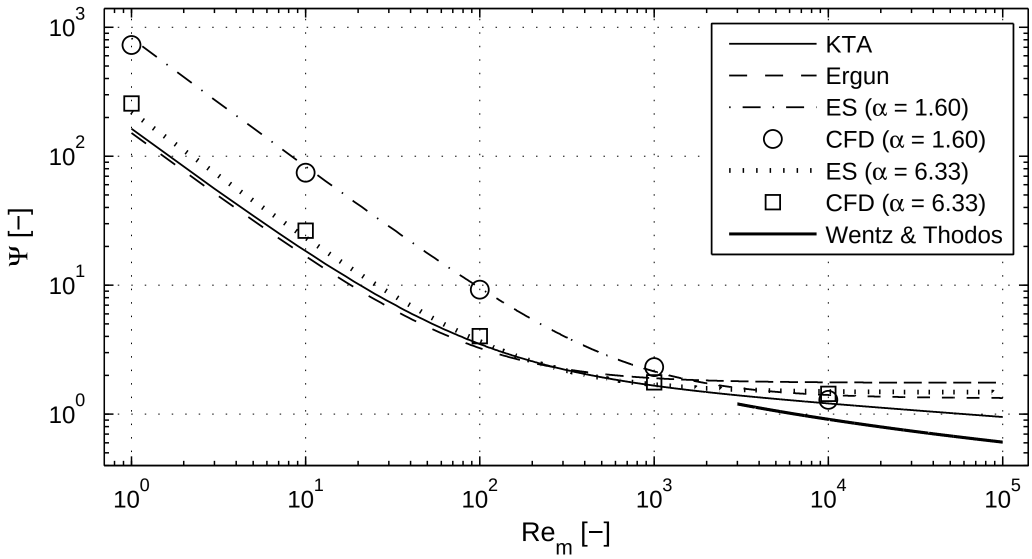

Figure 5.14: Friction factors from different investigations as a functions of Re_m.

Fig. 5.14 shows the values of the friction factors from the correlations of relevance to this investigation, as well as some of the results from the CFD simulations. Values for Ψ_{ES} and Ψ_{CFD} are shown for aspect ratios of $\alpha = 1.60$ and 6.33. Again, it can be seen that the friction factor deviates from Ψ_{KTA} and Ψ_{Ergun} at low aspect ratios. Note that neither Ψ_{KTA} nor Ψ_{Ergun} are functions of α, and does not take the wall effect into account. Thus, the deviation of Ψ_{KTA} and Ψ_{Ergun} from Ψ_{ES} and Ψ_{CFD} is indicative of the contribution of the frictional forces on the wall. It can be seen that there is good agreement between Ψ_{KTA} and Ψ_{Ergun} at low Reynolds numbers, with the difference less than 10%. This also indicates that in creeping regimes the frictional forces has a larger effect on the flow than the packing structure. On the other hand, at large modified Reynolds numbers there is a larger discrepancy between Ψ_{KTA} and Ψ_{Ergun}, with the difference reaching 45%. The KTA correlation was developed using beds with mono-sized spherical particles, whereas the Ergun correlation was developed from packings consisting of non-uniform particles. Thus, it can be concluded that the inertial forces as affected by the packing structure have a larger influence on the flow in turbulent regimes. Since the correlation by Wentz and Thodos, eq. (2.18), was derived from structured packings consisting of mono-sized spherical particles, the deviation of Ψ_{Wentz} from Ψ_{KTA} and Ψ_{Ergun} also reinforces this conclusion. In future investigations, the effect of the inertial forces on the friction factor as a function of the packing structure needs to be investigated in more detail.

5.6 Summary

This chapter contained the results from the CFD simulations of the flow through DEM generated packed beds. All DEM and CFD simulations were run with the methods developed in Chapter 4. It was shown that the randomly packed beds generated using DEM was of high quality, and the structures of these beds were analysed. Detail was given on the computational resources available for this investigation, as well as its limitations on the CFD simulations. The methodology developed in Chapter 4 was validated with measurements from the experimental investigations by Wentz and Thodos (1963) and Hassan and Kang (2012). Good agreement was found between the CFD predictions for pressure drop, and the experimental measurements.

The results for Ψ from the CFD simulations were compared to the predictions of Ψ from the KTA and ES correlations. It was found that at small aspect ratios, the KTA correlation under predicts the friction factor. The results also gave evidence of the fact that the wall effect is Reynolds number dependent, where the pressure drop may increase in creeping flow regimes due to the additional wall friction, and decrease in turbulent regimes due to the increased porosity and permeability. Since Ψ_{ES} compared well with Ψ_{CFD} in all instances, an assumption was made that the ES correlation is valid within its limits. Ψ_{KTA} was then analysed over a wide range of Reynolds numbers and aspect ratios at the hand of Ψ_{ES}. The KTA limiting line for the KTA correlation was found to be valid, but not exact, and a new limiting line was suggested.

The results presented in this chapter fulfilled the goal of the investigation, which was to determine the validity of the KTA limiting line. The next chapter concludes the investigation with conclusions made from the results of the explicit CFD simulations, and recommendations for future work on the topic.

Chapter 6

Conclusions

The goal of this investigation was to determine the validity of the KTA limiting line shown in Fig. 1.1, which is the proposed lower limit of the KTA correlation. This was to be done using an explicit approach, by simulating the flow through DEM generated packed beds. This chapter presents the conclusions made from the results of the explicit CFD simulation, as well as recommendations for future work on the topic.

6.1 Conclusions

This investigation used the commercial CFD package STAR-CCM+® to explicitly analyse the flow through DEM generated packed beds, with small aspect ratios. STAR-CCM+® was used for both the generation of randomly packed beds using DEM, and the simulation of the flow through the beds using CFD.

Steps were taken to ensure accurate solutions with a reasonable degree of confidence. The methods developed by Theron (2011) for creating DEM generated packed beds were improved upon, and beds with aspect ratios of $1.6 \leq \alpha \leq 25$ were generated. The quality of these beds were analysed by calculating the particle overlaps, the bulk porosities and the porosity variations in the axial direction. The particle overlaps were found to be small, with $d_{o,max} < 0.08\%$ for all beds. The bulk porosities were calculated with an analytical method as well as a numerical method. The differences in bulk porosity between the two methods were small, with $\Delta\varepsilon_b < 0.1\%$ for all beds. These calculated values for the bulk porosities also corresponded well with the values predicted by correlations from literature, as well as experimental measurements. Thus, the DEM generated beds were of high quality, though it was found that the lengths of the beds, with $L/d \simeq 10$, were insufficient to fully eliminate the length effect.

Methods were also developed with regards to the CFD simulation of the flow through the DEM generated beds, to ensure simulations which presented realistic results. Particular attention was given to the mesh generation, turbulence modelling and boundary conditions. It was decided to use a polyhedral mesh with two prism layers. Particles were connected with a specific contact area to increase the mesh quality. The Realisable $k-\epsilon$ turbulence model was used, and velocity profiles for fully developed laminar and turbulent flows were specified at the inlet boundary. The methods developed were validated with experimental measurements from literature, for both structured and randomly packed beds. Good agreement was found between the predicted pressure drops from the CFD simulations and the pressure drop measurements of five different experiments. It could be concluded then that the CFD simulations, set up with the methods developed during this investigation, presented realistic results.

With the available resources and the high computational demand of these simulations, the flow through beds with aspect ratios of $\alpha = 1.60$, 2.01, 2.50, 3.00, 3.65, 4.00, 5.00 and 6.33 were simulated. The values for the friction factors from the CFD simulations were calculated from the predicted pressure drops, and compared with the values predicted by the ES and KTA correlations. It was found that Ψ_{CFD} corresponded well with Ψ_{ES} for all instances, as it fell within the 18% NRMSD of the ES correlation. However, Ψ_{KTA} did not correspond well with either Ψ_{CFD} or Ψ_{ES}, particularly at low aspect ratios and low modified Reynolds numbers. This indicated the influence of the wall effect, since the ES correlation takes the wall effect into account, whereas the KTA correlation does not. The Reynolds number dependence of the wall effect could also be seen, where in creeping flow regimes the bed friction has an overwhelming effect on the pressure drop, whereas in turbulent regimes the structure and permeability of the bed has the overwhelming influence. It was also observed that the influence of the wall effect on the flow decreased as the aspect ratio increased.

Since a good correlation was found between Ψ_{CFD} and Ψ_{ES}, and assuming that the ES correlation is valid within its limits, the percentage difference between Ψ_{ES} and Ψ_{KTA} was calculated for a wide range of α and Re_m. It was found that the KTA limiting line is valid, but not exact. A new limiting line for the KTA correlation was suggested, however this new limiting line improved little on the existing line and was still the result of some major assumptions. In order to improve the determination of the position of the KTA limiting line further, criteria need to be established which determine how small the error in predicted friction factor must be before the KTA correlation can be accepted as accurate. Further investigation is required to develop this criteria, as it must take into account the random nature of packed beds and the errors of the ES and KTA correlations.

6.2 Recommendations

This investigation showed that simulating the flow through DEM generated packed beds explicitly do present realistic results. However, these simulations are computationally intensive, and with more resources many improvements could be made to the investigation. The following points are recommendations which could be used in future investigations which analyse the flow through packed beds using an explicit approach:

1. As mentioned above, this investigation showed that the KTA limiting line is valid, but not exact. In order to improve the determination of the position of the KTA limiting line, criteria need to be established which determine how small the error in predicted friction factor must be before the KTA correlation can be accepted as accurate.

2. Future studies may include explicitly simulating the flow through packed beds at higher aspect ratios, if the appropriate resources are available.

3. With the analysis of the DEM generated beds used in this investigation, it was found that

$L/d \simeq 10$ was insufficient to fully eliminate the length effect. Further analysis is required to determine the limit where the length effect can be considered negligible.

4. From the analysis of the DEM generated beds, it was found that the packing structure depends heavily on the aspect ratio. Future work may include in depth analysis of the packing structure as a function of the aspect ratio. With the particular goals of determining the limits between structured and random packings, and quantifying phenomena such as the unusually long length effect observed in the bed with $\alpha = 3.00$.

5. The methods developed in this investigation for the simulation of the flow through packed beds were validated with experimental measurements from literature. Future work could include building an in-house experimental setup with the specific goal of validating the CFD simulation results over a wide range of modified Reynolds numbers and aspect ratios.

6. This investigation focussed only on the pressure drop over packed beds, thus the control volumes were considered adiabatic and no heat transfer was modelled. Future studies may include modelling the heat transfer between the fluid and the particles. Particularly with a heat source within the particles, as is the case in nuclear packed bed reactors.

7. The particles were connected with a specific contact area to increase the mesh quality. The size of the contact area was of little importance in the current investigation, as long as it did not influence the pressure drop over the bed. If in future work the heat transfer between particles were to be modelled, particular focus would need to be given to the size of the contact area and the effective conduction heat transfer coefficient between particles.

8. Localised recovery of total pressure was observed in the flow between particles, at the expense of depletion of total pressure elsewhere in the domain. The potential influence that local total pressure rises may have on the heat transfer within packed beds should also be investigated.

9. It was found that the packing structure has a large influence on the flow through packed beds. In future investigations the effect of the inertial forces on the friction factor as a function of the packing structure needs to be investigated in more detail.

Bibliography

Bai, H., Theuerkauf, J., Gillis, P.A., and Witt, P.M. (2009). A coupled DEM and CFD simulation of flow field and pressure drop in fixed bed reactor with randomly packed catalyst particles. *Industrial and Engineering Chemistry Research*, 48(8):4060–4074.

Benenati, R.F. and Brosilow, C.B. (1962). Void fraction distribution in beds of spheres. *AIChE Journal*, 8(3):359–361.

Benyahia, F. and O'Neill, K.E. (2005). Enhanced voidage correlations for packed beds of various particle shapes and sizes. *Particulate Science and Technology*, 23(2):169–177.

Blake, F.C. (1922). The resistance of packing to fluid flow. *Transactions of the Institution of Chemical Engineers*, 14:415–421.

Calis, H.P.A., Nijenhuis, J., Paikert, B.C., Dautzenberg, F.M., and Van den Bleek, C.M. (2001). CFD modelling and experimental validation of pressure drop and flow profile in a novel structured catalytic reactor packing. *Chemical Engineering Science*, 56(4):1713–1720.

Carman, P. (1937). Fluid flow through granular beds. *Transactions of the Institution of Chemical Engineers*, 15:150–166.

CD-Adapco (2012). *STAR-CCM+ User guide*. 7th edition.

Cheng, G. and Yu, A. (2013). Particle scale evaluation of the effective thermal conductivity from the structure of a packed bed: Radiation heat transfer. *Industrial and Engineering Chemistry Research*, 52(34):12202–12211.

Cheng, G., Yu, A., and Zulli, P. (1999). Evaluation of effective thermal conductivity from the structure of a packed bed. *Chemical Engineering Science*, 54(19):4199 – 4209.

Cheng, N. (2011). Wall effect on pressure drop in packed beds. *Powder Technology*, 210(3):261–266.

Cohen, Y. and Metzner, A.B. (1981). Wall effects in laminar flow of fluids through packed beds. *AICHE J.*, 27(4):705–715.

Cundall, P.A. and Strack, O.D.L. (1979). Discrete numerical model for granular assemblies. *Geotechnique*, 29(1):47–65.

De Klerk, A. (2003). Voidage variation in packed beds at small column to particle diameter ratio. *AIChE Journal*, 49(8):2022–2029.

Di Felice, R. and Gibilaro, L.G. (2004). Wall effects for the pressure drop in fixed beds. *Chemical Engineering Science*, 59(14):3037–3040.

Dixon, A.G. (1988). Correlations for wall and particle shape effects on fixed bed bulk voidage. *Canadian Journal of Chemical Engineering*, 66(5):705–708.

Dixon, A.G., Nijemeisland, M., and Stitt, E.H. (2013). Systematic mesh development for 3D CFD simulation of fixed beds: Contact points study. *Computers & Chemical Engineering*, 48:135–153.

Dolejs, V. and Machac, I. (1995). Pressure drop during the flow of a newtonian fluid through a fixed bed of particles. *Chemical Engineering & Processing: Process Intensification*, 34(1):1–8.

Du Toit, C.G. (2008). Radial variation in porosity in annular packed beds. *Nuclear Engineering and Design*, 238(11):3073–3079.

Du Toit, C.G. and Rosslee, P.J. (2012). Analysis of the porous structure of packed beds of spheres using x-ray computed tomography. In *Eighth South African conference on computational and applied mechanics, SACAM.*

Du Toit, C.G., Van Antwerpen, W., and Rousseau, P.G. (2009). Analysis of the porous structure of an annular pebble bed reactor. In *ICAPP*, 9123.

Eisfeld, B. and Schnitzlein, K. (2001). The influence of confining walls on the pressure drop in packed beds. *Chemical Engineering Science*, 56(14):4321–4329.

Eppinger, T., Seidler, K., and Kraume, M. (2011). DEM-CFD simulations of fixed bed reactors with small tube to particle diameter ratios. *Chemical Engineering Journal*, 166(1):324–331.

Ergun, S. (1952). Fluid flow through packed columns. *Chemical Engineering Progress*, 48(2):89–94.

Goodling, J.S., Vachon, R.I., Stelpflug, W.S., Ying, S.J., and Khader, M.S. (1983). Radial porosity distribution in cylindrical beds packed with spheres. *Powder Technology*, 35(1):23–29.

Graton, L.C. and Fraser, H.J. (1935). Systematic packing of spheres: With particular relation to porosity and permeability. *The Journal of Geology*, 43(8):785–909.

Hassan, Y.A. (2008). Large eddy simulation in pebble bed gas cooled core reactors. *Nuclear Engineering and Design*, 238(3):530–537.

Hassan, Y.A. and Kang, C. (2012). Pressure drop in a pebble bed reactor under high Reynolds number. *Nuclear Technology*, 180(2):159–173.

Issa, R.I. (1995). Rise of total pressure in frictional flow. *AIAA journal*, 33(4):772–774.

KTA (1981). Reactor core design of high-temperature gas-cooled reactors. Part 3: Loss of pressure through friction in pebble bed cores. *Nuclear Safety Standards Commission, "Kerntechnischer Ausschuss"*, 3102.3:1–4.

KTA (1988). Safety Standard by the Nuclear Safety Standards Commission, "Kerntechnischer Ausschuss". *"Bundesanzeiger"*, 44:D1–D36.

Lee, J.J., Park, G.C., Kim, K.Y., and Lee, W.J. (2007). Numerical treatment of pebble contact in the flow and heat transfer analysis of a pebble bed reactor core. *Nuclear Engineering and Design*, 237(22):2183–2196.

Leva, M. and Grummer, M. (1947). Pressure drop through packed tubes, Part III Prediction of voids in packed tubes. *Chemical Engineering Progress*, 43(12):713–718.

Mariani, N.J., Salvat, W.I., Campesi, A., Barreto, G.F., and Martinez, O.M. (2009). Evaluation of structural properties of cylindrical packed beds using numerical simulations and tomographic experiments. *International Journal of Chemical Reactor Engineering*, 7:1.

Mehta, D. and Hawley, M.C. (1969). Wall effect in packed columns. *Industrial and Engineering Chemistry Design and Development*, 8(2):280–282.

Mueller, G.E. (1992). Radial void fraction distributions in randomly packed fixed beds of uniformly sized spheres in cylindrical containers. *Powder Technology*, 72(3):269–275.

Mueller, G.E. (1997). Angular porosity distributions in fixed packed beds of low diameter aspect ratio. *Canadian Journal of Chemical Engineering*, 75(4):677–683.

Mueller, G.E. (2010). Radial porosity in packed beds of spheres. *Powder Technology*, 203(3):626–633.

Mueller, G.E. (2012). A simple method for determining sphere packed bed radial porosity. *Powder Technology*, 229:90–96.

Munson, B.R., Young, D.F., Okiishi, T.H., and Huebsch, W.W. (2010). *Fundamentals of fluid mechanics*. John Wiley and Sons, Inc., 6th edition.

Preller, A.C.N. (2011). *Numerical modelling of flow through packed beds of uniform spheres*. Master of engineering in nuclear engineering, North-West University.

Reddy, R.K. and Joshi, J.B. (2008). CFD modeling of pressure drop and drag coefficient in fixed and expanded beds. *Chemical Engineering Research and Design*, 86(5):444–453.

Reddy, R.K. and Joshi, J.B. (2010). CFD modeling of pressure drop and drag coefficient in fixed beds: Wall effects. *Particuology*, 8(1):37–43.

Reichelt, W. (1972). Calculation of pressure drop in spherical and cylindrical packings for single-phase flow (Zur Berechnung des Druckverlustes einphasig durchstroemter Kugel- und Zylinderschuettungen). *Chemie-Ingenieur-Technik*, 44(18):1068–1071.

Reyneke, H.J. (2009). *Investigation into the velocity distribution through an annular packed bed*. Master of engineering in nuclear engineering, North-West University.

Reynolds, O. (1900). Papers on mechanical and physical subjects. *Cambridge University Press*, 14:81–85.

Ridgway, K. and Tarbuck, K.J. (1966). Radial voidage variation in randomly-packed beds of spheres of different sizes. *Journal of Pharmacy and Pharmacology*, 18(S1):168S–175S.

Roblee, L.H.S., Baird, R.M., and Tierney, J.W. (1958). Radial porosity variations in packed beds. *AIChE Journal*, 4(4):460–464.

Rosslee, P.J. (2009). Analysis of the variation in the porosity of packed columns. Technical report, North-West University, Potchefstroom, South-Africa.

Sederman, A.J., Alexander, P., and Gladden, L.F. (2001). Structure of packed beds probed by magnetic resonance imaging. *Powder Technology*, 117(3):255–269.

Tabor, G.R. and Baba-Ahmadi, M.H. (2010). Inlet conditions for large eddy simulation: A review. *Computers and Fluids*, 39(4):553–567.

Theron, W.G.J. (2011). *Numerical analysis of the flow distribution within packed columns using an explicit approach*. Master of engineering in nuclear engineering, North-West University.

Van Antwerpen, W., Du Toit, C.G., and Rousseau, P.G. (2010). A review of correlations to model the packing structure and effective thermal conductivity in packed beds of mono-sized spherical particles. *Nuclear Engineering and Design*, 240(7):1803–1818.

Versteeg, H.K. and Malalasekera, W. (2007). *An introduction to Computational Fluid Dynamics: The finite volume method*. Pearson Education Limited, 2nd edition.

Voronoi, M.G. (1908). Nouvelles applications des parametres continus a la theorie des formes quadratiques. Deuxieme memoire. Recherches sur les parallelloedres primitifs. *Journal fur die reine und angewandte Mathematik*, 134:198–287.

Wensrich, C. (2012). Boundary structure in dense random packing of monosize spherical particles. *Powder Technology*, 219:118–127.

Wentz, C.A. and Thodos, G. (1963). Pressure drops in the flow of gases through packed and distended beds of spherical particles. *AIChE Journal*, 9(1):81–84.

White, S.M. and Tien, C.L. (1987). Analysis of flow channeling near the wall in packed beds. *Warme - und Stoffubertragung*, 21:291–296.

Winterberg, M. and Tsotsas, E. (2000). Impact of tube-to-particle-diameter ratio on pressure drop in packed beds. *AIChE Journal*, 46:1084–1088.

Zhu, H.P., Zhou, Z.Y., Yang, R.Y., and Yu, A.B. (2007). Discrete particle simulation of particulate systems: Theoretical developments. *Chemical Engineering Science*, 62(13):3378–3396.

Zou, R.P. and Yu, A.B. (1995). The packing of spheres in a cylindrical container: the thickness effect. *Chemical Engineering Science*, 50(9):1504–1507.

LaTeX